NORTHWESTERN UNIVERSITY

Electrostatically Driven Assembly of Charged Amphiphiles Forming Crystallized Membranes, Vesicles and Nanofiber Arrays

A DISSERTATION

SUBMITTED TO THE GRADUATE SCHOOL

IN PARTIAL FULLFILLMENT OF THE REQUIREMENTS

For the degree

DOCTOR OF PHILOSOPHY

Field of Physics and Astronomy

By

Cheuk Yui (Curtis) Leung

EVANSTON, ILLINOIS

December 2013

ProQuest LLC.
789 East Eisenhower Parkway
P.O. Box 1346
Ann Arbor, MI 48106 - 1346

ABSTRACT

Electrostatically Driven Assembly of Charged Amphiphiles Forming Crystallized Membranes, Vesicles and Nanofiber Arrays

Cheuk Yui (Curtis) Leung

Charged amphiphilic molecules can self-assemble into a large variety of objects including membranes, vesicles and fibers. These micro to nano-scale structures have been drawing increasing attention due to their broad applications, especially in biotechnology and biomedicine. In this dissertation, three self-assembled systems were investigated: +3/-1 self-assembled catanionic membranes, +2/-1 self-assembled catanionic membranes and +1 self-assembled nanofibers. Transmission electron microscopy (TEM) combined with synchrotron small and wide angle x-ray scattering (SAXS and WAXS) were used to characterize the coassembled structures from the mesoscopic to nanometer scale.

We designed a system of +3 and -1 ionic amphiphiles that coassemble into crystalline ionic bilayer vesicles with large variety of geometries that resemble polyhedral cellular crystalline shells and archaea wall envelopes. The degree of ionization of the amphiphiles and their intermolecular electrostatic interactions can be controlled by varying pH. The molecular packing of these membranes showed a hexagonal to rectangular-C to hexagonal phase transition with increasing pH, resulting in significant changes to the membrane morphology. A similar mixture of +2 and -1 ionic amphiphiles was also investigated. In addition to varying pH, which controls the headgroup attractions, we also adjust the tail length of the amphiphiles to control the van der Waals interactions between the tails. A 2D phase diagram was developed to show how pH and

tail length can be used to control the intermolecular packing within the membranes.

Another system of self-assembled nanofiber network formed by positively charged amphiphiles was also studied. These highly charged fibers repel each other and are packed in hexagonal lattice with lattice constant at least eight times of the fiber diameter. The d-spacing and the crystal structure can be controlled by varying the solution concentration and temperature.

Approved

Professor Michael J. Bedzyk

Department of Materials Science and Engineering and

Department of Physics and Astronomy

Northwestern University

Evanston, Illinois

Acknowledgements

I would like to thank my advisor Professor Michael Bedzyk for his support and guidance during my graduate studies in Northwestern. He is very encouraging and he gave me a lot of advices for my personal development. He taught me to be a critical thinker and gave me great freedom in my research.

I thank Professors Monica Olvera de la Cruz, Pulak Dutta and John Marko for serving on my doctoral committee. I especially like to show my appreciation to Professor Monica Olvera de la Cruz for helping me in writing scientific papers and inspiring me in my researches.

I also thank my collaborators at Northwestern University. Dr. Liam Palmer has been producing quality samples for our measurements and taught me a lot of chemical techniques. I thank Dr. Sumit Kewalramani for helping me in the experiments as well as his willingness to discuss many aspects of scientific research. I really enjoyed the many nights that I spent with Liam and Sumit at Argonne National Laboratory talking about research and life. I thank Dr. Baofu Qiao for conducting atomistic simulation and his work increased our understanding of the systems from the theoretical point of view. I also thank Drs. Rastko Sknepnek, Graziano Vernizzi, Christina Newcomb and Megan Greenfield for their generous help and discussion in the research projects. I especially thank Drs. Steve Weigand and Denis Keane at the DND-CAT and Byeongdu Lee and Soenke Seifert at sector 12-ID for their helps in setting up the small angle x-ray scattering experiments.

I am also grateful to work with many present and past Bedzyk group members including Dr. Jeff Klug, Dr. Phillip Lin, Dr. Zhenxing Feng, Dr. Jon Emery, Martin McBriarty, I-Cheng Tung, Bor-Rong Chen, Xiao Chen, Li Zeng, Liane Moreau, Gavin Campbell, Dr. Sudeshana

Chattopadhyay and Dr Sven Stoltz. I especially give thanks to Dr. Zhenxing Feng, Dr. Jon Emery and Bor-Rong Chen for their friendships and discussions about life. I also treasure the times that I spent with my many friends at Northwestern.

Finally, I want to thank my parents and my sister for their love and support all these years. They have always listened to me when I share with them about work or life and encouraged me to follow my dreams.

Above all I honor my wife and my best friend Bella for her love, sacrifices and support in my graduate study. I could not have achieved these goals without her. I also thank God for bringing me to Northwestern University and having the chance to work with all these great people.

For Bella

TABLE OF CONTENTS

LIST OF FIGURES

LIST OF TABLES

Chapter 1. Introduction

Self-assembled systems of amphiphilic molecules have attracted increasing interest due to their applications in biotechnology and medicines. Self-assembly is defined as the process in which a disorganized system of pre-existing molecules assembles into an organized structure just by the interactions among the components themselves and without external direction. A large variety of structures such as micelles, membranes, vesicles and fibers can be formed depending on the structure, properties and the local environment of the amphiphiles.(1-4) Specifically, the geometry of the self-assembled structure is determined by the critical packing parameter v/a_0l_c, where v is the volume occupied by the amphiphile, a_0 is the optimal area of the headgroup and l_c is the critical chain length which defines the maximum limit on how far the tail can extends.(5) The relationship between the critical packing parameter and the object structure is shown in Table 1.1. When this parameter is small (< 1/3), each molecule is characterized by cone shape which forms spherical micelles.(Fig. 1.2a) An increase in v/a_0l_c indicates the molecular shape becomes more cylindrical, which leads to other structures such as cylindrical micelles (fiber) and bilayers.(Fig. 1.2b-d) When this parameter is very large, we will observe inverted micelles. (Fig. 1.2e)

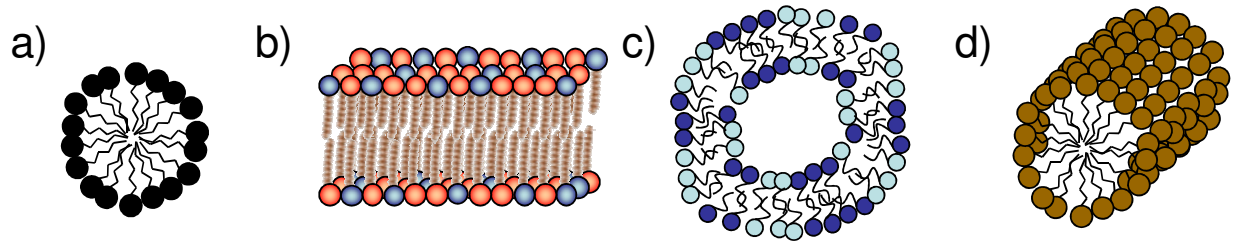

Figure 1.1. Schematic of (a) micelle; (b) membrane; (c) vesicle and (d) fiber

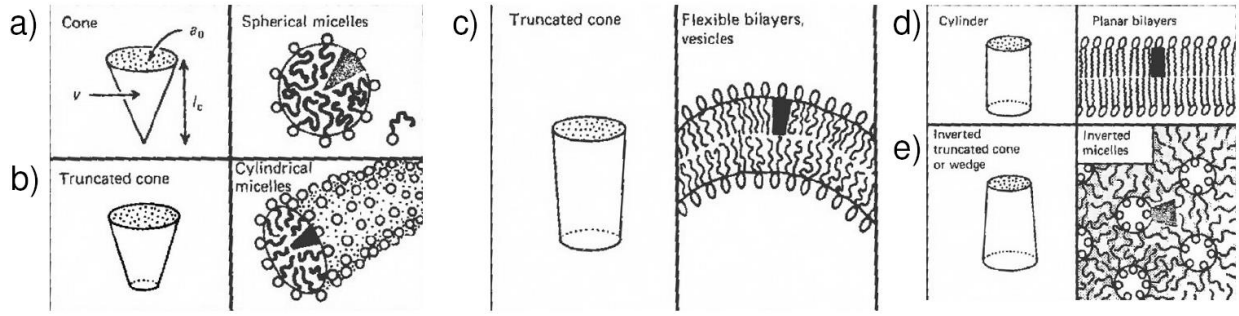

Figure 1.2. Mean packing shapes of lipids and the corresponding structures. (a) Spherical micelles, (b) cylindrical micelles, (c) flexible bilayers, (d) planar bilayers and (e) inverted micelles. (Image from Israelachvili)(5)

Table 1.1. Critical packing parameter and the corresponding assembled structure.(5)

Critical packing parameter (v/a_0l_c)	Assembled structure
<1/3	Spherical micelles
1/3-1/2	Cylindrical micelles
1/2-1	Flexible bilayer
~1	Planar bilayers
>1	Inverted Micelles

The shape and the structures of these assemblies can be used to carry out different functions. For example, systems of bilayer vesicles have been designed for various applications including drug delivery,(6) gene therapy,(7-9) as templates for synthesis,(10, 11) biomineralization(12) and as cell models.(13) Traditionally, phospholipids have been most commonly used to make vesicles. These kinds of vesicles are generally metastable(14) and the assembly process includes steps such as sonication,(15) thin-film hydration(16) or extrusion.(17) Later, it has been discovered

that by mixing cationic and anionic amphiphiles, they coassemble spontaneously into catanionic vesicles.(18-20) These vesicles tend to be stable for very long periods of time although their actual equilibrium structures are still under debate. Vesicles are also easy to make and there is a large variety of amphiphilic headgroups and tails to choose from that determines the function of the assembled structures.

While most of the vesicles developed to date adopt highly symmetric spherical shapes, Dubois *et al* showed that it is possible to make icosahedral vesicles where the faceting of the membrane walls occurs due to the crystallization of the oppositely charged amphiphiles.(21, 22) These icosahedra resemble the shape of some viruses observed in nature and may explain the origin of these shapes. In addition to icosahedra shapes, there are also microorganisms that exhibit even less symmetric shapes such as archaea(23) and some cellular carboxysomes.(24) In this thesis, we seek to understand how to design facetted vesicles that reproduce these polyhedral shapes. By mixing cationic and anionic amphiphiles together, the electrostatic attractions between them induce crystallization of the amphiphilic tails and form crystallized membrane. The heterogeneous coassembly within the bilayer breaks the symmetry and allows the formation of these nonspherical shapes. In addition, through control of the electrostatic interactions between the amphiphilic headgroups and the van der Waals interactions between the tails, we explore the possibility to control the membrane crystalline structure as well as the overall membrane morphology. pH determines the ionization state of the cationic and the anionic headgroups and therefore the electrostatic interactions between them.(Fig. 1.3a) The alkyl tail length controls the strength of the van der Waals interaction of the chains. (Fig. 1.3b) These studies can give new insights into the control of membrane structures at specific pH, temperature and salt conditions, which may lead to possible applications in targeted drug delivery and gene therapy.

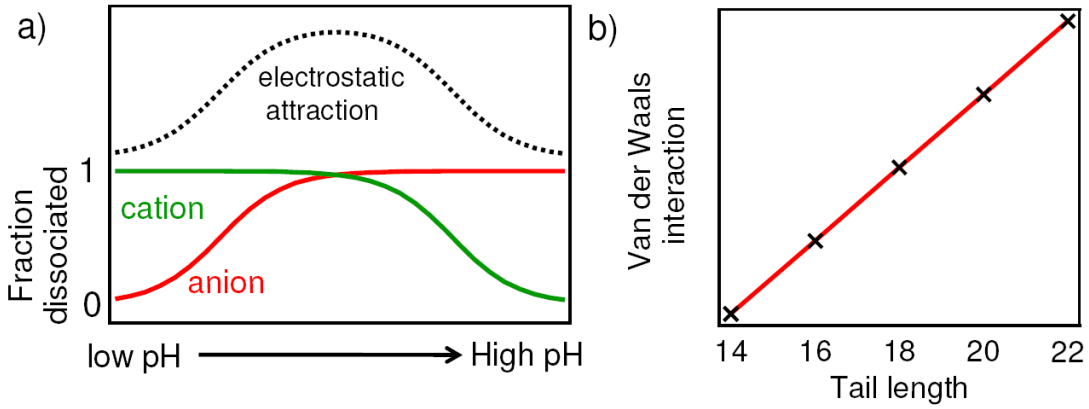

Figure 1.3 (a) Electrostatic interaction between the cationic and anionic headgroups within a crystallized membrane controlled by pH. (b) Van der Waals interaction between the amphiphilic tails increases with tail length.

Besides 2D bilayer systems, 1D self-assembled nanofibers have also attracted attention for their applications in many areas such as their ability to mimic the extracellular matrix and promote tissue regeneration.(25, 26) It may be possible to use aligned 1D nanostructures as templates for inorganic semiconductor materials as pathways to move charge carriers in transistors or photovoltaic devices.(27-29) In this thesis, we also describe a system of highly charged self-assembled nanofibers that form an ordered network in dilute aqueous solution. The ordering of these fibers can be controlled by temperature and the solution concentration. We expect such a network could allow the templated growth of hybrid organic-inorganic materials on the appropriate length scale for energy applications.

Chapter 2. Overview

Coassembled molecular structures are known to exhibit a large variety of geometries and morphologies including micelles, bilayers and fibers. The shape, molecular composition and the structure determine the function of such an assembly. Therefore, a grand challenge of self-assembly design is to find techniques to control the crystal symmetries and overall morphologies of multicomponent systems. The primary characterization methods used in this dissertation are discussed in Chapter 3. In Chapter 4, we show that by mixing +3 and -1 ionic amphiphiles, crystalline ionic bilayers can be assembled in a large variety of geometries that resemble polyhedral cellular crystalline shells and archaea wall envelopes. We combine transmission electron microscopy (TEM) with small- and wide-angle X-ray scattering (SAXS/WAXS) to characterize the coassembled structures from the mesoscopic to nanometer scale. The degree of ionization of the amphiphile headgroups and their intermolecular electrostatic interactions can be controlled by varying pH. With pH adjustment, we are able to change the crystalline structure of molecules packed within the bilayer membrane. We also find that the overall morphology of the membranes has a close relationship with the bilayer crystalline structure. Accurate atomistic molecular dynamics simulations reveal bilayers of hexagonally packed tails at low pH, where only a small fraction of anionic headgroups is charged. Coarse-grained simulations suggest that the faceted vesicles observed in low pH consist of flat crystalline domains separated by liquid-like edges.

A similar system of +2 and -1 ionic amphiphilic mixture is discussed in Chapter 5. In addition to varying pH, which controls the headgroup attractions, we also adjust the tail length of the amphiphiles to control the van der Waals interactions between the tails. The pH and the

hydrophobic tail length modify the intermolecular packing and the symmetry of their crystalline phase. For long or short hydrophobic tail lengths (C_{14} and C_{22}), we observe the coassembly into crystalline bilayers and the crystalline phase is insensitive to pH change. For intermediate tail length (C_{16} to C_{20}), WAXS shows different crystalline molecular ordering depending on pH. As the tail length increases, the hexagonal lattice spacing decreases due to an increase in van der Waals interactions, as demonstrated by atomistic molecular dynamics (MD) simulations. Our work demonstrates that it is possible to control membrane crystal structures by changing the solution pH value within a range of physiological conditions in bilayers of molecules with ionizable groups at room temperature.

In addition to bilayer systems, we also explore the self-assembly of nanofiber networks. Charged nanofibers are well known in natural systems such as filamentous viruses(30) and the cellular cytoskeleton.(31, 32) The unique properties of these structures have inspired the design of self-assembled nanofibers for applications in regenerative medicine and catalysis. The ability to order such one-dimensional objects in solution may have useful applications, such as the templated synthesis of highly ordered organic-inorganic hybrid materials. In Chapter 6, we discuss an azobenzene-based amphiphile that can self-assemble into highly charged nanofibers in water. Small-angle X-ray scattering shows that these nanofibers form crystalline networks with large inter-fiber spacings up to 130 nm mediated by repulsive forces between the charged nanostructures. Addition of salt destroys the crystal pattern, indicating the electrostatic repulsions are necessary for the observed ordering. Solution concentration and temperature can be adjusted to control the packing structure and large inter-fiber spacings.

Chapter 7 provides a summary of this thesis and some possible future works. The first part describes an experiment to test the molecule encapsulation ability of the vesicles. The second

part proposes a phospholipid bilayer system that we may be able to control the vesicle shapes by adjusting the molecular composition within the membrane.

Chapter 3. Characterization Methods

3.1. Transmission Electron Microscopy (TEM)

Cryogenic transmission electron microscopy (cryo-TEM)(33) and quick freeze deep-etch transmission electron microscopy (QFDE-TEM) are techniques for imaging vesicles, fibers or micelles in solution. Cyro-TEM images the frozen sample solution directly and therefore allows us to see the inside of the structures for example multilamellar vesicles.

Cryogenic transmission electron microscopy (cryo-TEM) imaging was performed on a JEOL 1230 microscope, operating at 100 kV. A small droplet of the solution (5–10 μL) was placed on a holey carbon film supported on a TEM copper grid. The grid was held by a tweezer mounted on a Vitrobot VI equipped with a controlled humidity and temperature environment. The specimen was blotted and plunged into a liquid ethane reservoir cooled by liquid nitrogen. The vitrified samples were transferred to a Gatan 626 cryo-holder through a cryo-transfer stage cooled by liquid nitrogen. During observation of the vitrified samples, the cryo-holder temperature was maintained below –180 °C. The images were recorded with a CCD camera.

Quick Freeze Deep-Etch QFDE-TEM is a technique for direct imaging of vesicles or micelles in solution. A preparation method similar to the one used by Pederson *et al*(34) was used. Each specimen is slammed down onto a –170 °C copper plate (Gentleman Jim Slam Freezing Apparatus). The frozen sample is then transferred into a freeze-fracture apparatus (model CFE-40; Cressington Scientific Instruments, Watford, UK) and fractured, etched for 20 minutes at –95 °C, followed by application of platinum coating at a 20° angle and carbon coating at 90° angle at –125 °C. The replicas are then washed with water and transferred onto copper mesh

TEM grids. TEM was done on a JEOL 1230 transmission electron microscope, which is available in the Northwestern University Biological Imaging Center.

3.2. Small/ Wide Angle X-ray Scattering (SAXS/WAXS)

The technique of SAXS is used to study structural features with length scales ranging from 1 nm to 1000 nm.(35-37) It is useful in determining the size and shape of macromolecules and packing structures of objects larger than 1 nm. The scattering intensity $I(q)$ is given by

$$I(q) = |A(q)|^2 S(q), \tag{3.1}$$

where $A(q)$ is the form factor of an isolated object and $S(q)$ is the structure factor corresponding to the correlation between objects, $\boldsymbol{q}$ is the scattering vector , which is the momentum transfer of the incident and scattered wave vectors ($\boldsymbol{q}=\boldsymbol{K}_f - \boldsymbol{K}_i$). The magnitude of $\boldsymbol{q}$ can be defined as

$$q = \frac{4\pi \sin(\theta)}{\lambda}, \tag{3.2}$$

where θ is the one-half of the scattering angle, 2θ and λ is the wavelength of the incident and elastically scattered X-rays.

When there is no correlation between the objects, which means the solution is dilute, $S(q)$ can be estimated to be 1. The scattering intensity $I(q)$ then only depends on the form factor $A(q)$. The amplitude $A(\boldsymbol{q})$ from a single object can be calculated by the Fourier transform of the electron density $\rho(\boldsymbol{r})$.

$$A(\boldsymbol{q}) = \int_v \rho(\boldsymbol{r}) e^{-\boldsymbol{q}\cdot\boldsymbol{r}} d\boldsymbol{r} \tag{3.3}$$

The total intensity is

$$I(\boldsymbol{q}) = |A(\boldsymbol{q})|^2. \tag{3.4}$$

Therefore, by fitting the form factor, we are able to obtain the dimension and the electron density profile of the objects. If equation [3.1] is expanded as a power series, the intensity can be approximated by Guinier's Law

$$I(q) = \rho_0^2 v^2 \exp\left(-\frac{1}{3} q^2 R_g^2\right), \tag{3.5}$$

where ρ_0 and v is the average density and volume of the scatters, R_g is the radius of gyration of the object defined as

$$R_g^2 = \frac{\int \boldsymbol{r}^2 \rho(\boldsymbol{r}) d\boldsymbol{r}}{\int \rho(\boldsymbol{r}) d\boldsymbol{r}}, \tag{3.6}$$

that can determine the approximate size of the scattered objects

The Porod region locates at a higher q than the Guinier region. The Porod region can be approximated by the power law

$$I(q) \propto q^{-\alpha}. \tag{3.7}$$

The exponent α defines the dimensionality of the scatters: 1 for one-dimensional objects, 2 for two-dimensional objects and 4 for three-dimensional objects.

WAXS studies structure of scale smaller than 10 Å and thus is suitable for measuring molecular spacing. Diffraction peaks in the WAXS region can be used to determine the diffraction plane spacing using the relation $d = 2\pi / q$ and thus the lattice structure.

SAXS and WAXS patterns were collected simultaneously by two separate CCD X-ray areal detectors (Figure 3.1) at the DND 5ID-D and 12ID-B undulator beamlines of the Advanced Photon Source at Argonne National Laboratory. The sample solution was injected through a capillary tube flow-cell (Figure 3.2) at room temperature to reduce radiation damage. The

capillary was surrounded by vacuum to avoid air scattering. Data was collected at an incident photon energy of 10.00 keV (wavelength λ = 1.240 Å) with the sample to detector distances arranged to allow the 2θ scattering-angle range of the SAXS detector to partially overlap the 2θ-range covered by the WAXS detector. For purposes of background subtraction, SAXS-WAXS patterns were also collected from the empty capillary and from the capillary containing the solution without the amphiphiles. The exposure time for each image was 10 s and five images were taken for each sample. The 2D SAXS-WAXS patterns were converted into 1D radial intensity patterns, $I(\theta)$, by circular integration.

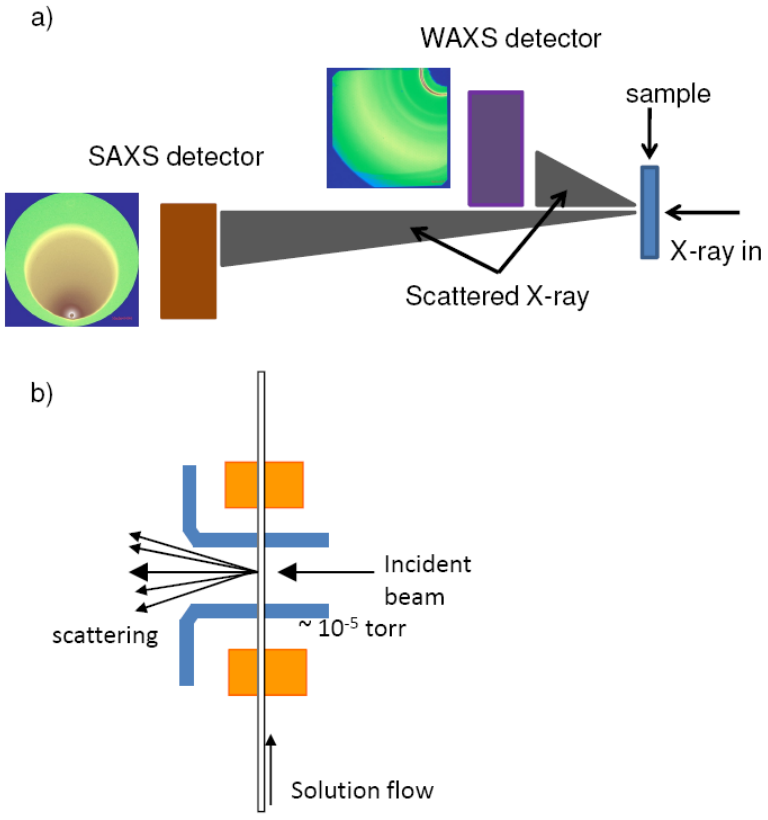

Figure 3.1. (a) Schematic of the SAXS/ WAXS detector system. SAXS and WAXS patterns were collected simultaneously by two separate CCD X-ray areal detectors. (b) Schematic of the solution flowcell setup.

Chapter 4. Molecular Crystallization Controlled by pH Regulates Mesoscopic Membrane Morphology

4.1. Introduction

A large variety of amphiphilic molecules with charged headgroups self-assemble into closed structures akin to cell membranes.(19, 20, 38, 39) Many closed membranes including viral capsids,(40) bacterial microcompartments(24, 41, 42) and halophilic organism envelopes(23, 43) spontaneously adopt complex shapes, including icosahedra and other polyhedral geometries, which suggests that these envelopes are likely to exhibit internal crystalline ordering within their membranes. The ability to fabricate nanocontainers with specific internal structures and geometries(44) is highly desirable for applications including catalysis, gene therapy, and targeted drug delivery.(45-47) Specifically, nano switches that can convert chemical energy into mechanical energy could be used to open and close membranes or to create large structural changes in the membrane thickness. However, it remains unknown how the specific crystal structure within a membrane affects its overall morphology on multiple length scales. Nevertheless, such a mechanism must exist as shown by many natural systems; for instance, the robust envelope of halophilic microorganisms, which allows them to survive in extreme environments, takes a square geometry,(43) even though the cell wall is actually composed of a hexagonal lattice (23) of various lipids.

In this chapter, we explore the possibility of using electrostatic interactions as one parameter to drive structural changes in the coassemblies of ionic amphiphiles into lattices that are expected to form nanocontainers with specific shape and composition.(21, 48-50) Specifically, we show that the pH of the solution can be used to vary the equilibrium shape of ionic crystalline

amphiphilic membranes, via a fascinating multiscale process that correlates global mesoscopic shape to the local nanoscale crystalline structure. Ionic coassemblies generally disassemble at physiological salt concentrations. (51-53) Therefore, we use long alkyl tail amphiphiles for which the additional intertail van der Waals attractions lead to salt-stable, ionically driven coassemblies.

While single-tailed ionic amphiphiles typically form micelles,(54) mixtures of oppositely charged amphiphiles have a distinct behavior resulting in bilayers that can even self-assemble into micrometer-sized icosahedral vesicles under salt-free conditions.(21, 55) Previous work on polymerizable amphiphiles showed that a large charge imbalance between the cationic and anionic headgroups enables their coassembly into nanoscale faceted structures.(49, 56) By coassembling oppositely charged surfactants without a polymerizable group, we demonstrate that electrostatics provides the essential "glue" for the crystallization of the tails and the potential to modify the structure by changing the solution pH. In fact, the solution pH controls electrostatic correlations, which in turn determine the two dimensional crystalline structure. Furthermore, crystalline domains can lead to the formation of closed shell shapes other than the ubiquitous icosahedra. Those shapes, which resemble organelle microcompartments (42) and faceted halophilic organisms,(43) are stable over time even at high salt concentrations. To observe structural changes at the mesoscopic and the atomistic length scales, we use transmission electron microscopy (TEM) for the 10 to 1000 nm length scale (overall membrane morphology), in situ small-angle X-ray scattering (SAXS) for observing the 1100 nm length scale (membrane wall thickness), and in situ wide-angle X-ray scattering (WAXS) to observe the angstrom scale (two-dimensional molecular crystal structure within the membrane).

4.2. Materials and Methods

4.2.1. Material Synthesis and Sample Preparation

All amino acids and Rink MBHA resin were purchased from Novabiochem Corporation (San Diego, CA). All other reagents and solvents for peptide synthesis were purchased from Aldrich or TCI and used as provided. The synthesis of the N-palmitoyl trilysine **C_{16}-K_3** was performed using standard manual solid-phase peptide synthesis methods. Briefly, peptides were grown on Rink amide MBHA polystyrene resin, using 4.0 molar equiv of an Fmoc-protected amino acid, 3.95 equiv of 2-(1H-benzotriazole-1-yl)-1,1,3,3-tetramethyluronium hexafluorophosphate (HBTU), and 6 equiv of N,N-diisopropylethylamine (DIEA) for each residue coupled to the resin. The palmitic acid tail was subsequently coupled to the N-terminus of the peptide by adding 8.0 molar equiv of palmitic acid **C_{15}-COOH** to the peptide in the presence of 7.95 molar equiv of HBTU and 12 molar equiv of DIEA. The palmitic acid was then cleaved from the polystyrene resin, and amino acid side groups were deprotected in 95%trifluoroacetic acid (TFA), 2.5%triisopropylsilane (TIS), and 2.5% deionized water. TFA was removed by rotary evaporation, and the peptide product was collected by precipitation with cold diethyl ether. Peptide **C_{16}-K_3** was purified by Varian preparative HPLC using a Waters Atlantis C-18 30 - 250 mm column under a slow elution gradient of 98% to0%water and acetonitrile (0.1% TFA). Separation with a gradient of 40_60% water over 25 min gave the desired peptide **C_{16}-K_3** as the trifluoroacetate salt. The schematic diagram in Figure 4.1 summarized the synthesis process of **C_{16}-K_3**.

Cation **C_{16}-K_3** was first dissolved in Milli-Q water at a concentration of 4mM(typically 750 μL). This solution was added to a centrifuge tube containing 3 equiv of solid palmitic acid **C_{15}-COOH**. The mixture was agitated and heated to 80^{o}C for 60 min. Each sample was cooled to room temperature then centrifuged at approximately 2000 rpm for 5 min to remove residual

palmitic acid prior to analysis. The pH of this solution was approximately 3 before and after heating. The pH of each sample (except pH 3) was adjusted with 1 M NaOH after heating.

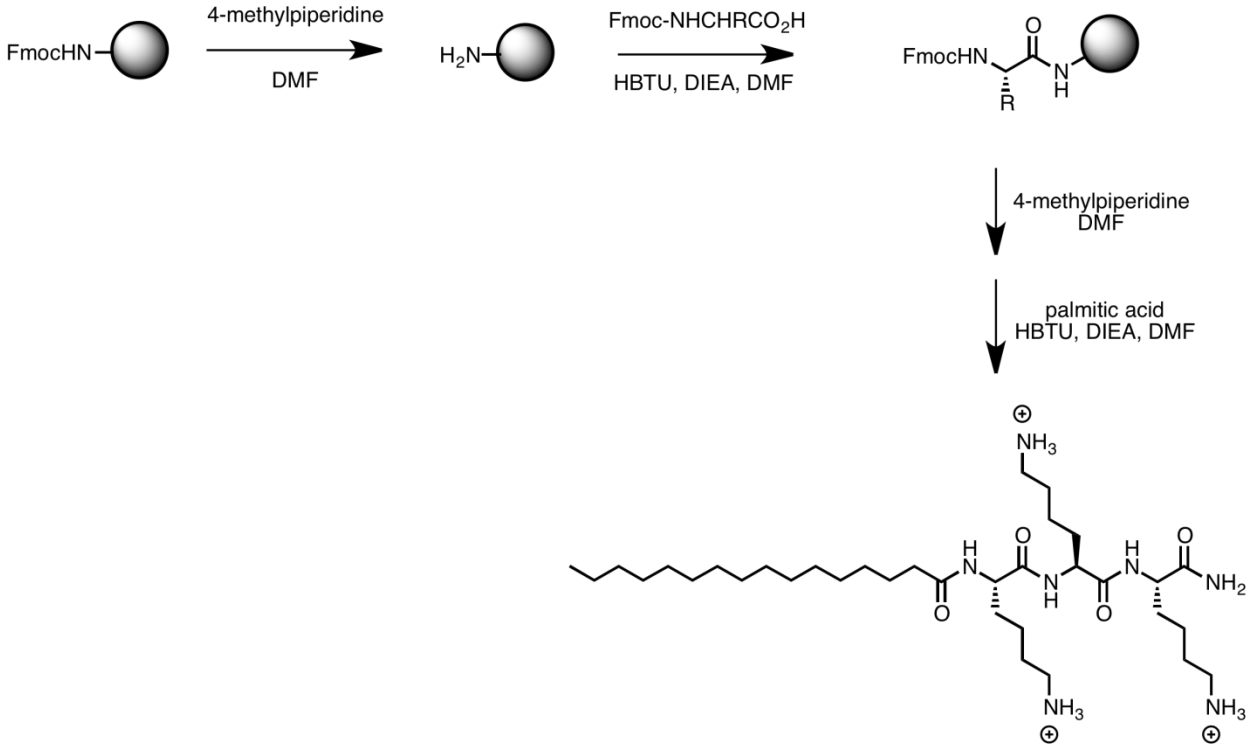

Figure 4.1. The schematic diagram showing the synthesis procedure of molecule $\mathbf{C_{16}\text{-}K_3}$.

4.2.2. Methods

Cryogenic transmission electron microscopy (cryo-TEM) imaging and Quick Freeze Deep-Etch (QFDE) transmission electron microscopy imaging techniques were used. The details are discussed in Chapter 3.2. SAXS and WAXS experimental setup is discussed in Chapter 3.3.

4.2.3. Theory and Simulations

Theoretical calculations and simulations were conducted by Dr. Bao Fu Qiao in Professor

Monica Olvera de la Cruz's group.

The effects of correlations on the dissociation of acid and basic groups as a function of the pH value are obtained by Monte Carlo simulations. We model a two-component system on a triangular lattice with two types of sites, those that are acidic (i.e., can be either neutral $q_A = 0$ or negatively charged $q_A = -1$) and those that are basic (i.e., $q_B = 0$ neutral or positively charged $q_B = +1, +2, +3$). The sites are placed on the lattice chosen to approximate the location of acidic and basic headgroups in the experimental system of interest. Three q_B sites are connected to represent a single molecule. The Hamiltonian used in the simulations is given by

$$\frac{H}{k_B T} = \frac{\mu_A}{k_B T}\sum_i Z_i^A + \frac{\mu_B}{k_B T}\sum_i Z_i^B - \frac{1}{2} l_B \kappa \sum_i Z_i^2 + \frac{1}{2}\sum_{i \neq j} Z_i Z_j l_b (-1)^{\eta} \frac{e^{-\kappa r_{ij}}}{r_{ij}} \qquad (4.1)$$

where Z_i is the absolute value of the ionization state of site I (i.e., $Z^A = 0, 1$ and $Z^B = 0, 1, 2, 3$), and $\eta = 0$ (1) if sites i and j have the same (opposite) sign. The chemical potentials are given as

$$\frac{\mu_I}{k_B T} = -\ln 10\left(pH - pKa_{(I)}\right) \qquad (4.2)$$

for I = A, B.

The atomistic MD simulations were performed using the GROMACS package (version 4.5.5). The latest version of the GROMOS96 54A7 united-atom force field(57) was employed for the amphiphiles; water is modeled using the SPC model. The electrostatic interactions were calculated using the particle mesh Ewald method, and the short-range Lennard-Jones interactions were truncated at 1.2 nm. Two systems representing the ionization degrees of palmitic acid molecules of 30 and 95%, respectively, were investigated, which are correspondingly composed of 660 (30%) and 632 (95%) amphiphiles. The simulations were started from pseudobilayer structures (no interdigitation), as we care about the equilibrium structure, rather than the slow kinetics of the self-assembling process. The simulation was performed for a duration of 300 ns

for the system with 30% ionization of palmitic acid. The formation of the interdigitation in the system with 30% ionization of palmitic acid is very slow, requiring a simulation as long as 1 μs. In the simulations, the area per lipid tail was tracked for the equilibration of the systems.

The MARTINI coarse-grained MD simulation was performed by employing the latest stable MARTINI force field (version 2.1).(58, 59) The planar bilayer was prepared and equilibrated at room temperature. Increasing the temperature to 350 K leads to the spontaneous formation of a spherical vesicle. Returning to ambient temperature and removing ~ 40% of the waters in the vesicle interior sped up the simulation, and faceted vesicles were obtained within 100 ns. The MARTINI MD simulation was performed for the duration of up to 1 μs.

4.3. Experimental Results and Discussion

Figure 4.2a depicts the two oppositely charged amphiphiles used in this study, with dissimilar headgroups but identical hydrophobic tails. Amphiphile **C_{15}-COOH** is a monovalent anionic fatty acid (palmitic acid). Amphiphile **C_{16}-K_3** comprises a trivalent cationic headgroup of three lysine (**K**) amino acids and a hydrophobic palmitoyl tail. (60) The charge ratio of +3/-1 (rather than +1/-1) (21, 22) is expected to reinforce the ionic correlations and maximize the packing of the hydrophobic tails into crystalline lattices. Cryogenic TEM (Figure 4.2 b-d) and quick-freeze/deep-etch TEM (Figure 4.3) are used to image the hydrated structures. As expected for simple surfactants with a large headgroup, cation **C_{16}-K_3** dissolves in water and forms micelles of ~10 nm diameter (Figure 4.3). It can be coassembled with water-insoluble palmitic acid **C_{15}-COOH** at different pH values to control the shape of membranes, as shown in Figure 1b-d. The cation/anion mixture images show a pH-dependent diversity of shapes including closed unilamellar and multilamellar faceted vesicles (Figure 4.2 b,d) and open sheets or ribbons

(Figure 4.2 c,d). All of these structures are consistent with a bilayer membrane morphology as discussed below.

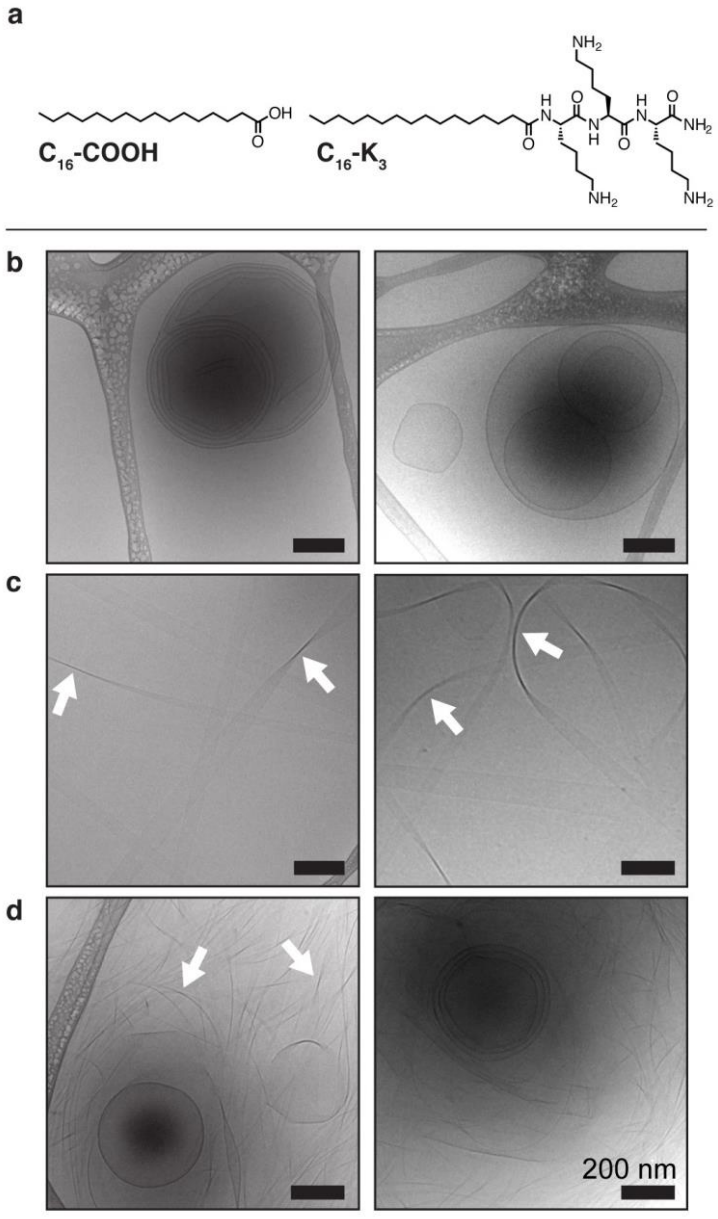

Figure 4.2. Coassembly of oppositely charged amphiphiles shows vesicles in aqueous solution. (a) Charged amphiphiles used for ionic coassembly: -1 palmitic acid (**C_{15}-COOH**) with +3

trilysine (**C_{16}-K_3**). Representative cryogenic TEM images of structures formed from a mixture of **C_{15}-COOH** and **C_{16}-K_3** in water. (b) At pH 5, only vesicles are observed. (c) Solutions at pH 8 show flat ribbons (indicated by white arrows). (d) At pH 10, the sample shows a mixture of vesicles and ribbons.

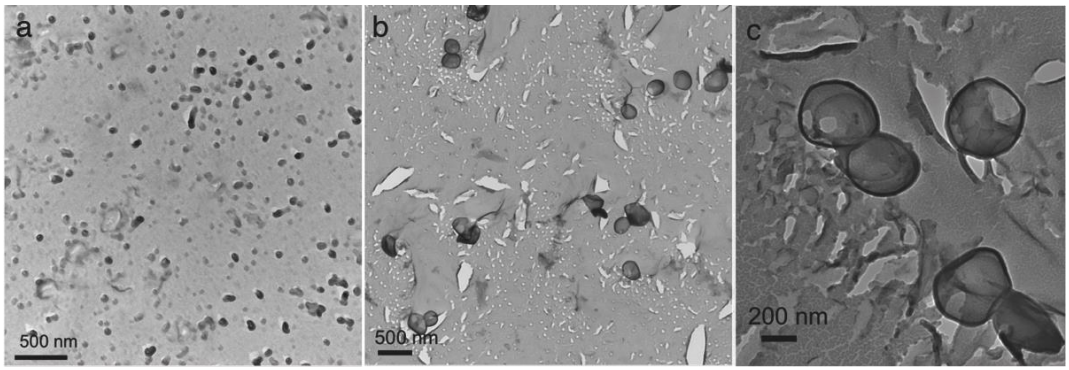

Figure 4.3. Coassembly of oppositely charged amphiphiles shows vesicles in aqueous solution. Quick-freeze/deep-etch TEM images of (**a**) micelles formed from molecule **C_{16}-K_3** alone (4 mM) and **(b, c)** faceted vesicles from a mixture of molecules **C_{16}-COOH** (12 mM) and **C_{16}-K_3** (4 mM) in water.

Simultaneously collected SAXS and WAXS data provide in situ information on the nanoscale morphology and atomic length-scale crystallinity, respectively. The processed SAXS/ WAXS data are shown in Figure 4.4 as a function of the scattering vector $q = 4\pi\sin\theta/\lambda$. For pH 4, 8, and 10, the SAXS intensity in the Porod region (q < 0.3 nm^{-1}) decreases as ~ q^{-2}, indicating scattering from two-dimensional structures.(36) We note that a collection of three-dimensional objects would cause a ~ q^{-4} decrease and one-dimensional fibers would show a q^{-1} decrease. These observations imply that the structures observed in TEM are composed of two-dimensional

bilayers. The features in the scattering pattern that would sense the 200-500 nm size of the vesicles occur below our 0.05 nm^{-1} cutoff range in q, so it is important to complement these SAXS measurements with the TEM images. Fitting the SAXS data to a bilayer model, as shown in Figure 4.5, gives the thickness information for each membrane (Table 4.2). We estimate that the thicknesses of the hydrophobic tail regions are ca. 3.1 nm for pH 3-7 and ca. 2.1 nm for pH >7, as shown in Figure 4.5. For pH 4, the hydrophobic thickness of 3.1 nm is slightly shorter than the length expected for two C16 alkyl tails in their fully extended conformation (~3.8 nm), whereas at pH 8, the thickness is consistent with the length of one $\mathbf{C_{16}}$ alkyl tail (~1.9 nm), as expected for a more highly interdigitated bilayer. The comparison of the WAXS data for the catanionic mixtures to the data for the pure cation (Figure 4.4) shows that the ordered packing of lipid tails arises only in structures formed due to electrostatic interactions between the oppositely charged amphiphiles. The WAXS data for the solution of cation alone (red dots in Figure 4.4) do not show diffraction peaks, as expected for a disordered micelle. By contrast, diffraction peaks appear in the WAXS region for the catanionic mixtures. For pH < 7 and pH > 10, the appearance of a single diffraction peak indicates that the molecules are packed in a two-dimensional hexagonal lattice, whereas the presence of two diffraction peaks for pH 8-9 indicates a rectangular-C structure. The lattice parameters and packing densities as a function of pH are listed in Table 4.1. Interestingly, very similar vesicle shapes are observed by TEM at pH 5 and 10 (Figure 4.2 b,d), while high aspect ratio nanoribbons are abundant at pH 8 (Figure 4.2 c).

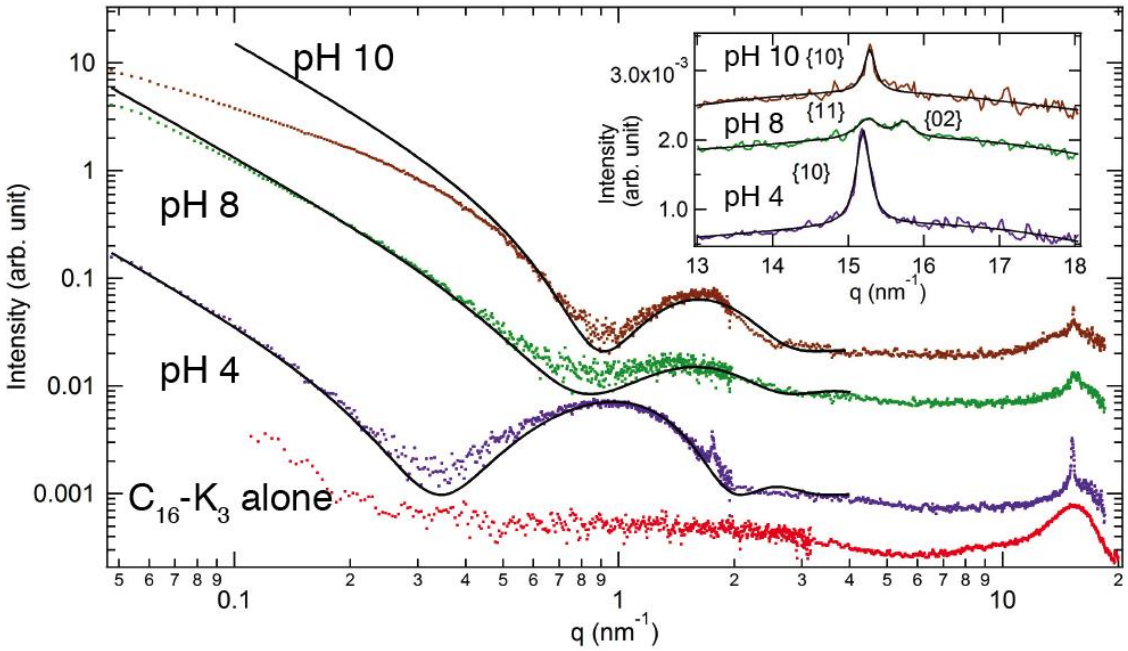

Figure 4.4. *In situ* small- and wide-angle x-ray scattering data showing the background subtracted scattered intensity versus the scattering vector q for cation $\mathbf{C_{16}\text{-}K_3}$ alone (bottom) and mixtures of acid $\mathbf{C_{16}\text{-}COOH}$ and cation $\mathbf{C_{16}\text{-}K_3}$ as the pH is increased from 4 to 10. The data sets are offset vertically for clarity. The black lines are the fits over the range $0.05 < q < 4$ nm^{-1}. Deviations in the fits are due to sample polydispersity. Inset: WAXS data and peak fits of the mixed cation/anion samples mixed samples indicate formation of crystalline lattices.

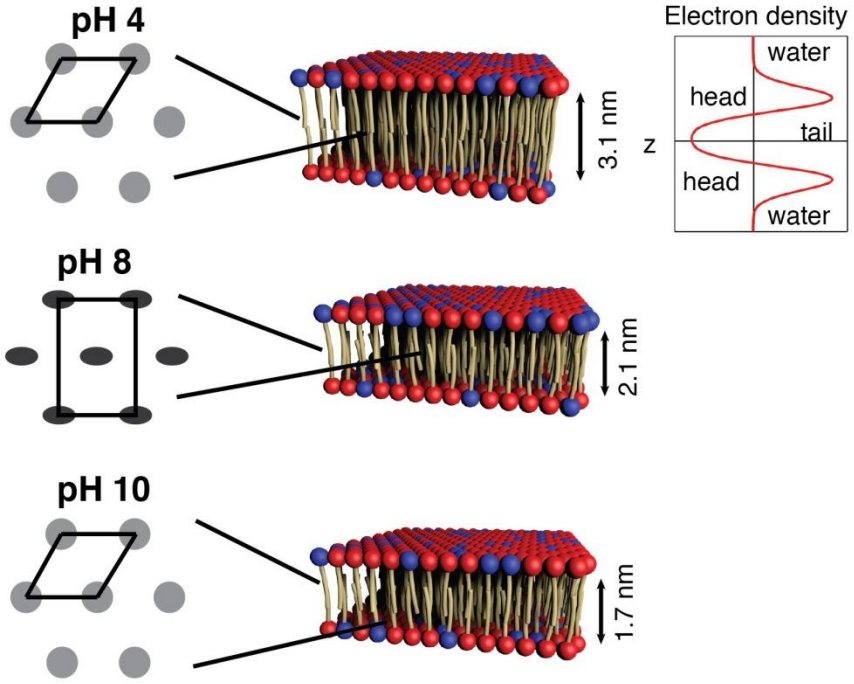

Figure 4.5. Schematic representations for the bilayer model at pH 4, 8, and 10 fitted to a bilayer model. Changes are observed in the thickness of the hydrophobic portion of the bilayer and the packing of the alkyl tails (green rectangles) into either an orientationally disordered hexagonal or a rectangular-C lattice.

Table 4.1. Lattice parameters obtained from x-ray scattering and atomistic MD simulation.

pH	2D Crystal lattice	Domain size (nm)	Lattice constant (nm)	Area per molecule (nm^2)	
	WAXS	WAXS	WAXS	WAXS	Atomistic simulation
3	Hexagonal	31	a = 0.477	0.197	/
4	Hexagonal	29	a = 0.477	0.197	0.2
7	Hexagonal	20	a = 0.474	0.195	/
8	Rectangular-C	21	a = 0.479 b = 0.800	0.192	0.2
10	Hexagonal	35	a = 0.474	0.195	/

Table 4.2. Membrane thicknesses obtained from x-ray scattering and atomistic MD simulation.

pH	Membrane thickness (nm)		Hydrophobic thickness (nm)	
	SAXS	Atomistic simulation	SAXS	Atomistic simulation
3	5.3	/	3.1	/
4	5.3	4.9	3.1	3.6
7	4.2	/	2.4	/
8	4.1	3.9	2.1	2.1
10	4.3	/	1.7	/

The hexagonal-rectangular-hexagonal transition as pH increases, illustrated in Figure 4.5, can be explained by the enhanced electrostatic attractions between the cationic and anionic molecules

in the pH 8-9 regime, where both the palmitic acid headgroups (pKa ~ 7.5) and the trilysine cationic molecules (pKa ~ 10.5) are expected to be nearly fully charged. In the low pH regime, the cations are fully charged and the degree of ionization of the anion is very low, while the reverse is true at high pH. This will be discussed below in conjunction with Figure 4.7c. The WAXS-derived area per tail (A_t = 0.192 nm^2) for pH 8-9 is less than the observed A_t = 0.197 nm^2 for pH 3-7 and A_t = 0.195 nm^2 for pH ≥ 10, which corresponds to the maximum packing density of the orientationally disordered (cylindrical) alkyl tails on a hexagonal lattice.(61) Therefore, a reduction in A_t necessarily requires an orientational ordering of the backbone plane of the alkyl tails and a distortion of the hexagonal lattice, which in this case leads to a rectangular-C lattice (Figure 4.5). The sum of integrated WAXS peak intensities, which is a measure of the degree of crystallization, is lower at pH 8 than at pH 4. Therefore, bilayers containing anionic molecules with a higher degree of ionization are less crystalline than bilayers with a lower fraction of ionized groups (i.e., the degree of ionization inversely affects the degree of crystallinity). While these experimental results clearly demonstrate structural changes at the nanoscale and mesoscale, they are not sufficient to identify the detailed mechanism and the behavior of the system at the level of individual molecules.

As indicated above, the X-ray experiments reveal that the membrane thickness can be controlled by adjusting the pH of the solution. To explore the mechanism of such change, molecular dynamics (MD) simulations are performed at both atomistic and molecular resolution.

Specifically, we simulate systems with a low degree of ionization of the palmitic acid groups to mimic the low pH data and a high degree of ionization to explain the intermediate-pH data. Moreover, to reveal the structures of the faceted vesicles experimentally observed at low pH, coarse-grained MD simulations are performed at the molecular resolution. That is, a series of

simulations are performed to reveal the morphological transformations across length scales and the origin of the observed shell geometries.

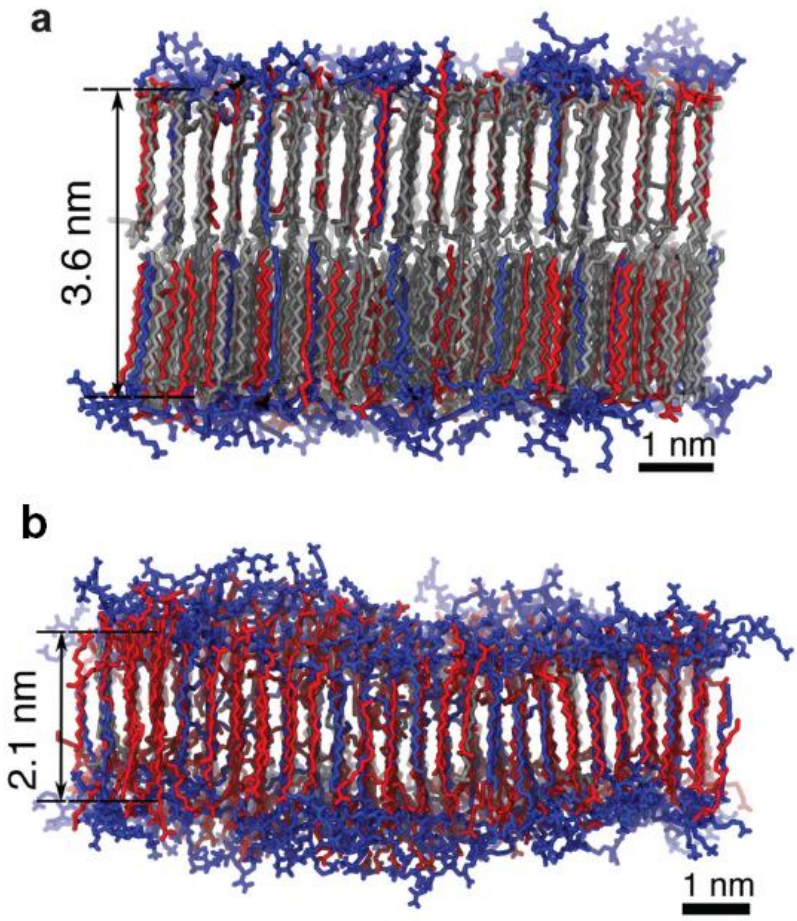

Figure 4.6. Atomistic MD simulation of bilayers. (a)(b) Snapshots of the typical bilayer configuration from the explicit solvent with (a) 30% and (b) 95% average degree of ionization of the anionic molecules. The cationic, anionic, and neutral anionic molecules are shown in blue, red and gray, respectively. Solvent (water) molecules are omitted for clarity. The hydrophobic thicknesses of the membranes are presented.

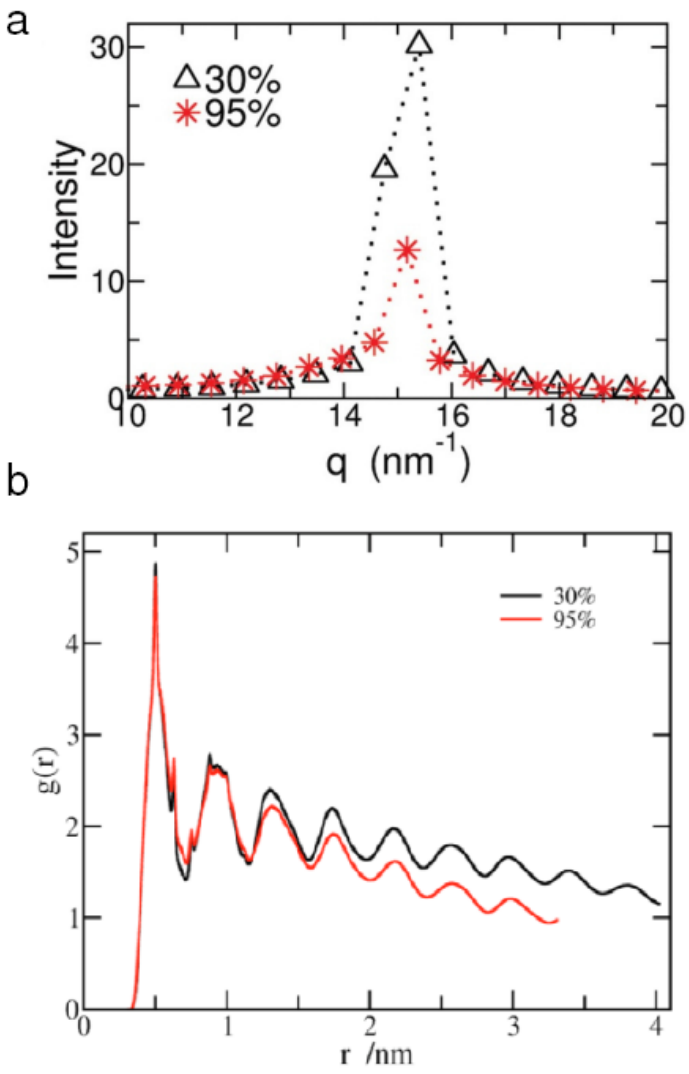

Figure 4.7. (a) Calculated scattering structure factor of the bilayer molecules (b) Radial distribution functions of the hydrocarbon atoms in the hydrophobic region.

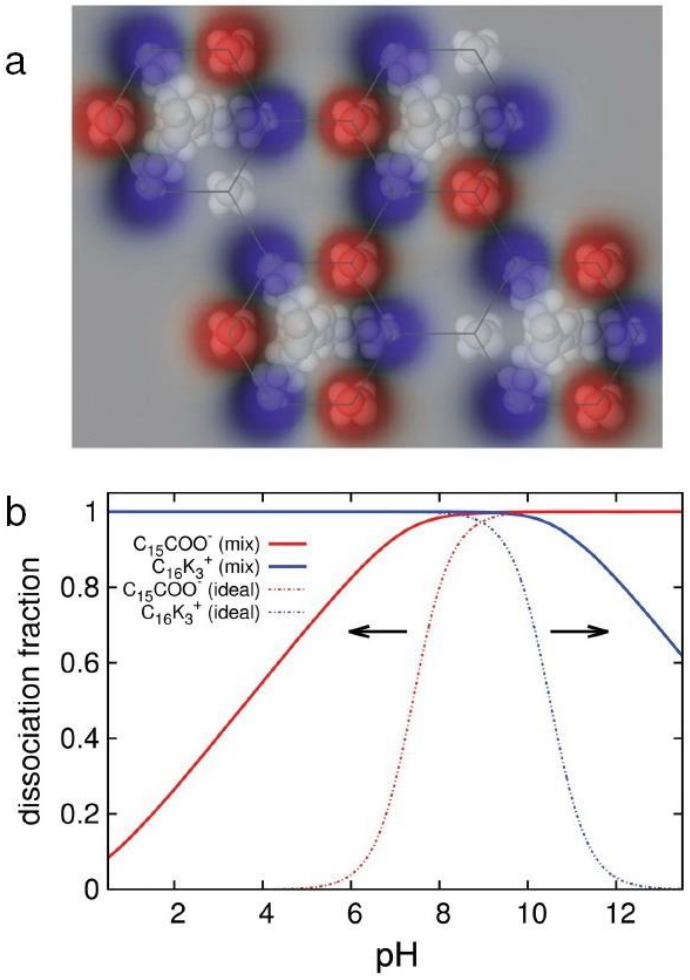

Figure 4.8. (a) Cartoon of the amphiphile head groups assumed to be projected into a two-dimensional hexagonal lattice formed by the amphiphile tails (not to scale). The heads of the amphiphiles are at the vertices of the hexagonal lattice and can be neutral (gray) or charged via dissociation with charge –1 (red) for the palmitic acid and +1 (blue) for the lysine groups; every three nearest-neighbor lysine side chains are connected via a common tail to form the trilysines. (b) The fraction of dissociated trilysine (blue curves) and palmitic (red curves) sites as a function of pH obtained by Monte Carlo simulation assuming the lattice shown in *d* for the distribution of cationic (+3) and anionic (-1) head groups for 94 mM monovalent salt concentration.

We first describe the atomistic simulations performed to describe the pH-induced bilayer thickness changes. The snapshots from long-time scale (up to 1 μs) atomistic molecular dynamics simulations show electroneutral systems with 30% (Figure 4.6a) and 95% (Figure 4.6b) average ionization of the palmitic acid molecules, which correspond roughly to pH 4 and 8, respectively. The bilayer structure is observed in both cases. Moreover, interdigitation between layers is observed only in systems with 95% ionization of the palmitic acid. Crystallization of the hydrocarbon tails is observed in both systems, as illustrated in Figure 4.6a,b. This is further supported by the diffraction peaks in the scattering structure factor of the hydrocarbon tails (Figure 4.7a), which is obtained from the Fourier transform of the corresponding radial distribution function (Figure 4.7b). The positions of the peaks in Fourier transform (Figure 4.7a) agree well with those observed in the WAXS data at pH 4 and 8, respectively (Figure 4.4). Furthermore, the scattering structure factors in Figure 4.7a suggest a relatively weaker degree of crystallization at 95% ionization of acid C_{15}-COOH, which is consistent with the smaller integrated intensity at pH 8 in WAXS. This difference in crystallinity indicates that a subtle balance among ionic correlations (which, as explained below, generate net attractions), van der Waals interactions, and chemical acid-base equilibria determines the crystalline structure. The area per tail is found to be ~0.2 nm^2 in both the 30 and 95% systems, which is consistent with the WAXS data (Table 4.1). The rectangular-C packing of the hydrocarbon chains was not reproduced by our atomistic MD simulations, which may be due to the limited length scale (<10.5 nm) and time scale (1 μs) of the simulation. Another reason may be attributed to the force field, which was not parameterized for crystalline phases, where the configuration entropy likely plays a more significant role than in the liquid phase. Monte Carlo simulations show how the pH is related to the degree of ionization of the molecules (Figure 4.8a). When the cationic and

anionic amphiphiles coassemble (Figure 4.8b), the dissociation is more favorable when compared to the cases of isolated anionic and cationic molecules in solutions.(62, 63) Therefore, headgroups are charged over a broad range of pH values. Removing salt enhances this effect

Also indicated in Figure 4.6a,b are the MD-derived thicknesses of the hydrophobic tail regions of the membranes, which are found to be 3.6 nm for the 30% ionization system and 2.1 nm for the 95% ionization system and are consistent with the corresponding SAXS data in Figure 2b. The change of the bilayer thickness can be interpreted based on the imbalance between the excluded volume of the large cationic headgroups and the relatively small cross section of the hydrophobic tails, which is compensated by the relatively high proportion of uncharged palmitic acid **C_{15}-COOH** at low pH. When the pH is elevated, the imbalance between the excluded volumes of the headgroups and tails increases because there are not enough uncharged palmitic acid molecules to fill the voids. This imbalance is energetically unfavorable and can be compensated by the interdigitation of the hydrophobic tails in the upper and the lower leaflets, as illustrated in Figure 4.9, to maintain the attractive hydrophobic interactions.

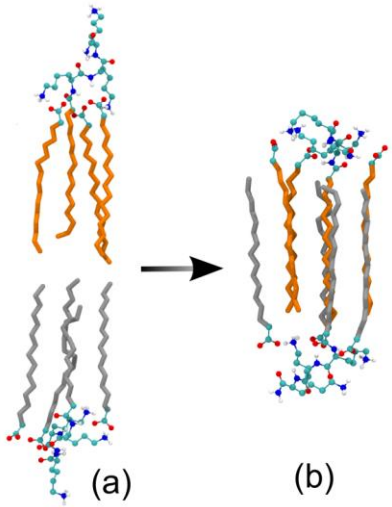

Figure 4.9. Bilayer structure (a) before (simulation time of 0 ns) and (b) after (1 μs) the interdigitation of the upper leaflet (hydrocarbons in orange) and the lower leaflet (hydrocarbons in silver) in the 95% system. Only a small fraction of the system is displayed for clarity. The process of the interdigitation is predominately induced by an increase of the hydrophobic interaction ($\Delta E = E_{after} - E_{before} = -3.56\ k_BT/nm^3$) relative to the ionic correlation between the opposite layers ($-1.38\ k_BT/nm^3$) .

A simple estimate of the electrostatic correlations can explain the formation of the crystalline lattices on the vesicles. The electrostatic correlations are quantified by $l_B = e^2/4\pi\varepsilon_0\varepsilon_r k_BT$, the length at which the electrostatic interaction is comparable with the thermal energy k_BT (where e is the unit charge, ε_r is the relative permittivity of the medium, and ε_0 is the dielectric permittivity of vacuum). The hydrocarbon tails are nonpolar with $\varepsilon_r \approx 1$, while $\varepsilon_r \approx 80$ in water. Consequently, the headgroups located between polar water and nonpolar tails experience a weaker dielectric response (typically the mean ε_r between the two media, i.e., $\varepsilon_r \approx 40$), resulting in $l_B \approx 1.4$ nm,

which is approximately three times the interchain distance observed by WAXS, $d \approx 0.5$ nm. The electrostatic energy necessary to hold together one t3 and three -1 chains into a four-tail bundle is then $E_e \approx 3(-1)l_B k_B T/\mathrm{d} \approx -9\ k_B T$, in agreement with the estimates from atomistic MD simulations of about -2.8 $k_B T$ (30%) or about -2.4 $k_B T$ (95%) per NH_3^+-COO^- ion pair for their cohesive energy, which is the effective interaction between them mediated by the water environment. Adding the hydrophobic attraction, which is around -20 $k_B T$/chain from atomistic MD simulations gives $E_b \approx -90\ k_B T$. In contrast to ionically driven assembly of incompatible molecules,(64) the assembly discussed here induces short-range attractions among dissimilar molecules of opposite charge, explaining the stability of the ionic crystalline bilayer up to salt concentration n = 500 mM NaCl. As shown in Figure 4.10b, a single diffraction peak in the WAXS region shows up in all four curves, indicating that the hydrophobic tails are still crystallized into a hexagonal lattice even at high salt concentrations.

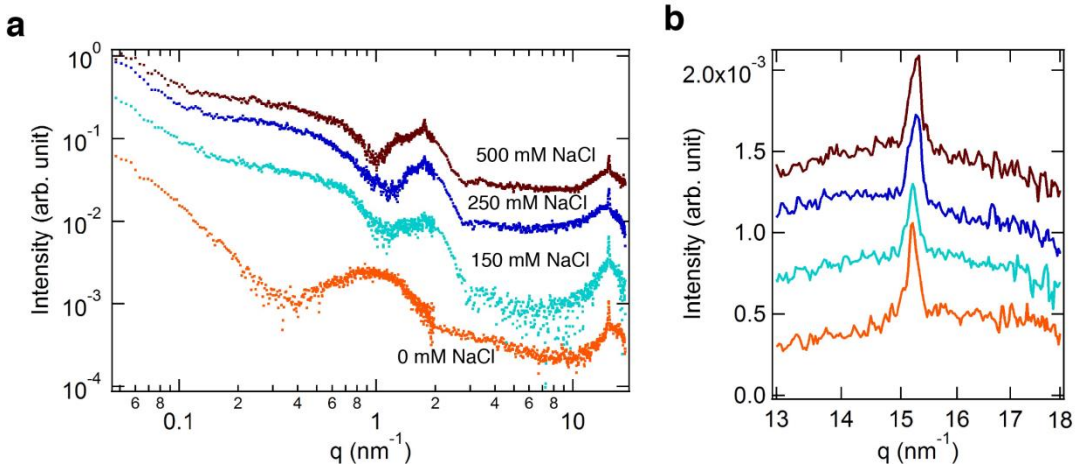

Figure 4.10. X-ray scattering from bilayers in salt solutions. (a) SAXS-WAXS data showing the scattered intensity versus the scattering vector q for mixtures of acid C_{16}-COOH and cation C_{16}-K_3 in 0, 150 mM, 250 mM and 500 mM NaCl solutions (from bottom to top) at pH4.

The three data sets are offset vertically for clarity. The broad oscillations in the SAXS region are consistent with form factors for catanionic bilayers. The small peak at 1.77 nm^{-1} is due to suspended (undissolved) solid palmitic acid. (b) WAXS data for the mixture in 0, 150, 250 and 500 mM NaCl solutions (from bottom to top).

Our results show that though electrostatic interactions can induce the formation of rectangular lattices in membranes of short ionic amphiphiles, the irregular faceted shapes seem to be prominent when the crystalline lattice is hexagonal, which is the ubiquitous symmetry in crystalline shells. To further reveal the morphology at mesoscale level, coarse-grained MD simulations are performed using the MARTINI force field.(58, 59) Under MARTINI force field, four heavy atoms are represented by one interaction bead on average (Figure 4.11e). Therefore, the atomistic structure is semiquantitatively preserved. In Figure 4.11a, a MARTINI MD simulation snapshot of the optimal tail packing shows that the internal structure of the vesicle bilayer is not homogeneous. The vesicle surface can be thought as a two-component shell, where one component represents flat crystalline domains while the second component represents the high curvature, liquid-like boundaries between the hard facets. The bilayer packing and thickness in the flat areas are in agreement with the atomistic MD simulations (Figure 4.6a). Given that the size of the crystalline domains obtained by SAXS is $\sim 30 \times 30$ nm^2, our results suggest that small vesicles (<100 - 200 nm in diameter), in which only few crystalline domains cover their surfaces, are more likely to be faceted into polyhedral structures with low symmetry (lower than the icosahedra) observed by TEM (Figure 4.11b-d). On the other hand, large vesicles in which the defects spread over many boundaries have nearly spherical accreted shapes (Figure 4.2b). The MARTINI MD simulations (Figure 4.11a) show that the edges of the polyhedral are fluid-like

bilayers. We note the possibility that a fluid-like region may exist on the polyhedron only if the packing lattice is hexagonal. This is because the phase diagram for tail packing, as observed in Langmuir films,(61) allows fluid-hexagonal coexistence. In comparison, there does not exist an obvious coexistence region between rectangular-C and fluid phases in monolayers,(61) which may explain why the vesicles are not stable at higher degrees of ionization when the pH is 8 (Figure 4.2b).

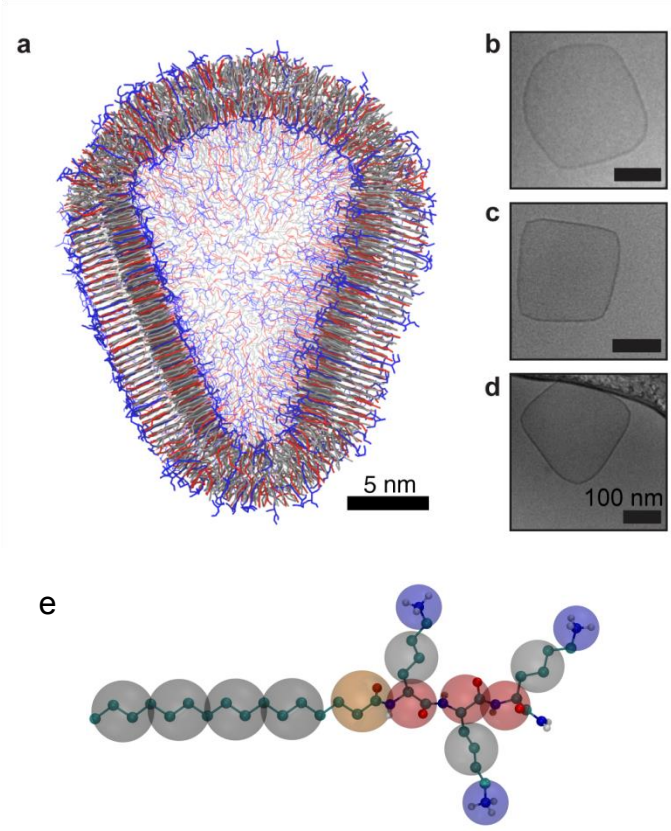

Figure 4.11. Faceted vesicle observed in simulation and TEM. (a) A representative snapshot of the MARTINI coarse-grained MD simulation where half of the vesicle is omitted for clarity. The ionization degree of the anion is 30% and the molecules are color coded as in Figure 4.8a and 4.8b. (b–d) TEM images of low symmetry, highly faceted vesicles observed in the mixture at pH

5. (e) Mapping methodology of the **C_{16}-K_3** molecule from GROMOS96 atomistic force field to MARTINI coarse-grained force field (larger transparent beads). Different colors in the MARTINI topology represent different interaction types (grey for apolar, orange for intermediate polar, red for polar, blue for charged).

4.4. Summary

In summary, the pH acts as a switch that controls the crystal structure and therefore the mesoscale morphology of bilayers of coassembled ionic amphiphiles. The low symmetry faceted shapes are due to crystalline domains induced by ionic correlations. These 2D ionic correlations, as in ionic bonding, are not sufficiently screened by the bulk salt, generating membranes that are stable even at high salt concentrations. The ionic non-icosahedra faceted vesicles are not homogeneous and the facets have a nonzero Young's modulus, akin to crystallized double-tail surfactants(65) or chemically bonded membranes.(66) Their crystalline lattice and morphology, however, are determined by the solution pH. The observed irregular faceted shapes arise only in hexagonal crystalline lattices, where crystalline domains are separated by soft interfaces that bend to release stress. At intermediate pH values, the induced crystalline transition opens the closed membranes. Faceting also arises when strongly charged molecules, such as DNA, are adsorbed into oppositely charged lipid vesicles,(67) which suggests that the geometries found here may also arise in the adsorption of multivalent ions on lipids(68) or cellular membranes.(69) Our results also suggest that spherical-to-faceted reversible transitions can be induced in cationic vesicles by adding (or chelating) metallic multivalent ions,(70) similar to the halophilic archaeon *Haloarcula japonica*, which undergoes a triangular to spherical morphological change after lowering the magnesium concentration in the medium,(71) in addition to other possible kinetic

growth mechanisms of faceted geometries.(72) The findings improve our understanding of how molecules self-assemble into robust aggregates with well-defined structures and surface composition stable at physiological ionic conditions and/or high salt concentrations, such as unusual viral capsids,(40) carboxysomes,(24, 41, 42) or halophilic organisms.(23, 43) We foresee applications of these vesicles to the design and fabrication of functional nanoscale containers. Moreover, our work demonstrates that a local molecular scale change in structure induced by adjusting the solution pH leads to mesoscale structural changes. This process elucidates a mechanism by which chemical energy transforms into mechanical energy, which could be exploited in the design of bioengineered synthetic nanomachines.

Chapter 5. Crystalline Polymorphism Induced by Charge Regulation in Ionic Membranes

5.1. Introduction

Nature uses electrostatic interactions among positively and negatively charged groups to induce the organization of biomolecules into highly complex structures that respond to ionic changes. (73, 74) The structure of the aggregates at specific ionic conditions is intimately related to their function. Therefore, understanding the mechanisms that control the structure of molecules with hydrophobic and polar groups at physiological conditions is of great importance in molecular biology and biotechnology. In particular, amphiphilic molecules that have polar ionizable groups, such as proteins and lipids, can change their structures and functions in response to the pH and the concentration of ions in the solution (75) thereby affecting their physical properties and functions. For example, the structure of lipid membranes affects the structure and activity of membrane-bound proteins.(76-78) Furthermore, the intermolecular packing density and structure are known to affect the molecular diffusion rates of water and ions across membranes.(79, 80) Changing the packing density of molecules within membranes could also be useful for controlling encapsulation and release efficiency of molecules inside a vesicle.(81) Additionally the spacing between amphiphilic molecules within a membrane may control the capacity to encapsulate or release amphiphilic molecules within the bilayer, such as the proteins that reside inside lipid membranes (82) and possibly hydrophobic drugs. Therefore, it is important to explore different approaches to adjust the structure of lipid membranes.

At the mesoscale level, crystalline membranes are essential for many bacteria, bacterial microcompartments (24) and archaea (23) to survive in extreme environments including high

salinity. These organisms take various polyhedral geometries that are characteristic of crystalline closed shells. (83, 84) The presence of polar and hydrophobic groups in their wall envelopes and the fact that they survive at low pH values and disintegrate or become spherical (the shape of closed liquid membranes) when divalent metal ions are chelated, (23, 85) suggest that their crystallization is triggered by electrostatic interactions. Divalent ion induced crystallization of anionic membranes has been recently studied,(68, 86) but crystallization changes induced by pH variations in bilayers are unknown. Here, we study pH effects in crystalline membranes of coassembled amphiphiles with carboxylate and dilysine headgroups, whose pK_a values are about 5.5 (87)and 10 (88), respectively.

Simple mixtures of cationic and anionic amphiphiles exhibit some of the behaviors of highly complex natural membranes. They self-assemble into a large variety of membrane structures, including closed-shell vesicles, via the electrostatic interactions between the cationic and the anionic surfactant headgroups.(18, 21, 89) Catanionic vesicles formed from coassembled cationic and anionic amphiphiles show stability for long periods and can be formed spontaneously without sonication or extrusion.(18, 49) The assembly of such amphiphilic molecules with ionizable groups into bilayer membranes offers a unique opportunity to systematically analyze the subtle balance of electrostatics, entropy, hydrophobicity and short-range interactions in their structure. Therefore, these membranes can provide important insight about membrane dynamics and may have useful biomedical applications such as drug delivery.(6)

The phase behavior of cationic and anionic amphiphiles is determined by many parameters, such as the amphiphile mixing ratio, concentration and molecular structure.(22, 90, 91) In Chapter 4, we discussed mixtures +3 cation and -1 anions forming catanionic membranes. The

molecular packing of these membranes showed a hexagonal to rectangular-C to hexagonal phase transition with increasing pH, resulting in significant changes to the membrane morphology. These membranes appear to be stable to salt (up to 500 mM NaCl) in contrast to other ionic coassembled systems that are very sensitive to charge screening. (51, 92) To be useful as models for biological membranes or for potential applications in drug delivery, the range of accessible temperatures is very limited, so other parameters to control crystalline order must be considered. The pH range of physiological media can vary considerably between different tissues. For example, it is known that microenvironment in tumors is more acidic than in normal tissues.(93-95) Therefore, it is important to understand the internal membrane structure and the consequent membrane morphology as function of pH. Since the variation of pH within a particular localized environment is small, other parameters like molecular structure must also be considered to control the internal membrane structure at a specific pH.

We study here the molecular packing in catanionic membranes formed from +2 cations and -1 anions (Fig. 5.1a) as a function of solution pH and amphiphile tail length (Fig. 5.1b). The solution pH controls the degree of ionization of the cationic and the anionic headgroups, while the tail length determines the strength of the intermolecular van der Waals interactions, as shown by atomistic molecular dynamics (MD) simulations. Simultaneous small- and wide-angle X-ray scattering (SAXS and WAXS) are utilized to measure the membrane thickness and the crystalline packing of the amphiphiles in the membrane plane.

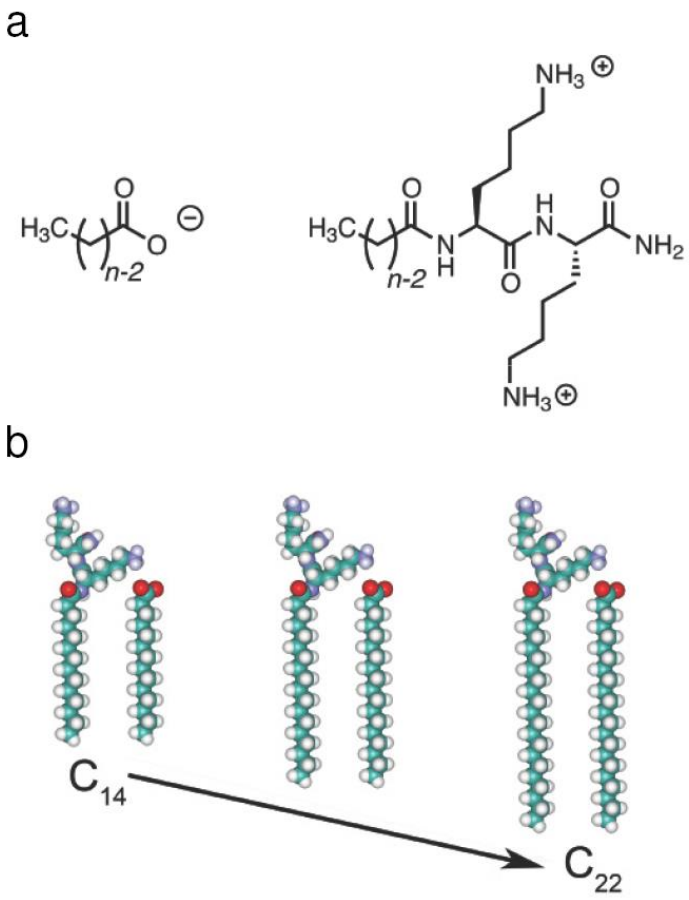

Figure 5.1. (a) Charged amphiphiles used for ionic coassembly: –1 fatty acid (**C_{n-1}-COOH**) with +2 dilysine (**C_n-K_2**). (b) Schematic representations of the pairs of cation and anion with different tail length from *n*=14 to *n*=22 used to form bilayers.

5.2. Materials and Methods

5.2.1. Material Synthesis and Sample Preparation

All Fmoc-amino acids and Rink 4-methylbenzhydrylamine (MBHA) amide resin were purchased from Novabiochem Corporation (San Diego, CA). All other reagents and solvents for peptide synthesis were purchased from Aldrich, Mallinckrodt, or TCI and used as provided. The

synthesis of each *N*-alkanoyl dilysine (**C_n-K_2**) was performed using standard solid-phase peptide synthesis methods as described previously in Chapter 4. Briefly, peptides were grown on Rink Amide MBHA resin, using 4.0 equivalents of an Fmoc-protected amino acid, 3.95 molar equivalents of 2-(1*H*-benzotriazole-1-yl)-1,1,3,3-tetramethyluronium hexafluorophosphate (HBTU) and 6 equivalents of *N*,*N*-diisopropylethylamine (DIEA) for each residue coupled to the resin. The palmitic acid tail was subsequently coupled to the N-terminus of the peptide by adding 8.0 molar equivalents of each fatty acid to the peptide in the presence of 7.95 molar equivalents of HBTU and 12 molar equivalents of DIEA. The peptide was then cleaved from the resin and amino acid side groups were deprotected in 95% trifluoroacetic acid (TFA), 2.5% triisopropylsilane (TIS), and 2.5% deionized water. TFA was removed by rotary evaporation. Peptides were purified by preparative HPLC on a Varian Prostar 210 HPLC system using a Waters Atlantis C-18 30 × 250 mm column under a slow elution gradient of 98% to 0% water and acetonitrile (0.1% TFA). Product-containing fractions were confirmed by ESI mass spectrometry (Agilent 6510 Q-TOF LC/MS), combined, and lyophilized after removing acetonitrile by rotary evaporation to afford the desired amphiphiles as their trifluoroacetate salts.

Cationic amphiphiles were first dissolved in deionized water (resistivity ~ 18 MΩ.cm) at a concentration of 4 mM (C_{16} –C_{22}) or 12 mM (C_{14}). To prepare each sample, the cation solution was added to a centrifuge tubes containing three equivalents of the solid fatty acid with the same hydrocarbon tail length. The solution concentrations were picked to ensure coassembly of amphiphiles. The anionic amphiphiles used in the present study are not water soluble at room temperature. To dissolve the fatty acids and thus to promote coassembly in solution, the mixtures were heated to 80 °C for 60 min. (C_{22} samples were heated to 90°C to ensure complete dissolution.) The samples were cooled to room temperature and centrifuged at approximately

2000 rpm for 5 min to remove precipitates, which were likely the undissolved fatty acids. The pH of these solutions after heating and cooling was approximately 3. The pH of each sample (except pH 3) was adjusted with 1 M NaOH, just prior to X-ray measurements. It is worth noting that no assembly was observed for samples prepared using a shorter C_{12} tail at 4mM.

5.2.2 Methods

SAXS and WAXS experimental setup is discussed in Chapter 3.3

5.2.3. Theory and Simulations

Theoretical calculations and simulations were conducted by Dr. Baofu Qiao in Professor Monica Olvera de la Cruz's group.

Classical atomistic MD simulations are performed using the package GROMACS (version 4.5.5).(96) The latest version of the GROMOS96 54A7 United-Atom force field (57) is employed for the amphiphile molecules with water molecules modeled by the SPC model. The force field has been validated in Chapter 4 in reproducing well the crystalline structures of mixtures of trivalent cationic (**C_{16}-K_3**) and monovalent anionic (**C_{15}-COOH**) amphiphiles. Two systems representing different hydrocarbon tail lengths of C_{14} and C_{16}, respectively, are investigated. In both of the systems, the ionization degree of palmitic acid molecules of 30% is employed to mimic the low pH condition (pH ≈ 3). The simulations are started from pseudo-bilayer structures (akin to Fig. 5.12a) to speed up the process for equilibrium structures. The electrostatic interactions are calculated via the Particle Mesh Ewald method (97) and the short-range Lennard–Jones 12-6 interactions are truncated at 1.2 nm with the long-range dispersion corrections applied to the energy and pressure. The simulations are performed for a

duration of 50 ns for the C_{14} system and a longer duration of 400 ns for the C_{16} system. The temporal calculations of the area per amphiphile molecule support that around 20 ns is long enough to equilibrate the bilayer structures for both systems. Therefore, the trajectories from the last 20 ns for the C_{14} system, the last 100 ns for the C_{16} system, are employed for the subsequent data collection and analysis.

5.3. Experimental Results and Discussion

To understand the effect of solution pH on catanionic mixtures, we first investigated solutions of oppositely charged amphiphiles with a given tail length. Specifically, we observed the coassembly of *N*-palmitoyl dilysine (**C_{16}-K_2**) and palmitic acid **(C_{15}-COOH**). In aqueous solution by itself, **C_{16}-K_2** forms micelles and **C_{15}-COOH** is insoluble. Cryo TEM shows that C_{16} mixtures form facetted bilayer vesicles at pH 3. (Fig. 5.2)

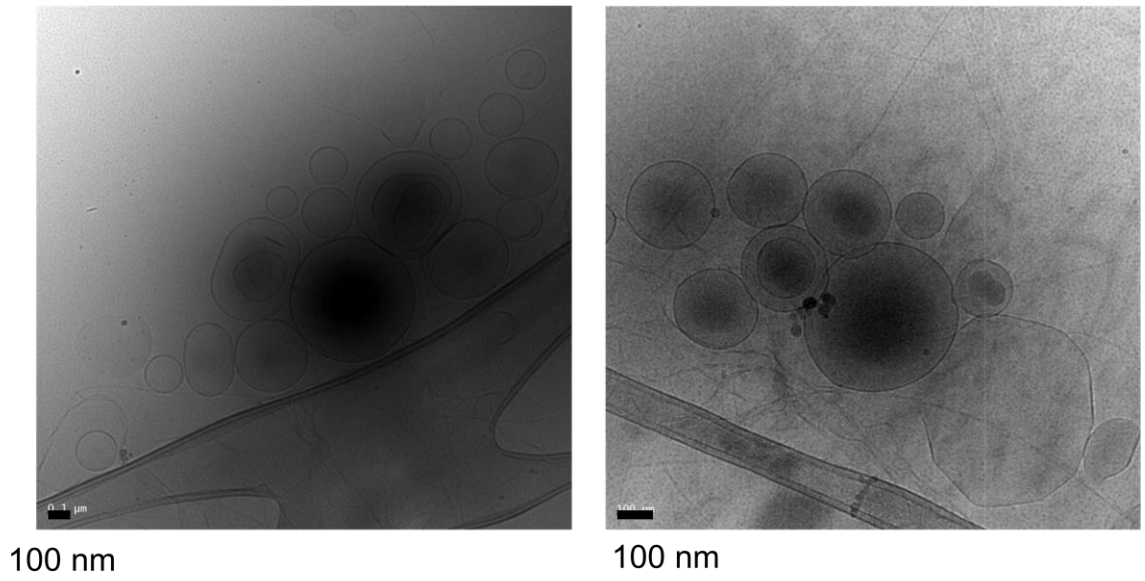

Figure 5.2. Representative cryogenic TEM images of structures formed from a mixture of **C_{15}-COOH** and **C_{16}-K_2** in water at pH3.

Simultaneously collected SAXS-WAXS data provide in situ information on the nanoscale morphology and atomic length scale crystallinity, respectively. Fig. 5.3a shows the processed SAXS data for the mixture of these amphiphiles as a function of scattering vector ($q=4\pi sin\theta/\lambda$) at various solution pH values. Regardless of the solution pH, the SAXS intensity in the Porod region ($q < 0.3$ nm^{-1}) decreases as $\sim q^{-2}$, indicating scattering from two-dimensional membranes, as illustrated in Fig. 5.4. The SAXS-derived estimates for the bilayer membrane thicknesses are listed in Table 5.1. For C_{16} mixtures, the bilayer thickness is highest at pH 3 (~ 5.8 nm). For pH ≥ 6.5, the bilayer thickness is nearly a constant ~ 4.0 nm. The reduction in the bilayer thickness with increasing pH has been previously also observed for mixtures of *N*-palmitoyl trilysine (**C_{16}-K_3**) and **C_{15}-COOH** in Chapter 4 and was explained by atomistic MD simulations, which showed that at high pH there exists extensive interdigitation of the hydrophobic tails of the molecules comprising the two leaflets of the bilayer.

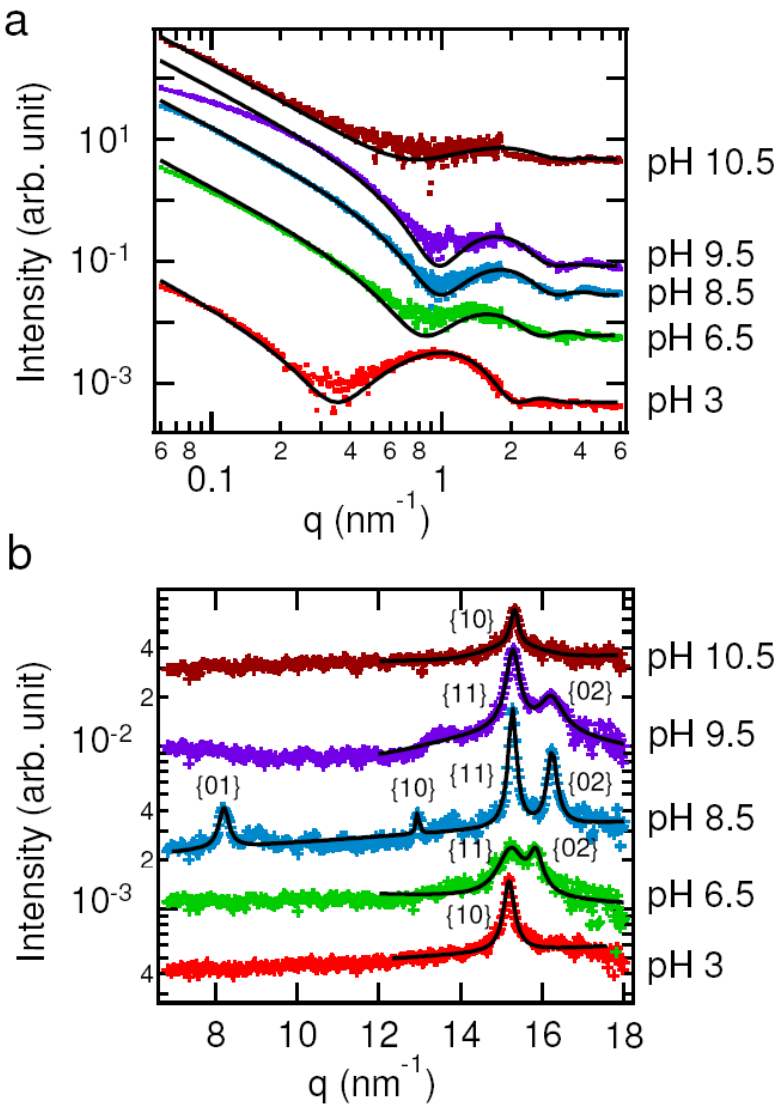

Figure 5.3. (a) In situ small- and (b) wide-angle x-ray scattering data showing the background subtracted scattered intensity versus the scattering vector q for mixtures of anion **C_{15}-COOH** and cation **C_{16}-K_2** as the pH is increased from 3 to 10.5. The data sets are offset vertically for clarity. The black lines are the fits. Deviations in the SAXS fits are likely due to sample polydispersity.

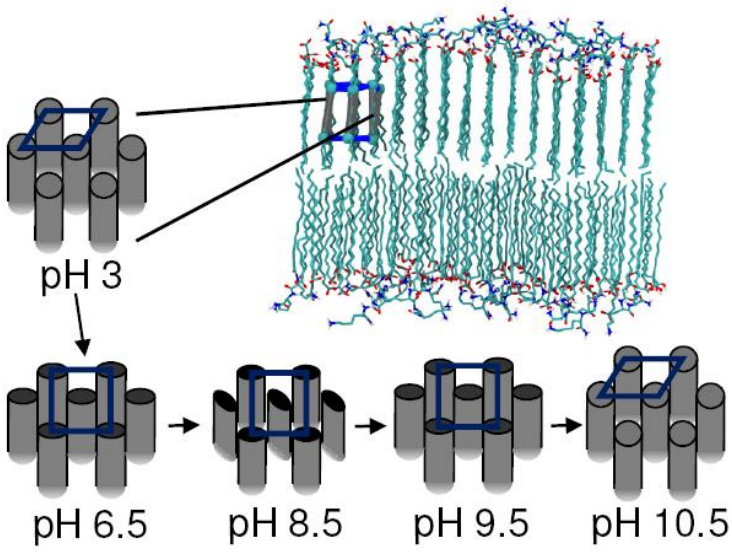

Figure 5.4. Schematic representations for the bilayer model at pH 3, 6.5, 8.5, 9.5 and 10.5. Changes are observed in the packing of the alkyl tails into a hexagonal, a rectangular-C or rectangular-P lattice.

Table 5.1. Lattice parameters and membrane thicknesses obtained from x-ray scattering for mixtures of anion **C_{15}-COOH** and cation **C_{16}-K_2**.

pH	**Crystal form**	**Domain size (nm)**	**Lattice const (nm)**	**Area per molecule (nm^2)**	**Membrane thickness (nm)**
3	Hexagonal	24	a = 0.477	0.197	5.8
6.5	Rectangular-C	13	a = 0.483	0.192	4.2
			b = 0.795		
8.5	Rectangular-P	33	a = 0.484	0.188	3.8
			b = 0.775		
9.5	Rectangular-C	23	a = 0.484	0.188	4.0
			b = 0.775		
10.5	Hexagonal	36	a = 0.474	0.195	3.3

While the features in the SAXS data describe the nanometer-scale morphology of the bilayers,

the diffraction peaks in the WAXS region ($q \geq 7$ nm^{-1}) arise from the crystalline packing of alkyl tails of the molecules forming the bilayer membranes. Fig. 5.3b shows the WAXS data for the C_{16} catanionic mixture at different pH values. For the C_{16} catanionic mixtures, the number and the position of the diffraction peaks, and thus the crystalline packing of the alkyl tails, sensitively depend upon the solution pH. For pH 3 and pH 10.5, a single diffraction peak is observed and is putatively attributed to a hexagonal packing of the molecular tails. This is because the cross-sectional area/tail A_t calculated for pH 3 and pH 10.5 (Table 5.1) are close to $A_t \sim 0.2$ nm^2 for cylindrically disoriented alkanes in their fully extended conformation.(61) By contrast, solutions at pH 6.5 and pH 9.5 exhibit two diffraction peaks, which are indicative of a rectangular-C (centered) structure in which each unit cell is occupied by two molecules with the same orientation of the molecular backbone planes. At pH 8.5, four diffraction peaks are observed and the peak positions indicate a 2D rectangular-P (primitive) lattice with two molecules per unit cell. Within a rectangular-P unit cell, the orientation of the alkyl tail backbone plane for the molecule at the center of the cell is different from that for the alkyl tails occupying the unit cell vertices, as shown schematically in Fig. 5.4. The observed diffraction peaks in the low q region are not due to ordering of the cationic headgroups. We consider here the following two cases:

Case 1. This case describes the scenario that there is cationic headgroup ordering with the same backbone orientation for every molecule. (Figure 5.5a) The real space lattice vectors for this oblique unit cell **a'** and **b'** can be written in terms of the rectangular unit cell lattice vectors **a** and **b** without headgroup ordering as:

$$\mathbf{a}' = \frac{3}{2}\mathbf{a} - \frac{1}{2}\mathbf{b} \tag{5.1}$$

$$\mathbf{b}' = \frac{3}{2}\mathbf{a} + \frac{1}{2}\mathbf{b} \tag{5.2}$$

The corresponding reciprocal space lattice vectors will then be

$$\mathbf{a}'^* = \frac{1}{3}\mathbf{a}^* - \mathbf{b}^* \tag{5.3}$$

$$\mathbf{b}'^* = \frac{1}{3}\mathbf{a}^* + \mathbf{b}^* \tag{5.4}$$

By rearranging,

$$\mathbf{a}^* = \frac{3}{2}(\mathbf{a}'^* + \mathbf{b}'^*) \tag{5.5}$$

$$\mathbf{b}^* = \frac{1}{2}(\mathbf{b}'^* - \mathbf{a}'^*) \tag{5.6}$$

It can be seen that the observed rectangular-P (10) and (01) reflections are forbidden for this lattice. Therefore, we can rule out the contribution from ordering of cationic headgroups to the diffraction peaks.

Case 2. This case describes the scenario that there is cationic headgroup ordering while tails pack into a rectangular-P structure. (Figure 5.5b) In this phase, the backbone orientation is different for the molecule at the center and corner of the rectangular cell. The real space lattice vectors for this unit cell $\mathbf{a}''$ and $\mathbf{b}''$ can be written in terms of the rectangular unit cell lattice vectors **a** and **b** without headgroup ordering. The structural factor can be calculated to be

$$S = f_B + f_B' e^{i2\pi(\frac{h+k}{2})} + f_A\left[e^{i2\pi(\frac{h}{6}+\frac{k}{2})} + e^{i2\pi(-\frac{h}{6}+\frac{k}{2})}\right] + f_A'\left[e^{i2\pi(\frac{h}{3})} + e^{i2\pi(-\frac{h}{3})}\right] \tag{5.7}$$

where f_B and f_B' are the form factors of the cationic molecules at the corner and at the center of the rectangular cell, respectively. f_A and f_A' are the form factors of the anionic molecules at the

(5.8)

corner and at the center of the rectangular cell. The corresponding real space lattice vectors $\mathbf{a}''$ and $\mathbf{b}''$ are

$$\mathbf{a}'' = 3\mathbf{a}$$
$$\mathbf{b}'' = \mathbf{b} \qquad (5.9)$$

The (10) reflection for this lattice, which should correspond to the (1/3 0) reflection for the original rectangular-P lattice (q = 4 nm^{-1}) is not observed in the X-ray data, so this scenario is also ruled out.

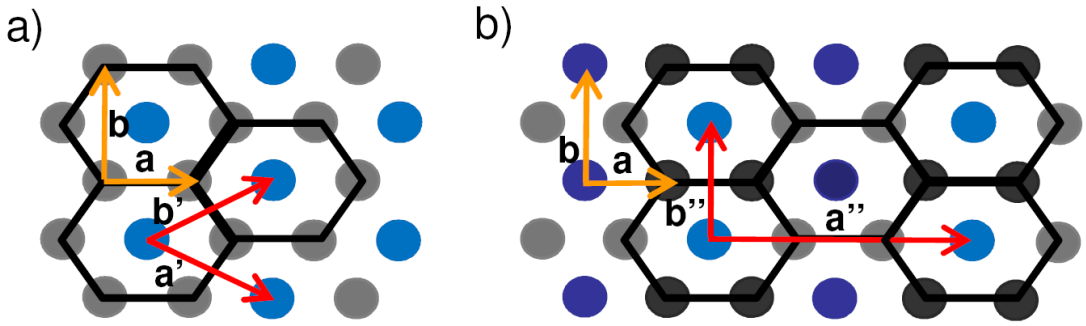

Figure 5.5. (a) Model for considering a real space lattice with ordered cationic headgroups (blue circles) while all the tails are packed in a rectangular-C phase. Red arrows represent the real space vectors for the new unit cell with ordered cationic molecules; orange arrows represent the real space lattice vectors for the unit cell with only tail packing as shown Figure 5.3. (b) Real space lattice with the cationic headgroup ordered (blue circles) while all the tails are packed in rectangular-P. Pale and dark grey circles represent anionic molecules with different tail orientations occupying the center and the corner of the original rectangular-P unit cell. Pale and dark blue circles represent cationic molecules with different tail orientations occupying the center and the corner of the original rectangular-P unit cell. Red arrows represent the real space vectors for the new unit cell; orange arrows represent the real space vectors for the unit cell with

only tail packing.

The pH-dependent effects on the 2D crystal phase and area/tail (A_t) can be qualitatively explained by the pH-driven ionization of the cationic and the anionic components of the membrane. Specifically, at low pH the carboxylic acid headgroups (pK_a ~ 5.5) (87) are largely not dissociated (neutral), whereas the amines in the dilysine headgroups (pK_a ~ 10) (88) are mostly protonated (cationic). In catanionic mixtures, the pK_a value for the anion is expected to be lowered and the pK_a value for the cation is expected to be higher compared to their bulk pK_a values.(62, 84, 98) At intermediate pH (~8.5), both the carboxylic acids and the lysine amines are fully ionized, whereas at very high pH the carboxylic acids are fully ionized and the lysines are mostly neutral. Therefore the attractive electrostatic interactions between the cations and the anions reach a maximum at intermediate pH (Table 5.1).

The observed hexagonal – rectangular C – rectangular P – rectangular C – hexagonal sequence of 2D crystal phase transitions with increasing pH (Fig. 5.4) is consistent with the pH-driven ionization changes of the cationic and anionic headgroups described above. At pH 3 and pH 10.5, where the electrostatic attractions between the headgroups are expected to be weak, the orientationally disordered molecular tails pack into a hexagonal lattice.(61, 84, 99) At pH 6.5 and 9.5, the enhanced electrostatic interactions lead to a higher packing density, which necessarily requires orientational ordering of the backbone planes of the alkyl tails. Therefore, a distortion of the hexagonal lattice is expected and is manifested by assembly into 2D rectangular-C lattices. At pH 8.5, where the electrostatic attractions are expected to be close to a maximum, the lattice is rectangular-P with the highest packing density. As the cohesive interactions are maximized at this pH, the molecules must reorient to achieve denser packing.

The rectangular-P lattice of C_{16} mixtures indeed has a A_t ~ 0.188 nm^2, which is close to the minimum observed for herringbone packing of C_{16} alkyl tails in Langmuir films (A_t = 0.185 nm^2).(61) Here it is worth noting that the lattice parameters for the rectangular-P as well as the rectangular-C lattices deviate from the "universal curve" of lattice parameters for alkyl tail packing in Langmuir films by ~ 2-4%. (Figure 5.6) These deviations likely result from the strong electrostatic attractions between the cationic and anionic headgroups present in our study, but absent in Langmuir film studies. Consistent with this interpretation, the lattice parameters for our hexagonal lattices (weak electrostatic interactions) fall within the range of values for the hexagonally packed alkyl tails in Langmuir films.

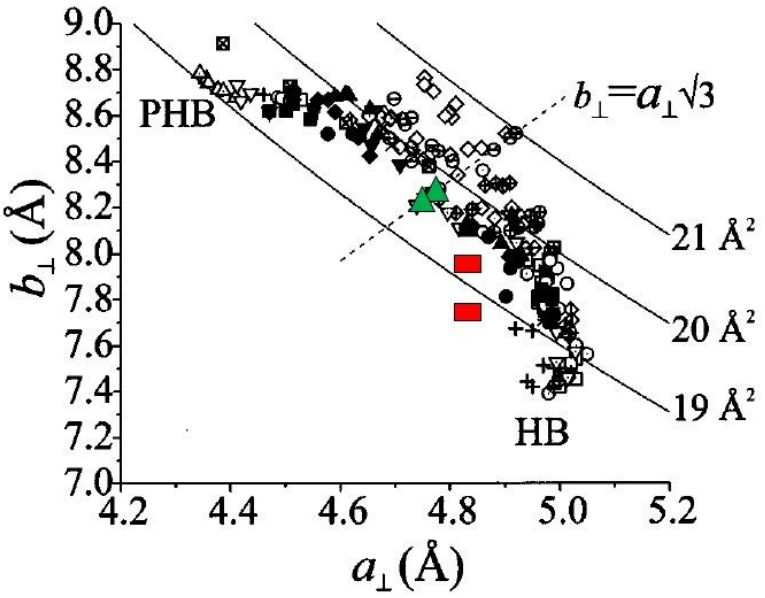

Figure 5.6. The universal curve of lattice parameters for alkyl tail packing in Langmuir films. (Image from Kaganer).(61) The green triangles and the red rectangles represent the lattice parameters of the hexagonal and rectangular lattices observed in the C_{16} mixture membranes.

In Chapter 4, no rectangular-P was observed for the mixture of *N*-palmitoyl trilysine and

palmitic acid at intermediate pH, where the electrostatic attractions should be highest. The larger trilysine headgroup may limit the extent of close intermolecular packing, as suggested by the larger area per tail (A_t~0.192 nm^2 at pH 8.5). These observations show that the solution pH provides a facile pathway to reversibly control the crystalline phases of ionic membranes by modulating the electrostatic interactions between oppositely charged amphiphilic headgroups.

Since biological media typically operate within a narrow pH range, it is valuable to understand the factors that control amphiphile crystallization at a particular pH. For this reason, we also explored the 2D packing of amphiphiles with longer or shorter tail lengths. The other systems we studied have the same cationic and anionic headgroups, but tail length C_{14}, C_{18}, C_{20} or C_{22}. The samples are prepared by mixing each cation with the carboxylic acid of the same alkyl tail length (Fig. 5.1b).

Fig. 5.7a shows the processed SAXS data for C_n (n = 14, 16, 18, 20, 22) mixtures in water at pH 3. In each system the cations alone formed micelles in solution (Fig. 5.8). Similar to the case of C_{16} mixtures of C_{14}, C_{18}, C_{20} and C_{22} each coassemble into bilayers that are stable over long periods (days). The SAXS data is fitted using a model that accounts for both bilayer membranes and spherical micelles (Fig. B.1). This model is chosen because SAXS profiles from solutions of the cations alone show strong scattering from micelle structures (Fig 5.8). As expected, the thickness of each membrane increases with alkyl tail length (Table 5.2). Fig. 5.5b shows the WAXS data for C_n (n = 14, 16, 18, 20 and 22) mixtures at pH 3. For the C_{14}, C_{16}, C_{18} and C_{20} mixtures, a single diffraction peak in the WAXS region indicates a hexagonal packing of the alkyl tails. In contrast, a rectangular-C phase is observed for C_{22} mixtures. The van der Waals interactions between the C_{22} tails are stronger than the shorter tails within the bilayers at a fixed temperature. Therefore, the longer tails are more sensitive to the orientation of neighboring tails,

resulting in the rectangular-C phase.

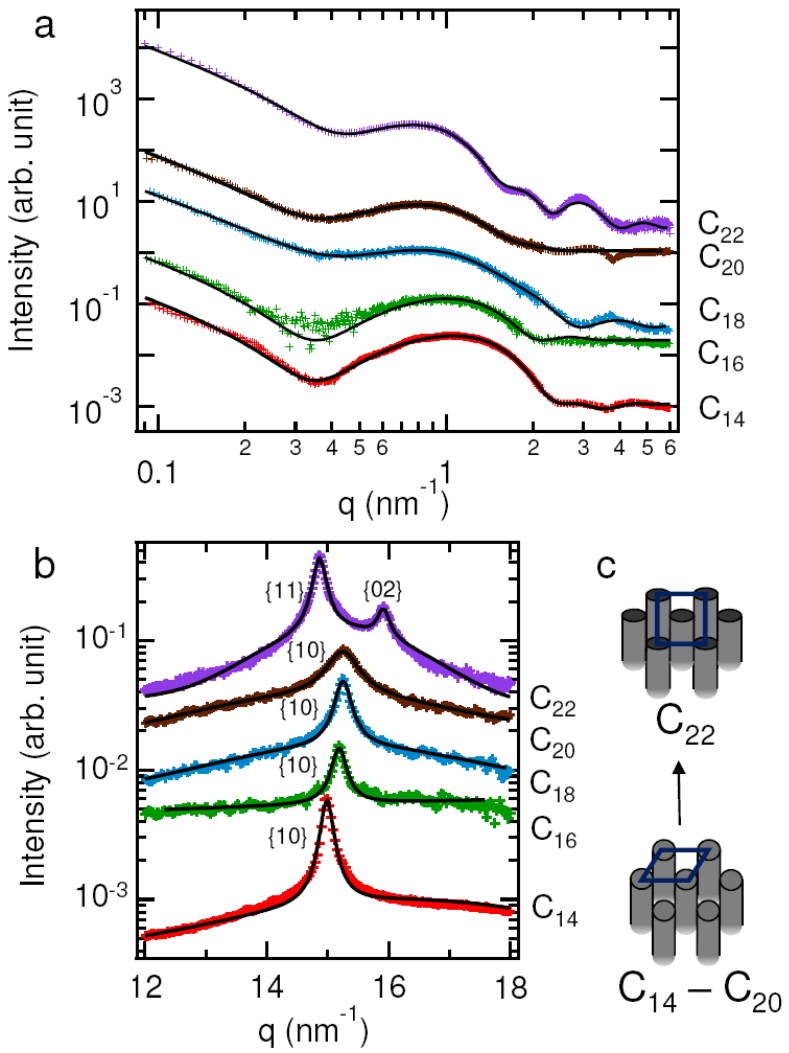

Figure 5.7. (a) *In situ* small- and (b) wide-angle x-ray scattering data showing the background subtracted scattered intensity versus the scattering vector q for mixtures of catanionic amphiphiles as the tail length n is increased from 14 to 22. The data sets are offset vertically for clarity. The black lines are the fits. (c) Schematic representations showing changes in molecular packing with tail length.

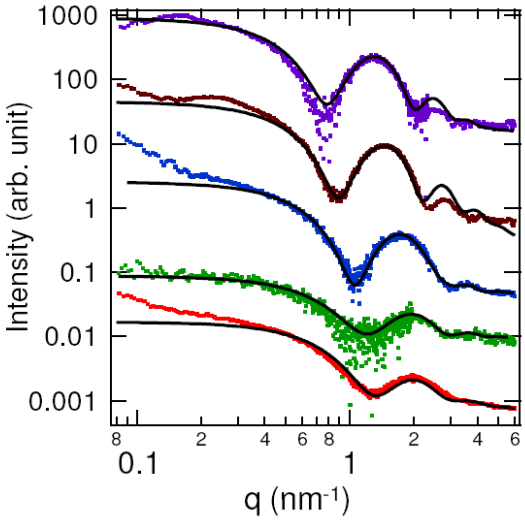

Figure 5.8. *In situ* small-angle x-ray scattering data showing the background subtracted scattered intensity versus the scattering vector q for C_{14}, C_{16}, C_{18}, C_{20} and C_{22} cation alone in aqueous solution at pH 3 (bottom to top). The curves are offset from each other for clarity. Black lines are fits of micelle structures with spherical core-shell model.

Table 5.2. Lattice parameters and membrane thicknesses obtained from x-ray scattering for mixtures of anion and cation at different tail lengths (*n)* at pH 3.

Tail length	**Crystal form**	**Domain size (nm)**	**Lattice const (nm)**	**Area per molecule (nm^2)**	**Area per molecule by MD (nm^2)**	**Membrane thickness (nm)**
14	Hexagonal	30	a = 0.487	0.205	0.207	5.6
16	Hexagonal	24	a = 0.477	0.197	0.200	5.8
18	Hexagonal	21	a = 0.477	0.197	/	7.5
20	Hexagonal	12	a = 0.477	0.197	/	7.6
22	Rectangular C	29	a = 0.500 b = 0.789	0.197	/	8.0

These results show how varying solution pH and tail length can affect the packing of molecules within a bilayer membrane. To fully understand the relationship between the hydrophobic tails and the charged headgroups, we also investigated membranes formed from this series of amphiphiles over a range of pH values. Fig. 5.9-5.12 show the SAXS and WAXS data respectively and Table 5.3-5.6 summarize the WAXS results. Based on the results, we are able to generate a 2D phase diagram as shown in Fig. 5.13. The shorter tailed surfactant C_{14} shows crystalline membranes with a hexagonal lattice across the pH range studied here. As discussed above, for C_{16} the change in electrostatic interaction between adjacent headgroups due to pH has a very strong effect on the crystalline order of the tails. The C_{18} mixture gives very similar phase transitions as a function of pH. As the tail length increases to C_{20}, there is a hexagonal to rectangular-C crystalline structure transition with increasing pH. The longest tail (C_{22}) is dominated by van der Waals interactions among the tails and shows only rectangular-C packing across all pH values. It is possible that the rectangular-P structure exists over a very narrow range of pH, as in the cases of C_{16} and C_{18} mixtures. This bilayer formed by coassembly of weak acids and weak bases has a strong capacity for self-buffering, making it experimentally difficult to attain precise pH values (±1 pH unit). Nevertheless, the pH-dependent changes in the A_t are similar to those observed in C_{16} and C_{18}, where A_t reaches a maximum around pH = 8.5 (Fig. 5.10). In summary, the packing of intermediate length tails (C_{16}, C_{18} and C_{20}) within the catanionic membrane is highly sensitive to the pH, whereas the packing of the shortest tail (C_{14}) and longest tail (C_{22}) is less sensitive.

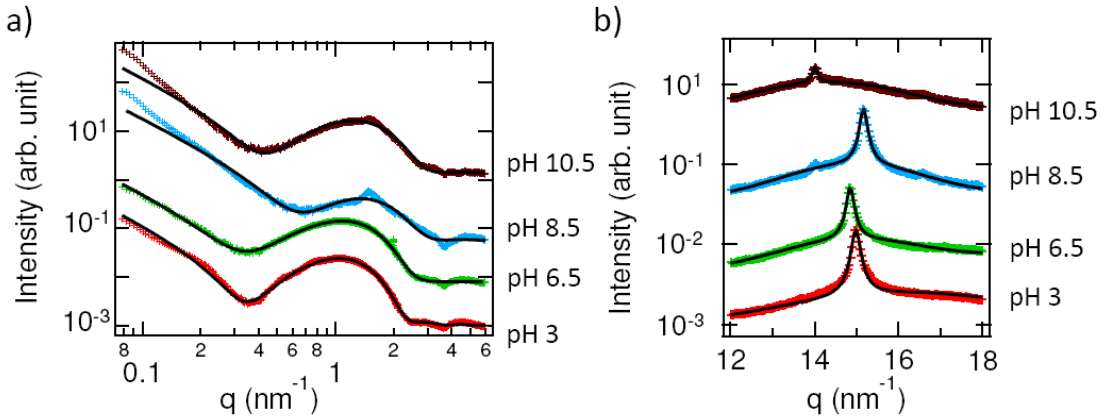

Figure 5.9. (a) *In situ* small- and (b) wide-angle x-ray scattering data showing the background subtracted scattered intensity versus the scattering vector q for mixtures of anion **C_{13}-COOH** and cation **C_{14}-K_2** as the pH is increased from 3 to 10.5. The data sets are offset vertically for clarity. The black lines are the fits. Deviations in the SAXS fits are due to sample polydispersity.

Table 5.3. Lattice parameters and membrane thicknesses obtained from x-ray scattering for mixtures of anion **C_{13}-COOH** and cation **C_{14}-K_2**.

pH	**lattice**	**Domain size (nm)**	**Lattice Const (nm)**	**Area per molecule (nm^2)**
3	Hexagonal	30	a = 0.487	0.205
6.5	Hexagonal	33	a = 0.487	0.205
8.5	Hexagonal	33	a = 0.477	0.197
10.5	Hexagonal/ rectangular -C	43	a = 0.518	0.232

Note: At pH 10.5, the principal peak is observed at q = 14 nm^{-1}. If this were the only diffraction peak, A_t would be unexpectedly large for an ordered packing of alkyl tails. Furthermore, for a hexagonal lattice the intensity of the diffraction peak is expected to increase with the domain size, which is the opposite our observation. Coincidentally, Langmuir films of fatty acids at high pH show a diffraction peak at q = 14 nm^{-1} accompanied by a weaker peak at 16 nm^{-1} (the so called X-phase). The structure in that case corresponds to a high aspect ratio rectangular-C phase. However, in the present case, the expected second peak does not show up in a statistically significant manner.

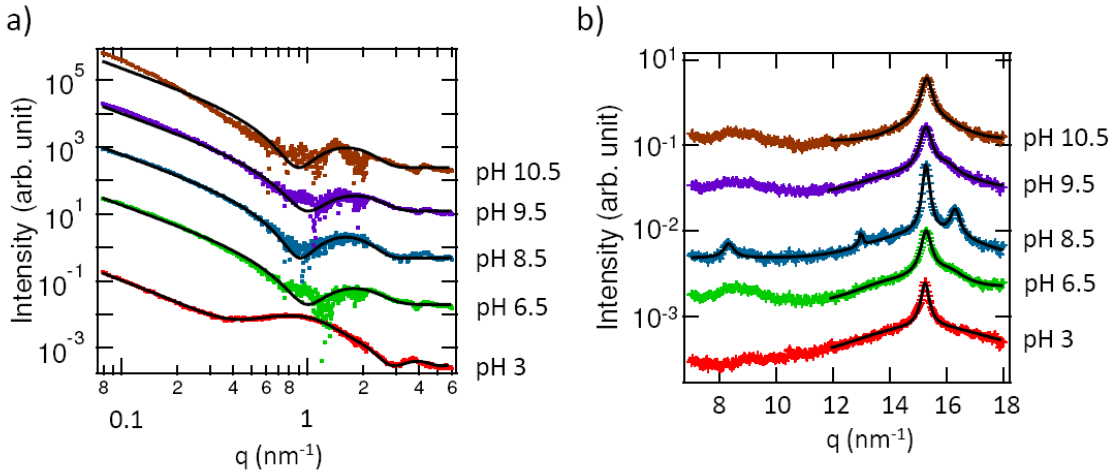

Figure 5.10. (a) *In situ* small- and (b) wide-angle x-ray scattering data showing the background subtracted scattered intensity versus the scattering vector q for mixtures of anion **C_{17}-COOH** and cation **C_{18}-K_2** as the pH is increased from 3 to 10.5. The data sets are offset vertically for clarity. The black lines are the fits. Deviations in the SAXS fits are due to sample polydispersity.

Table 5.4. Lattice parameters and membrane thicknesses obtained from x-ray scattering for mixtures of anion **C_{17}-COOH** and cation **C_{18}-K_2**.

pH	**lattice**	**Domain size (nm)**	**Lattice Const (nm)**	**Area per molecule (nm^2)**
3	Hexagonal	21	a = 0.477	0.197
6.5	Rectangular-C	11	a = 0.483	0.189
			b = 0.784	
8.5	Rectangular-P	23	a = 0.486	0.187
			b = 0.771	
9.5	Rectangular-C	12	a = 0.483	0.190
			b = 0.785	
10.5	Hexagonal	15	a = 0.474	0.195

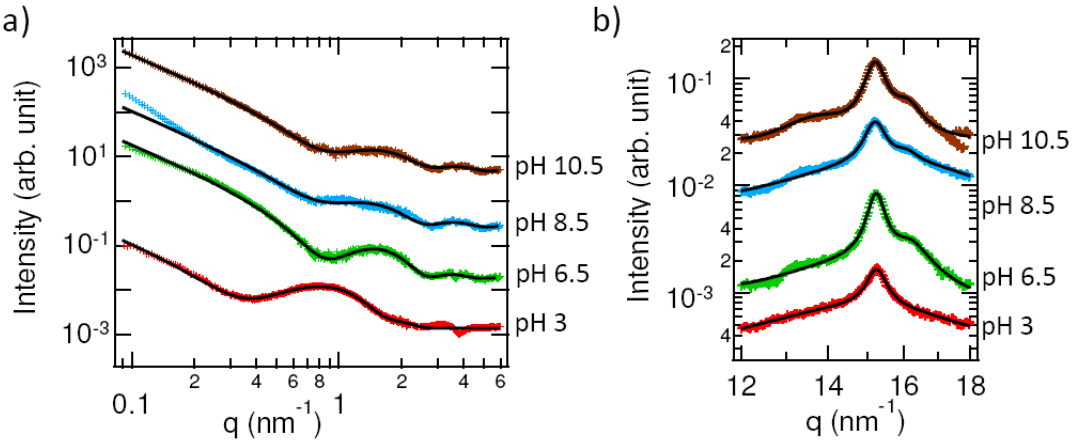

Figure 5.11. (a) *In situ* small- and (b) wide-angle x-ray scattering data showing the background subtracted scattered intensity versus the scattering vector q for mixtures of anion **C_{19}-COOH** and cation **C_{20}-K_2** as the pH is increased from 3 to 10.5. The data sets are offset vertically for clarity. The black lines are the fits. Deviations in the SAXS fits are due to sample polydispersity.

Table 5.5. Lattice parameters and membrane thicknesses obtained from x-ray scattering for mixtures of anion **C_{19}-COOH** and cation **C_{20}-K_2**.

pH	lattice	Domain size (nm)	Lattice Const (nm)	Area per molecule (nm^2)
3	Hexagonal	12	a = 0.477	0.197
6.5	Rectangular-C	8	a = 0.488 b = 0.776	0.189
8.5	Rectangular-C	9	a = 0.487 b = 0.781	0.190
10.5	Rectangular-C	8	a = 0.487 b = 0.781	0.190

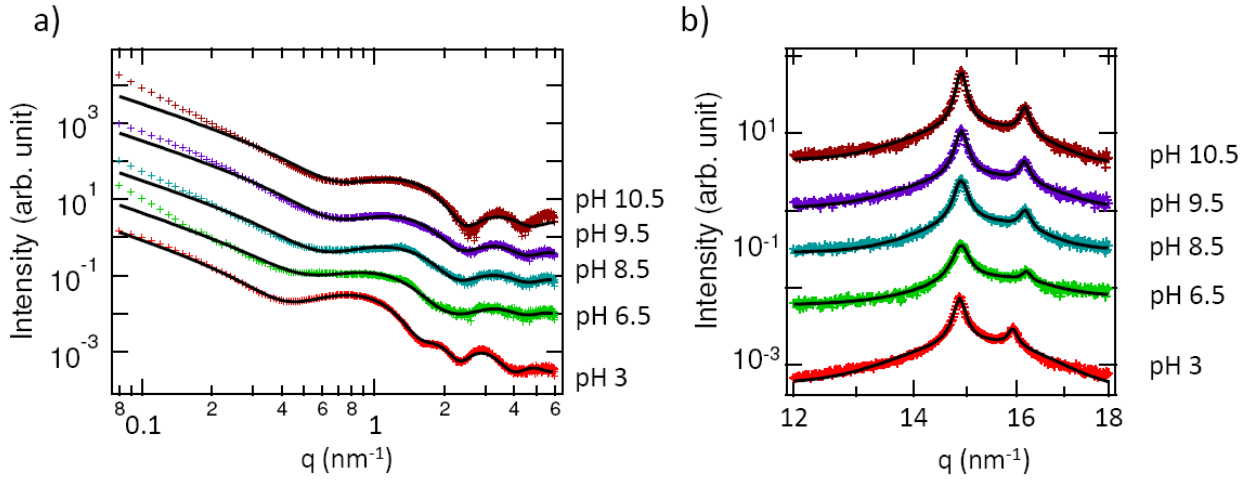

Figure 5.12. (a) *In situ* small- and (b) wide-angle x-ray scattering data showing the background subtracted scattered intensity versus the scattering vector *q* for mixtures of anion **C_{21}-COOH** and cation **C_{22}-K_2** as the pH is increased from 3 to 10.5. The data sets are offset vertically for clarity. The black lines are the fits. Deviations in the SAXS fits are due to sample polydispersity.

Table 5.6. Lattice parameters and membrane thicknesses obtained from x-ray scattering for mixtures of anion **C_{21}-COOH** and cation **C_{22}-K_2**.

pH	lattice	Domain size (nm)	Lattice Const (nm)	Area per molecule (nm^2)
3	Rectangular-C	28	a = 0.500 b = 0.789	0.197
6.5	Rectangular-C	26	a = 0.503 b = 0.776	0.195
8.5	Rectangular-C	24	a = 0.502 b = 0.777	0.195
9.5	Rectangular-C	26	a = 0.502 b = 0.778	0.195
10.5	Rectangular-C	30	a = 0.502 b = 0.778	0.195

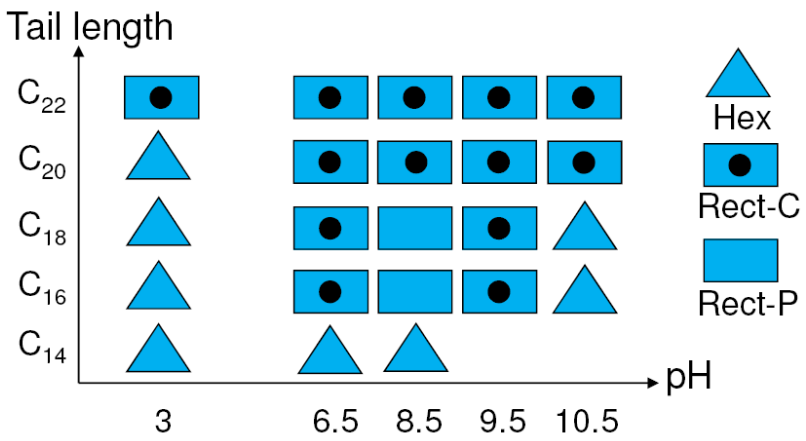

Figure 5.13. Phase diagram showing the formation of membrane and amphiphiles packing structure of catanionic mixture as a function of pH and tail length.

Atomistic MD simulations show remarkable agreement with the experiments in the C_{14} and C_{16} systems at pH 3 (Fig. 5.14a). The calculated peak positions extracted from the simulations match the experimental WAXS results. The simulation results show that the amphiphiles pack in hexagonal lattice in both cases, with a reduction in the area per molecule from 0.207 nm^2 (C_{14}) to 0.200 nm^2 (C_{16}). The simulations also reveal an enhancement in the van der Waals interactions from -27 k_BT to -33 k_BT per hydrocarbon tail when the tail length n increases from 14 to 16, which suggests a gain of approximately 2 k_BT per hydrocarbon atom in the crystalline membrane structure.(86) The hydration of lipid bilayers has been studied previously by MD simulations in systems with charged groups such as dimyristoylphosphatidylcholine (DMPC) lipid bilayers,(100) which showed that the average number of hydrogen bonds per lipid oxygen atom varies depending on its position within the lipid. Specifically, the oxygen atoms of the phosphate group in contact with water were found to have a higher probability to form hydrogen bonds

compared with the ester oxygen atoms. There are also studies on the structure of water close to hydroxyl groups.(101) However, the hydration of cationic-anionic bilayers is unknown. Our MD calculations of the radial distribution function show that the strength of the correlation (Fig. 5.14b) between the NH_3^+ headgroups (from cationic amphiphiles) and water is much stronger than between the COO^- headgroups (from anionic amphiphiles) and water since the NH_3^+ group from the long lysine side chain is more exposed to the aqueous medium. The coordination number of water molecules around the headgroups of NH_3^+, COO^- and COOH (from uncharged anionic amphiphiles) is smaller for C_{16} than for C_{14}, whereas the coordination number of COO^- around NH_3^+ is similar in both cases. The simulations suggest that the reduction of intermolecular spacing within the membrane from C_{14} to C_{16} is contributed by the enhancement of van der Waals interactions and the water distribution around the amphiphiles, while the electrostatic interaction between the oppositely charged headgroups remains the same in both cases. That is, the competition of van der Waals forces with electrostatic interactions between the cationic and anionic groups is not solely responsible for their coassembly into bilayers. In addition, the interaction of the polar heads of the amphiphiles with the water seems to play a key role in the energetics of coassembly.

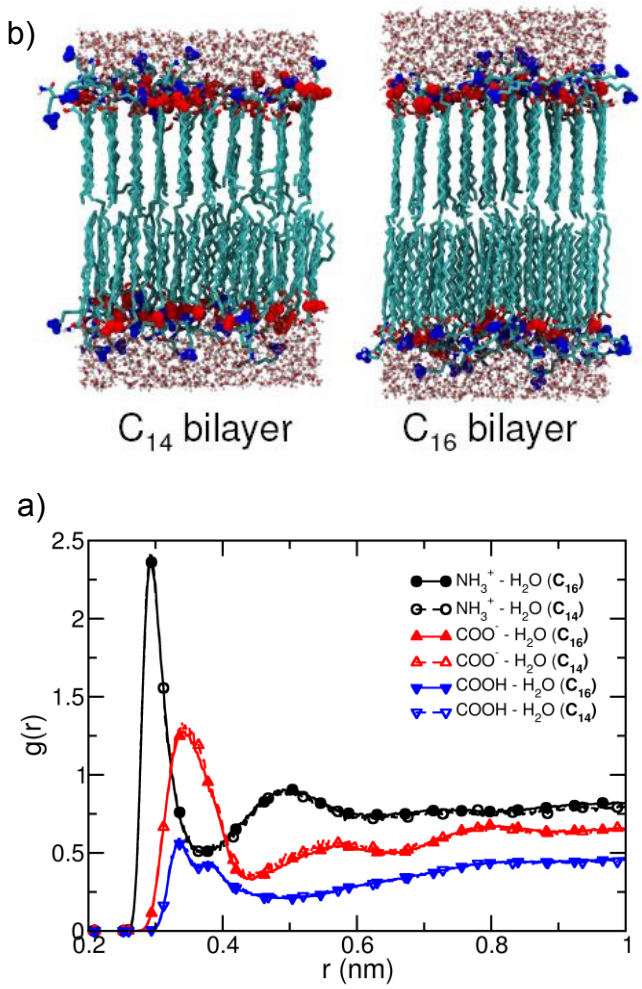

Figure 5.14. (a) Snapshots of the atomistic MD simulations on C_{14} and C_{16} systems. Carbon atoms are colored in cyan; the headgroups of the charged amphiphiles are highlighted: NH^{3+} in blue and COO^- in red. Water molecules are shown explicitly. (b) Radial distribution functions between water and the varying headgroups of NH_3^+ of $\mathbf{C_n\text{-}K_2}$, COO^- of $\mathbf{C_{n-1}COO^-}$, COOH of $\mathbf{C_{n-1}COOH}$, where n = 14, 16.

5.4. Summary

Our results demonstrate that crystalline order within catanionic membranes can be controlled by varying pH or molecular tail length. Previous work has shown only hexagonal packing of molecules within catanionic membranes where the ionization state of the cationic component does not depend on pH.(22, 102) In contrast, the ionization state of each of the molecules studied here is pH dependent, which enables us to control the membrane crystal structure by varying the degree of ionization among the headgroups. The solution pH controls the ionization state of the headgroups, thereby regulating the electrostatic interactions between neighboring molecules and the water around the headgroups. Increasing the alkyl tail length strengthen the van der Waals interactions between hydrophobic tails of adjacent molecules. These results produce a complete analysis of how the hydrophobic and hydrophilic parts of the molecules interact and contribute to crystalline packing within bilayers at a constant temperature. Our work suggests design of bilayer membranes with specific crystalline arrangements at ambient temperature and physiologically relevant pH environments with suitable choice of headgroup and tail. We foresee that the ability to control intermolecular spacing and arrangements may enable control over the encapsulation and release of molecules within the membrane. Changes in crystallinity are also likely to affect rate of diffusion of molecules across the membrane,(79-81) which is important for a liposome-based drug delivery system. Moreover, pH-induced crystalline transformations are likely used by organisms, including archaea and bacteria, to control metabolic flow in harsh environments.

Chapter 6. Long-range Crystallization of Highly Charged Self-assembled Nanofibers

6.1. Introduction

Networks of one-dimensional cytoskeletal components such as actin and microtubules are essential to mediate important biological processes like cell division, protein transport, and signaling.(31, 32) Self-assembled nanofibers(103) have also attracted attention for their ability to mimic the extracellular matrix and promote tissue regeneration. Recently, a pathway was discovered to create monodomain hydrogels of highly aligned peptide amphiphile nanofibers that can align cells and could potentially introduce anisotropic mechanical properties.(104) Furthermore, it may be possible to use aligned 1D nanostructures as templates for inorganic semiconductor materials as pathways to move charge carriers in transistors or photovoltaic devices.(105) Advancing these important applications will require a deeper understanding of the fundamental mechanisms and pathways to orient 1D objects.(106)

It is known from biological(107, 108) and synthetic (109) systems that like-charged nanofibers can form crystalline bundles with spacings on the order of their diameter. Counter intuitively, the crystallization of these structures into bundles is driven by fluctuation-induced attractive interactions between neighboring nanofibers.(110, 111) Added salts can also induce crystallization by bridging adjacent fibers through exponentially decaying attractive forces.(108, 112) In contrast to the filament bundling driven by attractive forces, a recent study of peptide amphiphile nanofibers at *ca*. 20 mM concentration showed the formation of a fibrillar network driven by *repulsions* between the negatively charged fibers using small-angle X-ray scattering (SAXS).(113) Interestingly, X-ray irradiation was found to create additional charges on the

surface of these fibers, causing bundle formation at even lower concentrations (*ca*. 5–10 mM). It was proposed that the long nanofibers formed at the early stages of self-assembly create a stable network that templates the elongation of short nanofibers within the growing bundle. The repulsion between these highly charged nanofibers is balanced by spatial confinement imposed by neighboring bundles within the network. (Fig. 6.1)

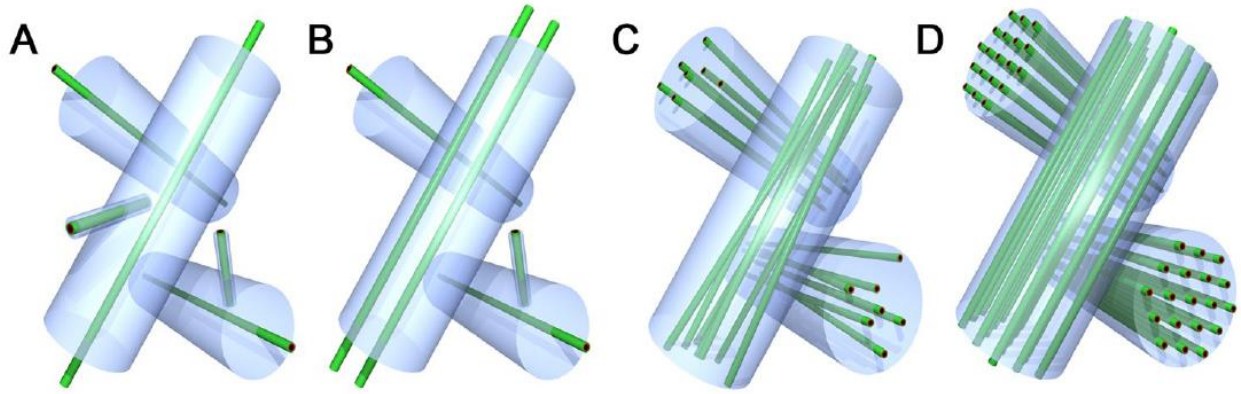

Figure 6.1. (A to D) Schematic illustration of the proposed templating model for filament bundle formation during self-assembly. (Image from Cui *et al*)(113)

Inspired by the anisotropic hexagonal packing of nanostructures observed for peptide amphiphile nanofibers, we designed amphiphilic molecules with a permanent charge (non-ionizable) in the headgroup based on aromatic groups in place of the hydrogen-bonding peptides. In water these molecules self-assemble into one-dimensional nanofibers that are expected to have a very high surface charge density. It has been argued that if the fibers form networks, the strong electrostatic repulsion between the confined fibers leads to highly spaced fibers arranged in two-dimensional hexagonal crystal.(113, 114) We investigate the ability of these fibers to form networks driven by electrostatic repulsion at low concentration (*ca*. 2–16

mM). These networks are studied by solution SAXS as a function of concentration and temperature.

6.2. Materials and Methods

6.2.1. Material Synthesis and Sample Preparation

General. Unless otherwise noted, all starting materials, reagents, and solvents were obtained from commercial suppliers and were used without further purification. Tetrahydrofuran (THF) and CH_2Cl_2 were dried using a VAC solvent purification system (Vacuum Atmospheres, Hawthorne, CA). 4-(Dimethylamino)-pyridinium 4-toluenesulfonate (DPTS) was prepared by forming the salt of 4-dimethylaminopyridine (DMAP) and *p*-toluenesulfonic acid in THF. Reactions were performed under nitrogen. Analytical thin layer chromatography (TLC) was performed on glass silica gel plates; visualization of products was performed with a handheld UV lamp. Flash column chromatography was performed using silica gel (ICN Silitech 32-63 D, 60 Å). The ^{1}H and ^{13}C NMR spectra were recorded on a Varian Inova 500, Inova 400, or Mercury 400 spectrometer using the residual solvent proton signal for calibration. Electrospray mass spectra were obtained on an Agilent 1100 MSD. Variable-temperature ^{1}H NMR experiments were performed on a Varian Inova 500 at 16 mM in D_2O at equilibrated for 10 minutes at each temperature. Variable temperature UV-vis experiments were performed on a HP 8452A diode array spectrophotometer with an Agilent 89090A temperature controller using a 0.01 mm path length cuvette.

Synthesis. The synthesis of azobenzene cation **1** is shown in Figure 6.2. Direction alkylation of acid **2** resulted in a mixture of the desired ether (**5**) and the corresponding decyl ester. Therefore, the acid was first protected as a methyl ester (**3**). The samples were kept dark to minimize

isomerization to the cis-azobenzene. If the cis-isomer was observed in solution, any of the molecules could be gently heated in solution to ~40°C for a few minutes to give exclusively the trans-azobenzene by ^{1}H NMR.

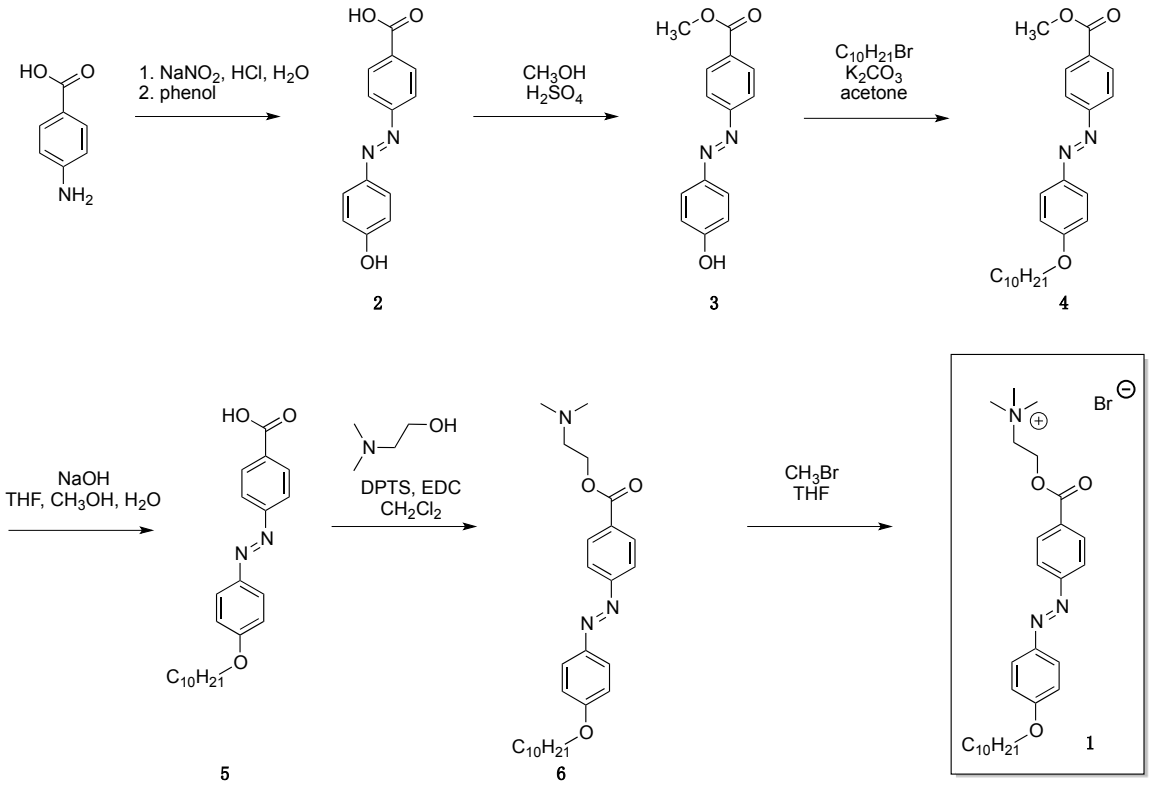

Figure 6.2. The scheme for the synthesis of cation **1**.

4'-hydroxy-4-azobenzylcarboxylic acid (2). A mixture of 4-aminobenzoic acid (1.790 g, 13.05 mmol) in aqueous HCl (20 mL, 3 M) was cooled with an ice bath. Sodium nitrite (1.09 g, 15.8 mmol) in 7.5 mL of H_2O was added drop wise and the mixture was allowed to stir for 30

min at 5°C. Solid phenol (1.509 g, 15.86 mmol) was added and the reaction continued to stir for 1 h at 5°C, neutralized with saturated aqueous $NaHCO_3$ (100 mL, saturated), and the crude product was filtered and washed with water. Purification via recrystallization from aqueous $NaHCO_3$ (100 mL) yielded the desired product as dark brown crystals (3.069 g, 12.66 mmol, 97%). ^{1}H NMR (500 MHz, DMSO, δ): 8.02 (d, *J* = 7.5 Hz, 2H), 7.78 (d, *J* = 8.5 Hz, 2H), 7.72 (d, *J* = 8 Hz, 2H), 6.96 (d, *J* = 8.5 Hz, 2H). ^{13}C NMR (500 MHz, DMSO, δ): 168.9, 162.3, 152.4, 144.7, 141.8, 129.9, 124.8, 121.0, 116.2. MS (m/z): $[M-H]^-$ calcd for $[C_{13}H_{10}N_2O_3]$, 241.06; found: 241.10.

Methyl 4'-hydroxy-4-azobenzylcarboxylate (3). Carboxylic acid **2** (0.937 g, 3.87 mmol) was suspended in CH_3OH (75 mL) in a round bottom flask at room temperature. To this mixture was added H_2SO_4 (0.5 mL, 9.38 mmol). The reaction was refluxed for three days and monitored by TLC. The reaction mixture was concentrated by rotary evaporation, re-dissolved in CH_2Cl_2 (200 mL), and washed with water (2 × 150 mL) and brine (150 mL). Purification of organic phase via flash chromatography (silica gel, 0% to 2% CH_3OH in CH_2Cl_2) yielded the desired product as an orange powder (0.221 g, 0.866 mmol, 22%). R_f (1% CH_3OH in CH_2Cl_2) = 0.13. ^{1}H NMR (500 MHz, $CDCl_3$, δ): 8.08 (d, *J* = 8 Hz, 2H), 7.81 (d, *J* = 6 Hz, 2H), 7.80 (d, *J* = 4.5 Hz, 2H), 6.87 (d, *J* = 8.5 Hz, 2H), 3.88 (s, 3H). ^{13}C NMR (500 MHz, $CDCl_3$, δ): 167.1, 161.2, 155.6, 146.4, 130.9, 130.7, 125.6, 122.4, 116.0, 52.5. MS (m/z): $[M+H]^+$ calcd for $[C_{14}H_{12}N_2O_3]$, 257.09; found: 257.10.

Methyl 4'-decyloxy-4-azobenzylcarboxylate (4). Ester **3** (2.60 g, 10.2 mmol) dissolved in acetone in a round bottom flask. To this solution was added 1-bromodecane (2.20 mL, 10.6

mmol), K_2CO_3 (4.00 g, 30 mmol), and a trace amount of 18-crown-6. The reaction was refluxed for five days and monitored by TLC. The crude reaction mixture was vacuum filtered, and the resulting filtrate was concentrated *in vacuo* by rotary evaporation. Purification via column chromatography (silica gel, 1:1 hexane/CH_2Cl_2) and recrystallization from hot methanol gave the desired product as an orange powder (1.68 g, 4.2 mmol, 42%). ^{1}H NMR (500 MHz, $CDCl_3$, δ): 8.17 (d, *J* = 8.5, 2H), 7.94 (d, *J* = 8.5 Hz, 2H), 7.90 (d, *J* = 8.5 Hz, 2H), 7.01 (d, *J* = 9 Hz, 2H), 4.04 (t, *J* = 6.8 Hz, 2H), 3.95 (s, 1H), 1.82 (app qn, J = 7.5, 2H), 1.48 (app qn, *J* = 7.5 Hz, 2H), 1.40-1.27 (m, 12H), 0.89 (t, *J* = 7, 3H). ^{13}C NMR (500 MHz, $CDCl_3$, δ): 166.8, 162.5, 155.5, 146.9, 131.2, 130.7, 125.3, 122.5, 114.9, 68.6, 52.4, 32.0, 29.7, 29.5, 29.5, 29.3, 29.4, 26.1, 22.8, 14.3. MS (m/z): $[M+H]^+$ calcd for $[C_{24}H_{32}N_2O_3]$, 397.24; found: 397.30.

4'-decyloxy-4-azobenzylcarboxylic acid (5). Ester **4** (0.8194 g, 2.066 mmol) was dissolved in THF (50 mL). To this solution was added NaOH (0.5613 g, 14.03 mmol) dissolved in H_2O (5 mL) and CH_3OH (5 mL). The reaction mixture was stirred at room temperature for two days. The crude reaction mixture was acidified to pH 1 with 1 M HCl, diluted with diethyl ether (100 mL), and washed with HCl (2 × 150 mL, 1 M) and brine (1 × 150 mL). The organic phase was concentrated *in vacuo* by rotary evaporation to afford the desired product as an orange powder (0.3978 g, 1.033 mmol, 50%). ^{1}H NMR (500 MHz, $CDCl_3$, δ): 8.10 (d, *J* = 8.5 Hz, 2H), 7.85 (d, *J* = 8.5 Hz, 2H), 7.81 (d, *J* = 9 Hz, 2H), 6.94 (d, *J* = 8.5 Hz, 2H), 3.98 (t, *J* = 6.5 Hz, 2H), 1.75 (app qn, *J* = 7.5 Hz, 2H), 1.40 (app qn, *J* = 7.8 Hz, 2H), 1.32–1.14 (m, 12H), 0.80 (t, *J* = 6.8 Hz, 3H). ^{13}C NMR (500 MHz, $CDCl_3$, δ): 168.3, 162.4, 155.5, 146.8, 131.4, 130.9, 125.2, 122.3, 114.8, 68.5, 31.9, 29.6, 29.4, 29.4, 29.2, 29.1, 26.0, 22.7, 14.1. MS (m/z): $[M-H]^-$ calcd for $[C_{23}H_{30}N_2O_3]$, 381.22; found: 381.20.

(*N*,*N*-dimethylaminoethanol) 4'-decyloxy-4-azobenzylcarboxylate (6). Carboxylic acid 5 (0.2485 g, 0.6497 mmol), EDC (0.1310 g, 0.6831 mmol) and DPTS (0.1963 g, 0.668 mmol) were dissolved in CH_2Cl_2 (40 mL) at room temperature. *N,N*-dimethylethanolamine was then added via syringe (0.40 mL, 4.0 mmol) to the cloudy solution. The reaction slowly turned clear and was allowed to continue stirring overnight. The crude product was diluted with CH_2Cl_2 (60 mL) and washed with saturated aqueous $NaHCO_3$ (2 × 100 mL) and water (4 × 150 mL). The organic phase was dried over $MgSO_4$ and concentrated in vacuo by rotary evaporation. Purification via column chromatography (0% TEA and 5% CH_3OH in CH_2Cl_2 to 1% TEA and 5% CH_3OH in CH_2Cl_2) yielded the desired product as an orange powder (0.0913 g, 0.201 mmol, 31%). ^{1}H NMR (500 MHz, $CDCl_3$, δ): 8.17 (d, J = 8 Hz, 2H), 7.93 (d, J = 9 Hz, 2H), 7.89 (d, J = 8.5 Hz, 2H), 6.99 (d, J = 9.5 Hz, 2H), 4.47 (t, J = 5.8 Hz, 2H), 4.03 (t, J = 6.5 Hz, 2H), 2.78 (t, J = 5.5 Hz, 2H), 2.35 (s, 6H), 1.81 (app qn, J = 7.5 Hz, 2H), 1.47 (app qn, J = 7.5 Hz, 2H), 1.40–1.22 (m, 12H), 0.88 (t, J = 7 Hz, 3H). ^{13}C NMR (500 MHz, $CDCl_3$, δ): 166.3, 162.6, 155.7, 147.0, 131.3, 130.9, 125.5, 122.6, 115.0, 68.7, 64.4, 63.2, 57.9, 46.0, 32.1, 29.8, 29.6, 26.2, 25.6, 22.9, 14.3. $[M+H]^+$ calcd for $[C_{27}H_{39}N_3O_3]$, 454.31; found: 454.30.

(*N*,*N*,*N*-trimethylaminoethanol) 4'-decyloxy-4-azobenzylcarboxylate bromide (1). Ester 6 was dissolved in THF (10 mL) at room temperature. To this solution was slowly added CH_3Br in methyl *tert*-butyl ether (1.50 mL, 2 M, 3.0 mmol) via syringe. The reaction mixture slowly turned cloudy and allowed to stir for two days. The crude product was vacuum filtered, yielding the desired product as orange crystals (0.0258 g, 0.0470 mmol, 25%). ^{1}H NMR (400 MHz, DMSO, δ): 8.19 (d, J = 8 Hz, 2H), 7.96 (d, J = 8 Hz, 2H), 7.93 (d, J = 9 Hz, 2H), 7.15 (d, J = 9

Hz, 2H), 4.75 (app s, 2H), 4.09 (t, *J* = 6 Hz, 2H), 3.86 (app s, 2H), 3.23 (s, 9H), 1.75 (app qn, 2H), 1.42 (app qn, *J* = 6.5 Hz, 2H), 1.36-1.18 (m, 12H), 0.85 (t, *J* = 6.5 Hz, 3H). ^{13}C NMR (400 MHz, DMSO, δ): 165.3, 162.9, 155.5, 146.7, 131.3, 131.0, 125.8, 123.0, 115.8, 68.7, 64.6, 59.6, 55.5, 32.0, 29.6, 29.4, 29.2, 26.1, 22.8, 14.6. MS (m/z): $[M]^+$ calcd for $[C_{28}H_{42}N_3O_3]^+$, 468.32; found: 468.30.

Sample preparation. Cation **1** was first dissolved in MilliQ water at a concentration of 16 mM (typically 750 μL). The mixture was agitated and heated to 50 °C for 60 min and then cooled to room temperature. For *in-situ* X-ray scattering studies, each solution was then diluted to 8, 6, 4 or 2 mM with the temperature of the samples adjusted in the thermo flow-cell.

6.2.2. Methods

Cryogenic transmission electron microscopy (cryo-TEM) imaging techniques was used. The details are discussed in Chapter 3.2. SAXS experimental setup is discussed in Chapter 3.3.

6.3. Experimental Results and Discussion

The amphiphilic molecule studied here is based on an aromatic azobenzene group, with a hydrophobic tail of ten carbons, and a permanent +1 charged headgroup (Figure 6.3a-molecular structure). The synthesis of this molecule with a bromide counterion is described in detail in the supplemental information. In water, these molecules dissolve to form a viscous yellow solution. Cryogenic transmission electron microscopy (TEM) shows formation of high aspect ratio nanofibers in aqueous solution (Figure 6.3c). Despite the strong electrostatic repulsions between the charged headgroups, the self-assembled 1D nanostructure is likely stabilized by interactions, such as van der Waals and π-π stacking interactions. Azobenzene amphiphiles in their *trans* form

are known to self-assemble(115) and form liquid-crystalline phases (116) at higher concentration, suggesting that excluded volume interactions characteristic of liquid crystals may also promote anisotropic interactions within the dense nanofiber.

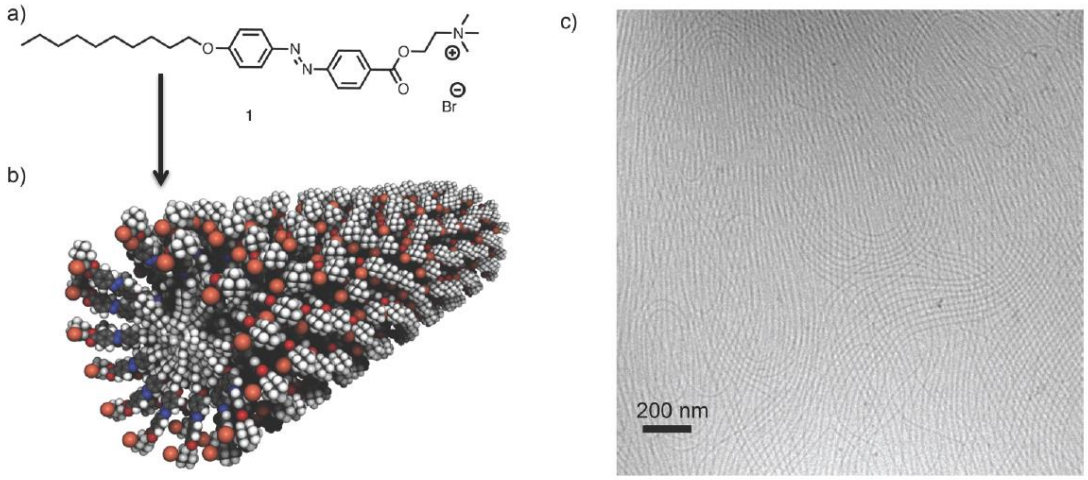

Figure 6.3. (a) Molecular structure of amphiphile **1** and (b) schematic of self-assembled nanofiber. (c) Representative cryogenic TEM images of nanofibers formed by self-assembly of cation **1** (1 mM in water).

Solution SAXS can provide information on the size and shape of a material (36) and is particularly useful to identify crystal structures over nanometer length scales. We used solution-phase SAXS to explore how these self-assembled nanoscale nanofibers ordered from 2–16 mM in water. The processed SAXS data are shown in Figure 6.4a as a function of the scattering vector $q = 4\pi\sin\theta/\lambda$. The scattered intensity $I(q)$ is given by

$$I(q) = F(q)S(q) \tag{6.1}$$

where $F(q)$ is the scattered intensity for an isolated object and $S(q)$ is the structure factor

corresponding to the correlation between objects. The fitted $F(q)$ and $S(q)$ curves for each data set are shown in the Figure 6.5. Fitting $F(q)$ to a cylindrical rod model, we estimate the nanofiber cross-sectional radius to be *ca*. 3.8 nm and the persistence length to be 10 nm. This radius is greater than the length of molecule **1** in its fully extended conformation estimated by molecular modeling (3.1 nm), suggesting that the molecules maybe slightly offset with respect to each other to reduce electrostatic repulsions. The persistence length of the nanofibers estimated from SAXS is much shorter than the total length shown by TEM and is consistent with the curvature of those fibers (Figure 6.3b). This fiber morphology appears be maintained across all of the conditions studied here.

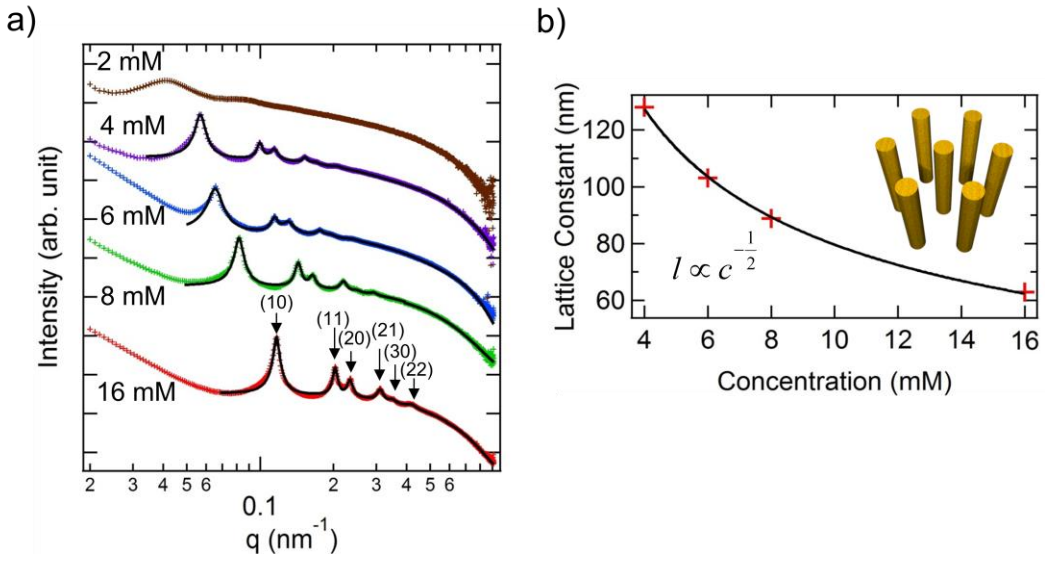

Figure 6.4. (a) *In situ* small-angle x-ray scattering (SAXS) data showing the background subtracted scattered intensity versus the scattering vector q (log-log plot) for amphiphile 1 in water as the solution is diluted from 16 mM to 2 mM. The data sets are offset vertically for clarity. The black lines are the fits. (b) The lattice constant of the hexagonal lattice formed by the nanofibers versus the solution concentration (log-log scale).

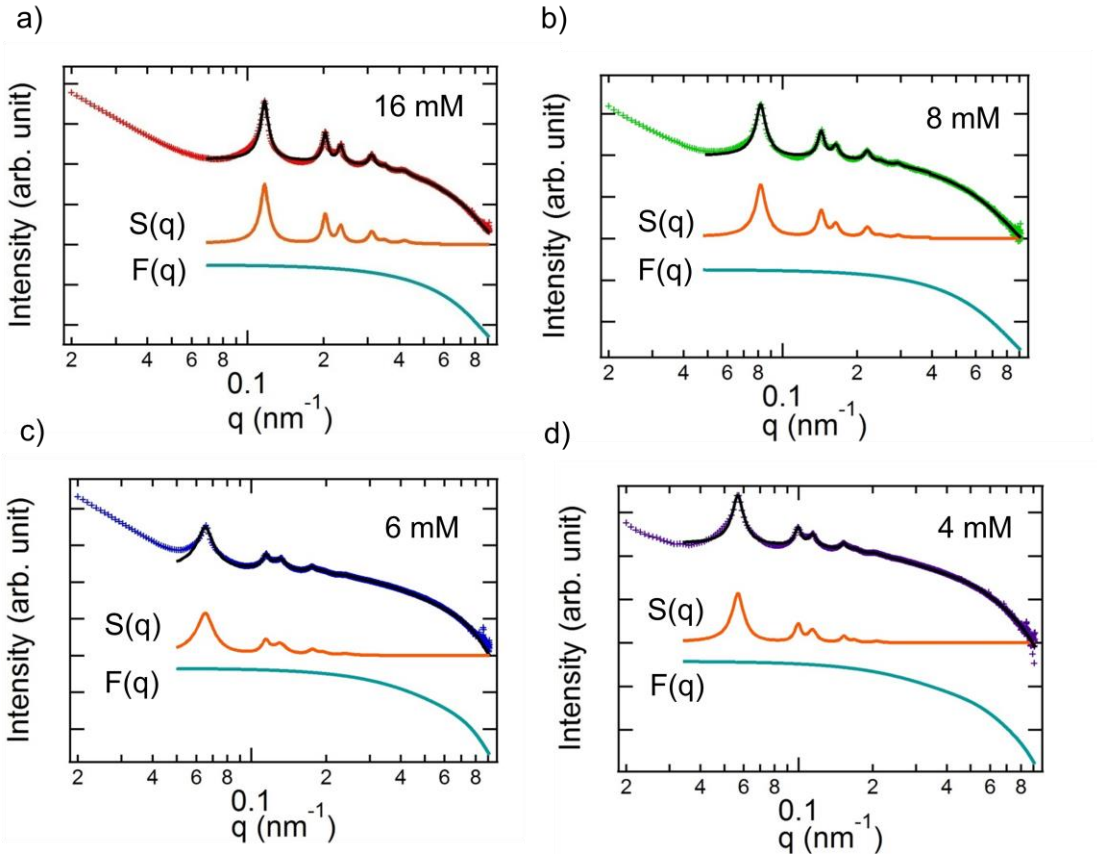

Figure 6.5. The fitted structure factor S(q) and form factor F(q) of the self-assembled nanofiber forming a hexagonal network at different concentration. Black lines are convolution of the structure factor and form factor, which match our observed SAXS data.

The structure factor $S(q)$ provides information about the packing structure of the nanofibers in solution. As shown in Figure 6.4, for 4–16 mM solutions we observe sharp diffraction peaks in the 0.1–0.5 nm^{-1} q-range indicating crystallization of the nanofibers. The relative positions of the peaks follow the q/q^* ratios of $1:\sqrt{3}:2:\sqrt{7}:3:\sqrt{12}$ (where q^* is the principal peak position) corresponding to 2D hexagonal lattice. The center-to-center spacing (lattice constant) between

the nanofibers is 63 nm for the 16 mM solution, which is about eight times larger than the filament diameter (~7.6 nm). The domain size of the 2D lattice can be estimated by the Scherrer equation to be on the order of 1 μm. To understand the origin of the nanofiber packing, we use the fitted dimensions and the electron density from SAXS to estimate a surface charge density *ca*. 0.4 C/m^2 (which corresponds to about +60e^-/nm). Charged filamentous viruses, like tobacco mosaic virus (TMV), are known to pack with liquid-like order in solution with a *d*-spacing on the order of 60 nm.(30) The magnitude of the surface charge density of TMV rods was reported to be 0.043 C/m^2,(117) which is much lower than the value we estimate for our nanofiber system. The condensation of bromide counterions may reduce this charge density,(118) but we expect the systems will remain highly charged. Addition of even 2 mM NaCl screens the repulsion and the hexagonal packing disappears (Figure 6.6). The high linear charge density contributes to strong repulsion among the nanofibers, enabling the formation of the observed hexagonally packed network with exceptionally large *d*-spacings.

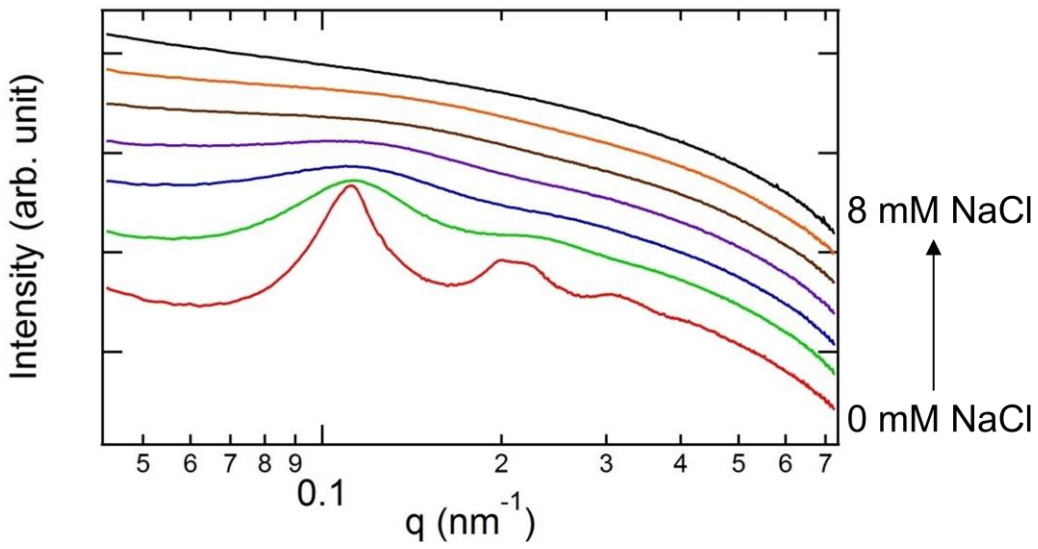

Figure 6.6. SAXS data showing the scattered intensity versus the scattering vector *q* for mixtures

of nanofiber formed by amphiphile **1** in NaCl solutions of 0, 1, 2, 3, 4, 5, 8 mM, from bottom to top. The data sets are offset vertically for clarity.

As we dilute the concentration of amphiphile **1** from 16 mM to 8, 6, or 4 mM, the lattice constant increases as $\sim c^{-1/2}$ (Figure 6.4b). The exponent *1/2* is expected for a hexagonal lattice of one-dimensional objects that is expanding in two dimensions. Our fit of $F(q)$ indicates that the filament structure does not change over this concentration range. The hexagonal packing disappears as the solution is further diluted to 2 mM. Instead, we observe only a broad intensity maximum in the SAXS data that indicates short-range correlations between adjacent nanofibers. The radial distribution function (RDF) $g(r)$ can be obtained by the Fourier-Bessel transform of the structure factor (119)

$$g(r) = 1 + \frac{1}{2\pi\rho}\int [S(q) - 1] J_0(qr) q dq \qquad (6.2)$$

where J_0 is the Bessel function of the first kind. The first maximum of the RDF for the 2 mM solution (Figure 6.7a) gives the nearest neighbor distance to be *ca.* 150 nm; the rapid decay of $g(r)$ indicates the loss of crystalline ordering. In contrast, for a more concentrated sample with long-range order, sharp peaks show up in the RDF (Figure 6.7c) and the amplitude of the peaks remains strong over many oscillations. These results indicate that above 2 mM the nanofibers are ordered in a crystalline lattice; at lower concentrations, only short-range correlations between the fibers are observed. The results of sample dilution show that it is possible to control the lattice constant by varying concentration.

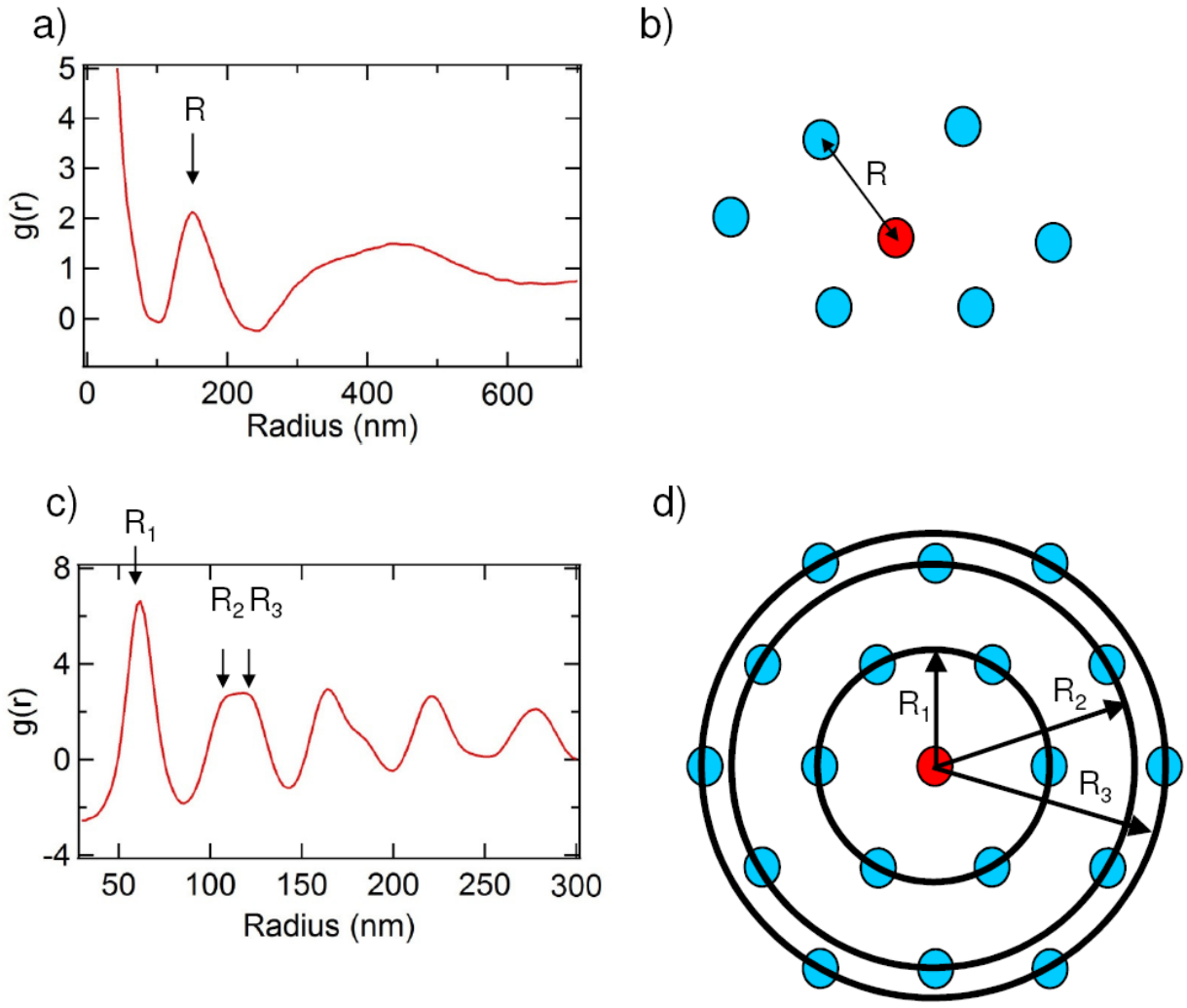

Figure 6.7. (a) The radial distribution function of 2 mM amphiphile **1** in water. The maximum corresponds to the correlation length between two nearest filaments in liquid order. (b) Schematic representation of the filaments not forming any crystal structure at 2 mM solution. (c) The radial distribution function of 16 mM amphiphile **1** in water. The maxima correspond to the correlation length between filaments packed in hexagonal structure. (d) Schematic representation of the filaments forming hexagonal crystal structure at 16 mM solution.

We examined the solutions as a function of temperature to understand the thermal stability of the system. Changes in the packing behavior were observed by heating a 16 mM solution from 20°C to 90°C (see Figure 6.8a). From 20°C to 40°C, the hexagonal peak positions remain constant and the lattice parameter is unchanged. When the temperature is increased to 50°C, the hexagonal pattern is replaced by a broad peak corresponding to liquid ordering between the nanofibers. As we heat the solution further, this correlation peak position shifts to higher q, which indicates a reduction in the average spacing between the nanofibers. For samples heated up to 70°C, the change is reversible and the hexagonal packing is restored upon cooling. In contrast, if these nanofiber solutions are heated to 80°C or higher they maintain their liquid-like order upon cooling, indicating an irreversible change in the network structure. While the hexagonal packing can be observed up to 40°C, the network is actually stable up to 70°C and can re-form the hexagonal crystal packing with the same spacing upon cooling.

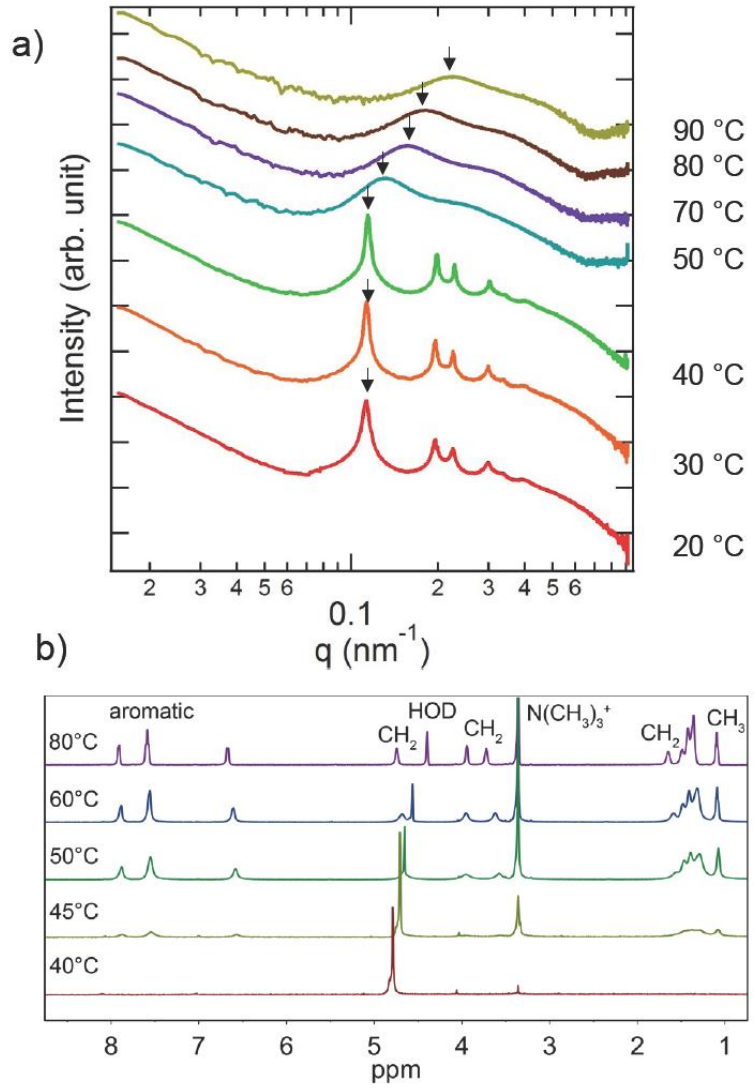

Figure 6.8. (a) SAXS data showing the background subtracted scattered intensity versus the scattering vector *q* (log-log plot) for amphiphile 1 in water as the solution temperature changes from 20°C to 90°C. The data sets are offset vertically for clarity. (b) Variable temperature ^{1}H NMR of 16 mM amphiphile 1 in D_2O shows transition at 50°C.

In order to better understand the behavior of the aggregate at the molecular level, we conducted variable-temperature ^{1}H NMR spectroscopy of amphiphile **1** in D_2O (Figure 6.8b).

The spectrum remains highly broadened up to 40°C, as expected for a highly aggregated system. From 50°C to 90°C, the proton resonances become sharper and more intense, suggesting that the molecules have more degrees of freedom within nanofiber. A similar transition temperature is observed by variable-temperature absorbance spectroscopy (Figure 6.9). At higher temperatures, the lower packing density of the molecules results in a decrease of the filament line charge density. Therefore, the repulsion between the filaments in the network is weakened and the nanofibers can come closer as suggested by the SAXS data.

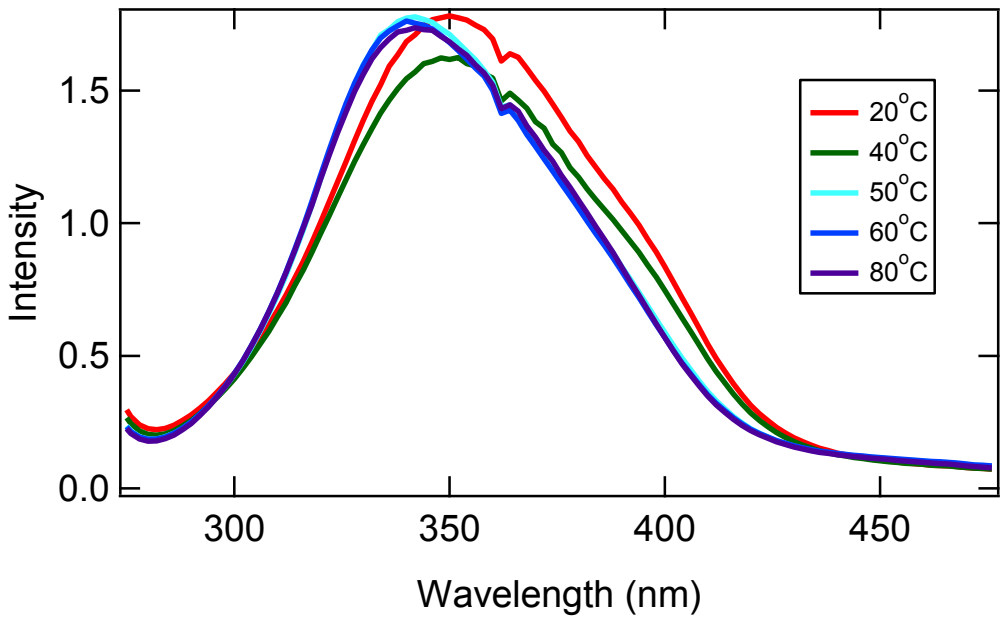

Figure 6.9. Variable-temperature absorbance spectra of amphiphile **1** in water at 16 mM showing a blue shift at 50°C. The absorbance peak at 352 nm is consistent with a π-π* transition reported previously for a *trans*-azobenzene with a similar electronic configuration. This blue shift may indicate that the molecules at room temperature are frozen in a state with little π-π stacking; heating provides the molecules more flexibility and more π-π stacking is observed. Data are not

normalized. The discontinuity at 362 nm is due to the lamp crossover.

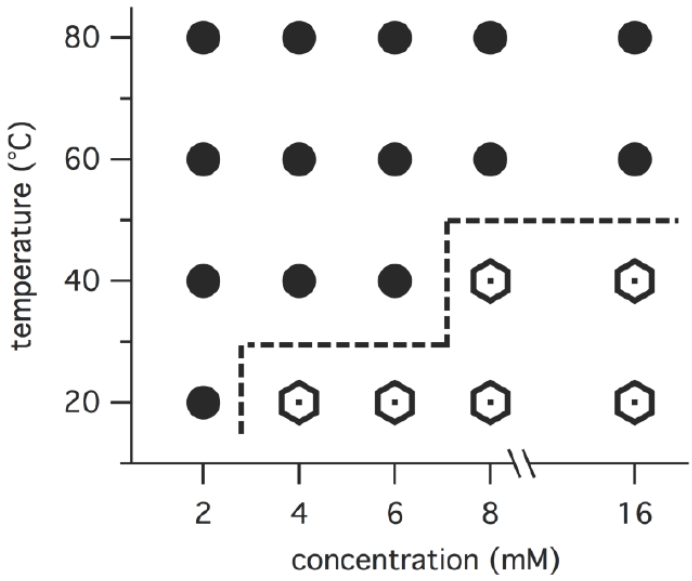

Figure 6.10. Diagram showing the packing structure of nanofibers formed by amphiphile **1** as a function of temperature and concentration.

The effects of solution concentration and temperature are summarized in Figure 6.10. When the solution concentration is greater than 4 mM and the temperature of the system is below the transition temperature of 50°C observed by ^{1}H NMR and UV-vis, the highly charged nanofibers organize into a hexagonal network. In this region, the nearest-neighbor distance of these nanofibers increases as the solution is diluted. When the solution is heated above the melting temperature or diluted to 2 mM, only short-range correlations are observed between nanofibers. At the intermediate concentration of 4 to 6 mM, the transition to the liquid phase occurs between 20 and 40°C (see Figure 6.10). Since this transition temperature is below the melting temperature

of molecule **1**, the collapse of the hexagonal packing is due to dilution of the nanofibers rather than changes on the molecular level within the nanofibers. At this diluted concentration the electrostatic repulsion between the charged fibers is barely sufficient to maintain the crystal structure within the confinement volume. Therefore, fluctuations of the fibers at slightly higher temperature make the crystal unstable. At high concentration, the loss of crystalline ordering upon heating is connected to decreasing linear charge density caused by melting of the molecules within the nanofiber; whereas at lower concentrations the transition to a liquid phase is due to fluctuations of the nanofibers with increasing temperature.

6.4. Summary

We have shown crystallization of highly charged cationic nanofibers into a hexagonally packed network with inter-fiber spacings more than eight times the fiber diameter. The high charge density required for this packing distance is made possible by close association of molecules within the nanofiber and the permanent +1 charge on each amphiphile. The strong electrostatic repulsions between molecules in the fibers can be counterbalanced by the intermolecular attractions among the azobenzene groups and between the hydrophobic tails, resulting in self-assembly into nanofibers. The packing structure and distance between the nanofibers can be controlled by either temperature or concentration. The dimensions of such a network could allow the templated growth of hybrid organic-inorganic materials on the appropriate length scale for energy applications. (120, 121)

Chapter 7. Summary and Outlook

7.1. Summary

In this thesis, we have designed systems of cationic and anionic peptide-based amphiphiles that can co-assemble into crystallized membranes and facetted vesicles in water. These closed shell vesicles mimic the polyhedral shapes that are observed in viral capsids, halophilic organism envelopes, and bacterial microcompartments. In many cases, electrostatic interactions between the membrane components are the key for crystallization of the membrane, which eventually result in a buckled structure. For example, the halophilic archaeon *Haloarcula japonica* has been found to undergo a triangular to spherical morphological change after lowering the magnesium concentration in the medium.(23, 43) The catanionic systems discussed in this thesis provide direct evidence that buckling is driven by electrostatic interactions between the oppositely charged headgroups.

We also explore the potential of these vesicles to be used for biomedical applications. We found that the intermolecular packing structure within the membrane can be controlled by varying the electrostatic interactions between the headgroups. In the +3/ -1 system, the ionization states of the *N*-palmitoyl trilysine **C_{16}-K_3** and palmitic acid **C_{15}-COOH** headgroups are pH sensitive. Through changing the pH in the catanionic solutions, we were able to observe hexagonal – rectangular C – hexagonal phase transition. Furthermore, closed shell vesicles are only observed when the amphiphiles are packed in hexagonal while the membranes exhibit in ribbon form when the molecules are packed in rectangular C. It shows that the membrane morphology is dependent on the molecular packing structure of amphiphiles. Therefore, pH can act as a switch to control the crystal structure and the mesoscale morphology of bilayers of

coassembled ionic amphiphiles. Since different parts of the human body such as stomach, small intestine and large intestine have different pH, the control of membrane morphology with pH has potential applications in medicine, such as targeted drug delivery.

In addition to using pH to adjust the headgroup attractions, in an analogous mixture of +2 and -1 amphiphiles, we adjust the tail length of the amphiphiles to control the van der Waals interactions between the hydrophobic tails. The crystalline order of the amphiphiles within the membrane does not change for the short tail system (C_{14}) and long tail system (C_{22}) at all measured pH values. For intermediate tail lengths (C_{16}-C_{20}), WAXS shows crystalline molecular ordering corresponding to hexagonal, rectangular-C, or rectangular-P phases depending on pH. These results produce a complete analysis of how the hydrophobic and hydrophilic parts of the molecules interact and contribute to crystalline packing within bilayers at a constant temperature. As a summary, we have demonstrated how to design cationic and anionic amphiphiles that coassemble into bilayer membranes with specific crystalline arrangements at specific temperature and physiologically relevant pH environments with suitable choice of headgroup and tail. The ability to adjust the molecular packing density within the membrane will be useful in drug delivery systems by controlling the molecular diffusion rate across the membranes.

Besides studying bilayers formed from catanionic mixtures, we also designed a system of cationic amphiphiles that self-assemble into nanofibers. These highly charged cationic nanofibers crystallize into a hexagonally packed network with inter-fiber spacings more than eight times the fiber diameter. The packing structure and distance between the nanofibers can be controlled by either temperature or concentration. The length scale of the ordering is appropriate for energy applications such as making organic-inorganic solar cells. To achieve such goal, we will need to improve the system by picking a choromophore that absorbs light better and increasing the

electron-hole transport efficiency. The system also needs to be salt stable.

7.2. Outlook

7.2.1. Vesicle Encapsulation Ability

In the study of +3 and -1 amphiphile mixtures, we propose the possibility to use these vesicles as drug carriers. It is important to study the drug release rate of the vesicles to understand the hydrophilic drug encapsulation ability of the vesicles. The stability of the vesicles upon dilution also needs to be considered. These factors can be tested by encapsulating a fluorescent dye calcein inside the vesicles during the assembly process. (122) After using size-exclusion column to remove the unbound dye, the calcein fluorescence can be measured as a function of time to estimate the hydrophilic molecule diffusion rate across the membrane walls of the vesicles at low and high pH. Further test can be performed at intermediate pH to understand the dye release process when the vesicles change the morphology and open up into ribbons. These results can provide us insight about the ability of these vesicles to carry hydrophilic molecules.

7.2.2. Control of Vesicle Shapes by Stoichiometry

The stoichiometric ratio of the cation and anion composing the vesicles is unknown in the systems of self-assembled vesicles discussed in Chapter 4 and 5, We were unable to know the charge distribution on the surface of the vesicles. As the electrostatic interactions between the amphiphiles have important effect in the membrane crystallization as well as the crystal phase, it will be important to design a system that we know the amount of cationic and anionic molecules with the membrane. (123)

Here, we propose a bilayer vesicle system by mixing positively charged and negatively

charged double tail phospholipids. The cation DMTAP has the chain melting temperature (T_m) 18.9°C while the anion DMPG has T_m = 23°C. These two molecules alone form spherical bilayer vesicles with liquid-like membranes at room temperature (25°C).(124, 125) By mixing these two molecules at different stoichiometric ratios, we may be able to form vesicles with different charge and may allow us to control the shapes. Specifically, with only the cationic component, the vesicles are expected to stay in spherical shape. With an increase in the anionic composition, the increasing electrostatic attractions between the oppositely charged molecules may induce crystallization of the phospholipid tails and result in buckling of the vesicles into nonspherical shapes. The vesicles are expected to adopt a spherical shape again with further increase in the anionic composition due to insufficient electrostatic attractions to bring the tails together. Therefore, in this system, we can adjust the stoichiometry and control the vesicle shapes. Furthermore, with the known ratio of cationic and anionic charges on the vesicles, it will be possible to model the electrostatic interactions between the molecules and provide more insights in how electrostatics induces tail crystallization.

REFERENCE

1. Trent A, Marullo R, Lin B, Black M, & Tirrell M (2011) Structural Properties of Soluble Peptide Amphiphile Micelles. *Soft Matter* 7(20):9572-9582.
2. Wang Y, Xu H, & Zhang X (2009) Tuning the Amphiphilicity of Building Blocks: Controlled Self-Assembly and Disassembly for Functional Supramolecular Materials. *Adv Mater* 21(28):2849-2864.
3. Ke DM, Zhan CL, Li ADQ, & Yao JN (2011) Morphological Transformation between Nanofibers and Vesicles in a Controllable Bipyridine-Tripeptide Self-Assembly. *Angew Chem Int Edit* 50(16):3715-3719.
4. Jung HT, Lee SY, Kaler EW, Coldren B, & Zasadzinski JA (2002) Gaussian Curvature and the Equilibrium among Bilayer Cylinders, Spheres, and Discs. *Proc Natl Acad Sci USA* 99(24):15318-15322.
5. Israelachvili J (1991) *Intermolecular & Surface Forces* (Academic Press, London).
6. Bramer T, Dew N, & Edsman K (2007) Pharmaceutical Applications for Catanionic Mixtures. *J Pharm Pharmacol* 59(10):1319-1334.
7. Torchilin VP (2005) Recent Advances with Liposomes as Pharmaceutical Carriers. *Nat Rev Drug Discov* 4(2):145-160.
8. Peer D, Karp JM, Hong S, FaroKHzad OC, Margalit R, & Langer R (2007) Nanocarriers as an Emerging Platform for Cancer Therapy. *Nat Nanotechnol* 2(12):751-760.
9. Ganta S, Devalapally H, Shahiwala A, & Amiji M (2008) A Review of Stimuli-responsive Nanocarriers for Drug and Gene Delivery. *J Control Release* 126(3):187-204.
10. Simmons BA, Li SC, John VT, McPherson GL, Bose A, Zhou WL, & He JB (2002) Morphology of CdS Nanocrystals Synthesized in a Mixed Surfactant System. *Nano Lett* 2(4):263-268.
11. McKelvey CA, Kaler EW, Zasadzinski JA, Coldren B, & Jung HT (2000) Templating Hollow Polymeric Spheres from Catanionic Equilibrium Vesicles: Synthesis and Characterization. *Langmuir* 16(22):8285-8290.
12. Collier JH & Messersmith PB (2001) Phospholipid Strategies in Biomineralization and Biomaterials Research. *Annu Rev Mater Res* 31:237-263.
13. Fenz SF & Sengupta K (2012) Giant Vesicles as Cell Models. *Integr Biol-Uk* 4(9):982-995.
14. Leermakers FAM & Scheutjens JMHM (1989) Statistical Thermodynamics of

Association Colloids .2. Lipid Vesicles. *J Phys Chem-Us* 93(21):7417-7426.

15. Chakrabarti P & Khorana HG (1975) New Approach to Study of Phospholipid-Protein Interactions in Biological-Membranes - Synthesis of Fatty-Acids and Phospholipids Containing Photosensitive Groups. *Biochemistry-Us* 14(23):5021-5033.
16. Fonseca P & Light A (1983) Incorporation of Bovine Enterokinase in Reconstituted Soybean Phospholipid-Vesicles. *J Biol Chem* 258(5):3069-3074.
17. Olson F, Hunt CA, Szoka FC, Vail WJ, & Papahadjopoulos D (1979) Preparation of Liposomes of Defined Size Distribution by Extrusion through Polycarbonate Membranes. *Biochim Biophys Acta* 557(1):9-23.
18. Kaler EW, Murthy AK, Rodriguez BE, & Zasadzinski JAN (1989) Spontaneous Vesicle Formation in Aqueous Mixtures of Single-Tailed Surfactants. *Science* 245(4924):1371-1374.
19. Morigaki K & Walde P (2007) Fatty Acid Vesicles. *Curr Opin Colloid In* 12(2):75-80.
20. Segota S & Tezak D (2006) Spontaneous Formation of Vesicles. *Adv Colloid Interfac* 121(1-3):51-75.
21. Dubois M, Deme B, Gulik-Krzywicki T, Dedieu JC, Vautrin C, Desert S, Perez E, & Zemb T (2001) Self-assembly of Regular Hollow Icosahedra in Salt-free Catanionic Solutions. *Nature* 411(6838):672-675.
22. Carriere D, Belloni L, Deme B, Dubois M, Vautrin C, Meister A, & Zemb T (2009) In-plane Distribution in Mixtures of Cationic and Anionic Surfactants. *Soft Matter* 5(24):4983-4990.
23. Nakamura S, Aono R, Mizutani S, Takashina T, Grant WD, & Horikoshi K (1992) The Cell-Surface Glycoprotein of Haloarcula-Japonica TR-1. *Biosci Biotech Bioch* 56(6):996-998.
24. Iancu CV, Morris DM, Dou ZC, Heinhorst S, Cannon GC, & Jensen GJ (2010) Organization, Structure, and Assembly of α-Carboxysomes Determined by Electron Cryotomography of Intact Cells. *J Mol Biol* 396(1):105-117.
25. Matson JB, Zha RH, & Stupp SI (2011) Peptide Self-assembly for Crafting Functional Biological Materials. *Curr Opin Solid St M* 15(6):225-235.
26. Cui HG, Webber MJ, & Stupp SI (2010) Self-Assembly of Peptide Amphiphiles: From Molecules to Nanostructures to Biomaterials. *Biopolymers* 94(1):1-18.
27. Zhang LG, Li N, Gao FM, Hou L, & Xu ZM (2012) Insulin Amyloid Fibrils: An Excellent Platform for Controlled Synthesis of Ultrathin Superlong Platinum Nanowires with High Electrocatalytic Activity. *J Am Chem Soc* 134(28):11326-11329.

28. Bisoyi HK & Kumar S (2011) Liquid-crystal Nanoscience: an Emerging Avenue of Soft Self-assembly. *Chem Soc Rev* 40(1):306-319.
29. Mao CB, Flynn CE, Hayhurst A, Sweeney R, Qi JF, Georgiou G, Iverson B, & Belcher AM (2003) Viral Assembly of Oriented Quantum Dot Nanowires. *Proc Natl Acad Sci USA* 100(12):6946-6951.
30. Maier E, Krause R, Deggelmann M, Hagenbuchle M, Weber R, & Fraden S (1992) Liquid-Like Order of Charged Rodlike Particle Solutions. *Macromolecules* 25(3):1125-1133.
31. Needleman DJ, Ojeda-Lopez MA, Raviv U, Miller HP, Wilson L, & Safinya CR (2004) Higher-order Assembly of Microtubules by Counterions: From Hexagonal Bundles to Living Necklaces. *Proc Natl Acad Sci USA* 101(46):16099-16103.
32. Wang N, Butler JP, & Ingber DE (1993) Mechanotransduction across the Cell Surface and through the Cytoskeleton. *Science* 260(5111):1124-1127.
33. Newcomb CJ, Moyer TJ, Lee SS, & Stupp SI (2012) Advances in Cryogenic Transmission Electron Microscopy for the Characterization of Dynamic Self-assembling Nanostructures. *Curr Opin Colloid In* 17(6):350-359.
34. Pederson AW, Ruberti JW, & Messersmith PB (2003) Thermal Assembly of a Biomimetic Mineral/Collagen Composite. *Biomaterials* 24(26):4881-4890.
35. Roe R-J (2000) *Methods of X-ray and Neutron Scattering in Polymer Science* (Oxford University Press, New York).
36. Svergun DI & Koch MHJ (2003) Small-Angle Scattering Studies of Biological Macromolecules in Solution. *Rep Prog Phys* 66(10):1735-1782.
37. Glatter O & Kratky O (1982) *Small Angle X-ray Scattering* (Academic Press Inc, New York).
38. Spector AA & Yorek MA (1985) Membrane Lipid-Composition and Cellular Function. *J Lipid Res* 26(9):1015-1035.
39. Seifert U (1997) Configurations of Fluid Membranes and Vesicles. *Adv Phys* 46(1):13-137.
40. Twarock R (2004) A Tiling Approach to Virus Capsid Assembly Explaining a Structural Puzzle in Virology. *J Theor Biol* 226(4):477-482.
41. Kerfeld CA, Sawaya MR, Tanaka S, Nguyen CV, Phillips M, Beeby M, & Yeates TO (2005) Protein Structures Forming the Shell of Primitive Bacterial Organelles. *Science* 309(5736):936-938.
42. Fan CG, Cheng SQ, Liu Y, Escobar CM, Crowley CS, Jefferson RE, Yeates TO, & Bobik

TA (2010) Short N-terminal Sequences Package Proteins into Bacterial Microcompartments. *Proc Natl Acad Sci USA* 107(16):7509-7514.

43. Walsby AE (1980) Square Bacterium. *Nature* 283(5742):69-71.
44. Vernizzi G, Sknepnek R, & Olvera de la Cruz M (2011) Platonic and Archimedean geometries in multicomponent elastic membranes. *Proc Natl Acad Sci USA* 108(11):4292-4296.
45. Geng Y, Dalhaimer P, Cai SS, Tsai R, Tewari M, Minko T, & Discher DE (2007) Shape Effects of Filaments Versus Spherical Particles in Flow and Drug Delivery. *Nat Nanotechnol* 2(4):249-255.
46. Soussan E, Cassel S, Blanzat M, & Rico-Lattes I (2009) Drug Delivery by Soft Matter: Matrix and Vesicular Carriers. *Angew Chem Int Edit* 48(2):274-288.
47. Dias RS, Lindman B, & Miguel MG (2002) DNA Interaction with Catanionic Vesicles. *J Phys Chem B* 106(48):12600-12607.
48. Liu YZ, Hu CH, Comotti A, & Ward MD (2011) Supramolecular Archimedean Cages Assembled with 72 Hydrogen Bonds. *Science* 333(6041):436-440.
49. Greenfield MA, Palmer LC, Vernizzi G, Olvera de la Cruz M, & Stupp SI (2009) Buckled Membranes in Mixed-Valence Ionic Amphiphile Vesicles. *J Am Chem Soc* 131(34):12030-12031.
50. Bressel K, Muthig M, Prevost S, Gummel J, Narayanan T, & Gradzielski M (2012) Shaping Vesicles-Controlling Size and Stability by Admixture of Amphiphilic Copolymer. *Acs Nano* 6(7):5858-5865.
51. Raspaud E, Olvera de la Cruz M, Sikorav JL, & Livolant F (1998) Precipitation of DNA by Polyamines: A Polyelectrolyte Behavior. *Biophys J* 74(1):381-393.
52. Wong GCL & Pollack L (2010) Electrostatics of Strongly Charged Biological Polymers: Ion-Mediated Interactions and Self-Organization in Nucleic Acids and Proteins. *Annu Rev Phys Chem* 61:171-189.
53. Kalsin AM, Fialkowski M, Paszewski M, Smoukov SK, Bishop KJM, & Grzybowski BA (2006) Electrostatic Self-assembly of Binary Nanoparticle Crystals with a Diamond-like Lattice. *Science* 312(5772):420-424.
54. Salkar RA, Mukesh D, Samant SD, & Manohar C (1998) Mechanism of Micelle to Vesicle Transition in Cationic-anionic Surfactant Mixtures. *Langmuir* 14(14):3778-3782.
55. Kaler EW, Herrington KL, Murthy AK, & Zasadzinski JAN (1992) Phase-Behavior and Structures of Mixtures of Anionic and Cationic Surfactants. *J Phys Chem-Us* 96(16):6698-6707.

56. Vernizzi G & Olvera de la Cruz M (2007) Faceting Ionic Shells into Icosahedra via Electrostatics. *Proc Natl Acad Sci USA* 104(47):18382-18386.
57. Schmid N, Eichenberger AP, Choutko A, Riniker S, Winger M, Mark AE, & van Gunsteren WF (2011) Definition and Testing of the GROMOS Force-field Versions 54A7 and 54B7. *Eur Biophys J Biophy* 40(7):843-856.
58. Monticelli L, Kandasamy SK, Periole X, Larson RG, Tieleman DP, & Marrink SJ (2008) The MARTINI Coarse-grained Force Field: Extension to Proteins. *J Chem Theory Comput* 4(5):819-834.
59. Marrink SJ, de Vries AH, & Mark AE (2004) Coarse Grained Model for Semiquantitative Lipid Simulations. *J Phys Chem B* 108(2):750-760.
60. Hartgerink JD, Beniash E, & Stupp SI (2001) Self-assembly and Mineralization of Peptide-amphiphile Nanofibers. *Science* 294(5547):1684-1688.
61. Kaganer VM, Mohwald H, & Dutta P (1999) Structure and Phase Transitions in Langmuir Monolayers. *Rev Mod Phys* 71(3):779-819.
62. Tagliazucchi M, Olvera de la Cruz M, & Szleifer I (2010) Self-Organization of Grafted Polyelectrolyte Layers via the Coupling of Chemical Equilibrium and Physical Interactions. *Proc Natl Acad Sci USA* 107(12):5300-5305.
63. Netz RR (2003) Charge Regulation of Weak Polyelectrolytes at Low- and High-dielectric-constant Substrates. *J Phys-Condens Mat* 15(1):S239-S244.
64. Solis FJ, Stupp SI, & Olvera de la Cruz M (2005) Charge Induced Pattern Formation on Surfaces: Segregation in Cylindrical Micelles of Cationic-anionic Peptide-amphiphiles. *J Chem Phys* 122(5).
65. Blaurock AE & Gamble RC (1979) Small Phosphatidylcholine Vesicles Appear to Be Faceted Below the Thermal Phase-Transition. *J Membrane Biol* 50(2):187-204.
66. Percec V, Wilson DA, Leowanawat P, Wilson CJ, Hughes AD, Kaucher MS, Hammer DA, Levine DH, Kim AJ, Bates FS*, et al.* (2010) Self-Assembly of Janus Dendrimers into Uniform Dendrimersomes and Other Complex Architectures. *Science* 328(5981):1009-1014.
67. Raspaud E, Pitard B, Durand D, Aguerre-Chariol O, Pelta J, Byk G, Scherman D, & Livolant F (2001) Polymorphism of DNA/Multi-cationic Lipid Complexes Driven by Temperature and Salts. *J Phys Chem B* 105(22):5291-5297.
68. Nadler M, Steiner A, Dvir T, Szekely O, Szekely P, Ginsburg A, Asor R, Resh R, Tamburu C, Peres M*, et al.* (2011) Following the Structural Changes during Zinc-induced Crystallization of Charged Membranes Using Time-resolved Solution X-ray Scattering.

Soft Matter 7(4):1512-1523.

69. Christian DA, Tian AW, Ellenbroek WG, Levental I, Rajagopal K, Janmey PA, Liu AJ, Baumgart T, & Discher DE (2009) Spotted Vesicles, Striped Micelles and Janus Assemblies Induced by Ligand Binding. *Nat Mater* 8(10):843-849.
70. Travesset A & Vaknin D (2006) Bjerrum Pairing Correlations at Charged Interfaces. *Europhys Lett* 74(1):181-187.
71. Horikoshi K, Aono R, & Nakamura S (1993) The Triangular Halophilic Archaebacterium Haloarcula-Japonica Strain TR-1. *Experientia* 49(6-7):497-502.
72. Leng J, Egelhaaf SU, & Cates ME (2003) Kinetics of the Micelle-to-vesicle Transition: Aqueous Lecithin-bile Salt Mixtures. *Biophys J* 85(3):1624-1646.
73. Leforestier A & Livolant F (2009) Structure of Toroidal DNA Collapsed inside the Phage Capsid. *Proc Natl Acad Sci USA* 106(23):9157-9162.
74. Poirier MG, Monhait T, & Marko JF (2002) Reversible Hypercondensation and Decondensation of Mitotic Chromosomes Studied Using Combined Chemical-micromechanical Techniques. *J Cell Biochem* 85(2):422-434.
75. Jancarik J & Kim SH (1991) Sparse-Matrix Sampling: A Screening Method for Crystallization of Proteins. *J Appl Crystallogr* 24:409-411.
76. Lee AG (2004) How Lipids Affect the Activities of Integral Membrane Proteins. *Bba-Biomembranes* 1666(1-2):62-87.
77. van Meer G, Voelker DR, & Feigenson GW (2008) Membrane Lipids: Where They Are and How They Behave. *Nat Rev Mol Cell Bio* 9(2):112-124.
78. Brugger B, Glass B, Haberkant P, Leibrecht I, Wieland FT, & Krausslich HG (2006) The HIV Lipidome: A Raft with an Unusual Composition. *Proc Natl Acad Sci USA* 103(8):2641-2646.
79. Falck E, Patra M, Karttunen M, Hyvonen MT, & Vattulainen I (2004) Lessons of Slicing Membranes: Interplay of Packing, Free Area, and Lateral Diffusion in Phospholipid/Cholesterol Bilayers. *Biophys J* 87(2):1076-1091.
80. Barenholz Y (2002) Cholesterol and other Membrane Active Sterols: from Membrane Evolution to "Rafts". *Prog Lipid Res* 41(1):1-5.
81. Nii T & Ishii F (2005) Encapsulation Efficiency of Water-soluble and Insoluble Drugs in Liposomes Prepared by the Microencapsulation Vesicle Method. *Int J Pharm* 298(1):198-205.
82. White SH & Wimley WC (1999) Membrane Protein Folding and Stability: Physical Principles. *Annu Rev Bioph Biom* 28:319-365.

83. Vernizzi G, Sknepnek R, & Olvera de la Cruz M (2011) Platonic and Archimedean Geometries in Multicomponent Elastic Membranes. *Proc Natl Acad Sci USA* 108(11):4292-4296.
84. Leung CY, Palmer LC, Qiao BF, Kewalramani S, Sknepnek R, Newcomb CJ, Greenfield MA, Vernizzi G, Stupp SI, Bedzyk MJ*, et al.* (2012) Molecular Crystallization Controlled by pH Regulates Mesoscopic Membrane Morphology. *ACS Nano* 6(12):10901-10909.
85. Sara M & Sleytr UB (2000) S-layer Proteins. *J Bacteriol* 182(4):859-868.
86. Qiao BF & Olvera de la Cruz M (2013) Driving Force for Crystallization of Anionic Lipid Membranes Revealed by Atomistic Simulations. *J Phys Chem B* 117(17):5073-5080.
87. Wang WJ, Park RY, Travesset A, & Vaknin D (2011) Ion-specific Induced Charges at Aqueous Soft Interfaces. *Phys Rev Lett* 106(5).
88. Isom DG, Castaneda CA, Cannon BR, & Garcia-Moreno BE (2011) Large Shifts in pK(a) Values of Lysine Residues Buried inside a Protein. *Proc Natl Acad Sci USA* 108(13):5260-5265.
89. Fukuda H, Kawata K, Okuda H, & Regen SL (1990) Bilayer-forming Ion-pair Amphiphiles from Single-chain Surfactants. *J Am Chem Soc* 112(4):1635-1637.
90. Rosa M, Infante MR, Miguel MD, & Lindman B (2006) Spontaneous Formation of Vesicles and Dispersed Cubic and Hexagonal Particles in Amino Acid-based Catanionic Surfactant Systems. *Langmuir* 22(13):5588-5596.
91. Marques EF, Regev O, Khan A, Miguel MD, & Lindman B (1998) Vesicle Formation and General Phase Behavior in the Catanionic Mixture SDS-DDAB-water. The Anionic-rich Side. *J Phys Chem B* 102(35):6746-6758.
92. Widom J & Baldwin RL (1983) Monomolecular Condensation of Lambda-DNA Induced by Cobalt Hexammine. *Biopolymers* 22(6):1595-1620.
93. Helmlinger G, Schell A, Dellian M, Forbes NS, & Jain RK (2002) Acid Production in Glycolysis-impaired Tumors Provides New Insights into Tumor Metabolism. *Clin Cancer Res* 8(4):1284-1291.
94. Tannock IF & Rotin D (1989) Acid pH in Tumors and its Potential for Therapeutic Exploitation. *Cancer Res* 49(16):4373-4384.
95. Wojtkowiak JW, Verduzco D, Schramm KJ, & Gillies RJ (2011) Drug Resistance and Cellular Adaptation to Tumor Acidic pH Microenvironment. *Mol Pharmaceut* 8(6):2032-2038.
96. Hess B, Kutzner C, van der Spoel D, & Lindahl E (2008) GROMACS 4: Algorithms for

Highly Efficient, Load-balanced, and Scalable Molecular Simulation. *J Chem Theory Comput* 4(3):435-447.

97. Essmann U, Perera L, Berkowitz ML, Darden T, Lee H, & Pedersen LG (1995) A Smooth Particle Mesh Ewald Method. *J Chem Phys* 103(19):8577-8593.
98. Thomas CK & Olvera de la Cruz M (2013) Theory and Simulations of Crystalline Control via Salinity and pH in Ionizable Membranes. *Soft Matter* 9(2):429-434.
99. Kuzmenko I, Kaganer VM, & Leiserowitz L (1998) Packing of Hydrocarbon Chains and Symmetry of Condensed Phases in Langmuir Monolayers. *Langmuir* 14(14):3882-3888.
100. Lopez CF, Nielsen SO, Klein ML, & Moore PB (2004) Hydrogen Bonding Structure and Dynamics of Water at the Dimyristoylphosphatidylcholine Lipid Bilayer Surface from a Molecular Dynamics Simulation. *J Phys Chem B* 108(21):6603-6610.
101. Janecek J & Netz RR (2007) Interfacial Water at Hydrophobic and Hydrophilic Surfaces: Depletion Versus Adsorption. *Langmuir* 23(16):8417-8429.
102. Vautrin C, Zemb T, Schneider M, & Tanaka M (2004) Balance of pH and Ionic Strength Influences on Chain Melting Transition in Catanionic Vesicles. *J Phys Chem B* 108(23):7986-7991.
103. Palmer LC & Stupp SI (2008) Molecular Self-Assembly into One-Dimensional Nanostructures. *Accounts Of Chemical Research* 41(12):1674-1684.
104. Zhang SM, Greenfield MA, Mata A, Palmer LC, Bitton R, Mantei JR, Aparicio C, Olvera de la Cruz M, & Stupp SI (2010) A Self-assembly Pathway to Aligned Monodomain Gels. *Nat Mater* 9(7):594-601.
105. Dang X, Yi H, Ham M-H, Qi J, Yun DS, Ladewski R, Strano MS, Hammond PT, & Belcher AM (2011) Virus-templated Self-assembled Single-walled Carbon Nanotubes for Highly Efficient Electron Collection in Photovoltaic Devices. *Nat Nanotechnol* 6(6):377-384.
106. Aida T, Meijer EW, & Stupp SI (2012) Functional Supramolecular Polymers. *Science* 335(6070):813-817.
107. Parsegian VA & Brenner SL (1976) The Role of Long Range Forces in Ordered Arrays of Tobacco Mosaic Virus. *Nature* 259:632-635.
108. Li T, Winans RE, & Lee B (2011) Superlattice of Rodlike Virus Particles Formed in Aqueous Solution through Like-Charge Attraction. *Langmuir* 27(17):10929-10937.
109. Valéry C, Paternostre M, Robert B, Gulik-Krzywicki T, Narayanan T, Dedieu J-C, Keller G, Torres M-L, Cherif-Cheikh R, Calvo P*, et al.* (2003) Biomimetic Organization: Octapeptide Self-assembly into Nanotubes of Viral Capsid-like Dimension. *Proc Natl*

Acad Sci USA 100(18):10258-10262.

110. Oosawa F (1968) Interaction between Parallel Rodlike Macroions. *Biopolymers* 6(11):1633-1647.
111. Safinya CR & Li Y (2010) Bundling with X-rays. *Science* 327(5965):529-530.
112. Solis FJ & Olvera de la Cruz M (1999) Attractive Interactions Between Rodlike Polyelectrolytes: Polarization, Crystallization, and Packing. *Physical Review E, Statistical physics, plasmas, fluids, and related interdisciplinary topics* 60(4 Pt B):4496-4499.
113. Cui H, Pashuck ET, Velichko YS, Weigand SJ, Cheetham AG, Newcomb CJ, & Stupp SI (2010) Spontaneous and X-ray-triggered Crystallization at Long Range in Self-assembling Filament Networks. *Science* 327(5965):555-559.
114. Yao ZW & Olvera de la Cruz M (2013) Electrostatic Repulsion-driven Crystallization Model Arising from Filament Networks. *Phys Rev E* 87(4).
115. Kunitake T, Okahata Y, Shimomura M, Yasunami S, & Takarabe K (1981) Formation of Stable Bilayer Assemblies in Water From Single-Chain Amphiphiles . Relationship Between the Amphiphile Structure and the Aggregate Morphology. *J Am Chem Soc* 103:5401-5413.
116. Ikeda T & Tsutsumi O (1995) Optical Switching and Image Storage by Means of Azobenzene Liquid-crystal Films. *Science* 268(5219):1873-1875.
117. Ermolina I, Morgan H, Green NG, Milner JJ, & Feldman Y (2003) Dielectric Spectroscopy of Tobacco Mosaic Virus. *Bba-Gen Subjects* 1622(1):57-63.
118. Gelbart W, Bruinsma R, Pincus P, & Parsegian V (2000) DNA-inspired Electrostatics. *Physics Today* 53(9):38-44.
119. Spaar A & Salditt T (2003) Short Range Order of Hydrocarbon Chains in Fluid Phospholipid Bilayers Studied by X-ray Diffraction from Highly Oriented Membranes. *Biophys J* 85(3):1576-1584.
120. Sofos M, Stone DA, Goswami DK, Okasinski JS, Jin H, Bedzyk MJ, & Stupp SI (2008) Nanoscale Structure of Self-assembling Hybrid Materials of Inorganic and Electronically Active Organic Phases. *The Journal of Physical Chemistry C* 112:2881-2887.
121. Briseno AL, Holcombe TW, Boukai AI, Garnett EC, Shelton SW, Fréchet JJM, & Yang P (2010) Oligo- and Polythiophene/ZnO Hybrid Nanowire Solar Cells. *Nano Lett* 10(1):334-340.
122. Wang X, Danoff EJ, Sinkov NA, Lee JH, Raghavan SR, & English DS (2006) Highly Efficient Capture and Long-term Encapsulation of Dye by Catanionic Surfactant Vesicles.

Langmuir 22(15):6461-6464.

123. Wadsater M, Maric S, Simonsen JB, Mortensen K, & Cardenas M (2013) The Effect of Using Binary Mixtures of Zwitterionic and Charged Lipids on Nanodisc Formation and Stability. *Soft Matter* 9(7):2329-2337.
124. Zantl R, Baicu L, Artzner F, Sprenger I, Rapp G, & Radler JO (1999) Thermotropic Phase Behavior of Cationic Lipid-DNA Complexes Compared to Binary Lipid Mixtures. *J Phys Chem B* 103(46):10300-10310.
125. Riske KA, Amaral LQ, Dobereiner HG, & Lamy MT (2004) Mesoscopic Structure in the Chain-melting Regime of Anionic Phospholipid Vesicles: DMPG. *Biophys J* 86(6):3722-3733.
126. Ilavsky J (2012) Nika: Software for Two-dimensional Data Reduction. *J Appl Crystallogr* 45:324-328.
127. Kline SR (2006) Reduction and Analysis of SANS and USANS Data Using IGOR Pro. *J Appl Crystallogr* 39:895-900.
128. Ben-Nun T, Ginsburg A, Szekely P, & Raviv U (2010) X Plus : a Comprehensive Computationally Accelerated Structure Analysis Tool for Solution X-ray Scattering from Supramolecular Self-assemblies. *J Appl Crystallogr* 43:1522-1531.
129. Bartlett P & Ottewill RH (1992) A Neutron-Scattering Study of the Structure of a Bimodal Colloidal Crystal. *J Chem Phys* 96(4):3306-3318.
130. Nallet F, Laversanne R, & Roux D (1993) Modeling X-Ray or Neutron-Scattering Spectra of Lyotropic Lamellar Phases - Interplay between Form and Structure Factors. *J Phys Ii* 3(4):487-502.

Appendix A. Vesicles Formed by Azobenzene Amphiphiles

In Chapter 4 and 5, we discussed the use of peptide amphiphiles with ionic headgroups and hydrocarbon alkyl tails to coassemble vesicles. In chapter 6, we used a cationic amphiphile with an azobenzene group to coassemble charged nanofibers. The aromatic azobenzene group strengthens the attractions between the molecules and stabilizes the self-assembly into highly charged nanofibers. In this Appendix, we present a system of facetted vesicles that is assembled from azobenzene amphiphiles by similar strategy. The cation used is exactly the same as the one presented in chapter 6. The structure of the anionic component is shown in Fig. A1.1. The cationic molecule has a +1 permanent charge on the head and the anion has a -1 charge group with pKa ~ 4. Two similar systems were studied, in one case the hydrophobic region of both molecules contains an alkyl tail with 8 carbons (C_8) and the other contains 10 carbons (C_{10}).

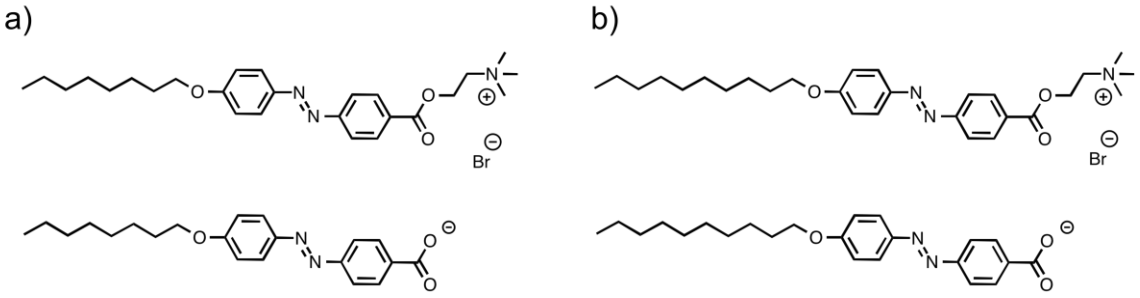

Figure A.1. (a) Molecular structure of cationic (top) and anionic (bottom) amphiphile with an azobenzene group and 8 carbons in the alkyl tails. (b) Molecular structure of cationic (top) and anionic (bottom) amphiphile with an azobenzene group and 10 carbons in the alkyl tails.

To make the vesicles, the cation was first dissolved in MilliQ water at a concentration of 4 mM (typically 750 µL). This solution was added to a centrifuge tube containing 1.2 equiv of the solid anion. The mixture was agitated and heated to 80 °C for 60 min. Each sample was cooled to room temperature then centrifuged at approximately 2000 rpm for 5 min to remove residual solids prior to analysis.

The QFDE-TEM image of the C_8 cation alone in water in Fig. A1.2a shows that they form fibers. When the cations and anions are mixed together and heated, they coassembled into bilayer vesicles with a buckled surface. The size of these vesicles is about 100-300nm in diameter as shown in Fig. A1.2b-c. Simultaneous SAXS and WAXS was used to understand if the facetted surface of the vesicles are crystallized and the results are shown in Fig. A1.3 as a function of scattering vector ($q=4\pi\sin\theta/\lambda$).

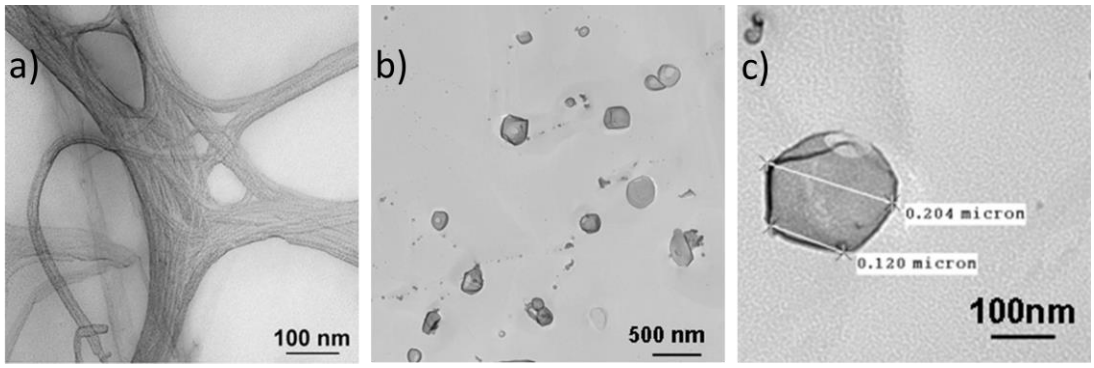

Figure A.2. Coassembly of oppositely charged amphiphiles shows vesicles in aqueous solution. Quick-freeze/deep-etch TEM images of (a) fibers formed from the cation alone (4 mM) and (b, c) faceted vesicles from a mixture of the cation and anion in water.

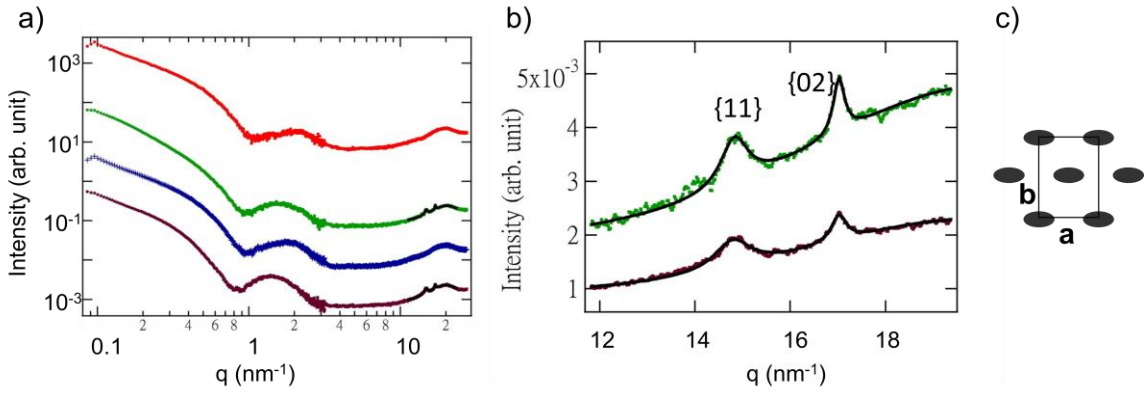

Figure A.3. (a) *In situ* small- and wide-angle x-ray scattering data showing the background subtracted scattered intensity versus the scattering vector q for cation alone (blue for C_{10} and red for C_8) and mixtures of cation and anion. (brown for C_{10} and green for C_8) The data sets are offset vertically for clarity. (b) WAXS data and peak fits of the mixed cation/anion samples mixed samples indicate formation of crystalline lattices. (b) Schematic of the rectangular-C unit cell of the catanionic mixture

Table A.1. Lattice parameters obtained from x-ray scattering for mixture of azobenzene cation and anion

	C_8 mixture		C_{10} mixture	
	Peak 1	Peak 2	Peak 1	Peak 2
q (nm^{-1})	14.8	17.0	14.8	17.0
Domain size (nm)	8	21	8	20
Lattice constants (nm)	a=0.519 b=0.739		a=0.519 b=0.739	
Area per molecule (nm^2)	0.192		0.192	

In the WAXS region, diffraction peaks show up in the scattering data of catanionic vesicles, which indicates the crystallization of the amphiphiles within the bilayer membrane. The appearance of two diffraction peaks indicates that the molecules are packed in a rectangular-C structure. The fitted parameters are shown in Table A1.1. The diffraction peak positions for both C_8 and C_{10} cation/anion mixture are the same. This is expected since the lattices formed are on a 2-D plane and the C_8 and C_{10} molecules are very similar to each other with slightly different tail lengths. The area per molecule calculated (A_t=0.192 nm^2) is very similar to the packing of alkyl tails discussed in chapter 4 and 5. The {02} peak is much sharper than the {11} suggesting the correlation in the **b** direction of the lattice is stronger than in the **a** direction. One possible explanation is that the direction of π-π stacking interactions of the molecules is in the **b** direction and therefore the molecules order better in the **b** direction than in the **a** direction.

As a summary, we have shown a different approach to assemble facetted vesicles. Even the amphiphilic headgroups have a weaker charge (+1 or -1); the packing can be stabilized by the π-π stacking interactions between the molecules. Since the azobenzene group is known to be a photo switch, it may be possible be converted to its *cis* isomer by irradiating UV light and reversibly disrupt the vesicle structure.

Appendix B. SAXS and WAXS data processing

B.1. SAXS Data Analysis and Fitting Programs

Analysis of the SAXS data usually includes 2D image integration and form factor fitting. Listed below are some free software online that can serve these purposes:

1) 2D image integration: Fit2D, Nika (126)
2) Form factor fitting: NIST, (127) SASFIT, XPlus (128) and Irena

Fit2D is the software used at DND-CAT 5ID-D for image integration. Nika is a macro that can easily be installed in IgorPro for 2D image processing and integration for both solution SAXS and GISAXS data. We can also use it to integrate the images obtained in the X-ray lab SAXS machine. There is a user guide for Nika available online.

NIST is an excellent macro that can be installed in IgorPro for fitting form factors. This macro has many built-in fitting models such as bilayer, cylindrical or spherical structures that are available to fit different shapes. A very useful manual of NIST can be found in the macro that describes the fitting equations for each model. SAXSFIT also has a good manual for learning different fitting models but the fitting power of this program is not as good as IgorPro.

Besides using the fitting programs that are available online, we can also fit the data with IgorPro. The procedure is as follow

1) Create a graph by clicking “Window/ New graph” and select the appropriate x and y data set
2) Select the graph window. Click “Graph/ Show info” to get the info toolbar that appears below the graph. Then drop the two cursers onto the curve and select the region need to be fitted.
3) Click “Data analysis/ Curve fitting”. There are some very basic functions that can be used.
4) To build our own fitting equations, we can choose “Function and data/ New fit function” and

type in the equations.

5) In the dialog box “Data option”, click “Curser” to allow fitting of the selected region of the curve. The data error can be selected in the section “Weighing data”
6) Type in an initial guess of the fit in “Coefficients”. The coefficients can be saved by creating a new coefficient wave in the same dialog box
7) By clicking “Do it”, IgorPro will fit the data based on the initial guess of the data. One should also fine tune the parameters and try to get the best fit with several trials.

B.2. Fitting Equations

The equations used for fitting SAXS and WAXS data for the crystallized bilayer membranes are shown below as examples. The SAXS data of the bilayer are fitted by the following equation: (129, 130)

$$I = A \cdot 4\pi e^{-\frac{q^2\sigma^2}{2}} \cdot \frac{((\rho_h - \rho_w)\cdot(\sin(q(d_h + d_t)) - \sin(q \cdot d_t)) + (\rho_t - \rho_w)\cdot\sin(q \cdot d_t))^2}{q^4(d_h + d_t)} \quad \text{(A.1)}$$

$$+ \frac{B}{r_t^3} \cdot \left(\begin{array}{l} \dfrac{3 \cdot r_i^3(\rho_{mi} - \rho_{mt})\cdot(\sin(q \cdot r_i) - q \cdot r_i \cdot \cos(q \cdot r_i))}{(q \cdot r_i)^3} \\ + \dfrac{3 \cdot r_h^3(\rho_{mt} - \rho_w)\cdot(\sin(q \cdot r_t) - q \cdot r_t \cdot \cos(q \cdot r_t))}{(q \cdot r_t)^3} \end{array} \right)^2 + background,$$

where ρ_h and ρ_t represent the electron density of the hydrophilic and hydrophobic regions, of the membrane, respectively, ρ_w is the water electron density, σ is the surface roughness of the bilayer, ρ_{mt} and ρ_{mi} represent the electron densities of the hydrophilic and hydrophobic region of the micelle, and r_t and r_i represent the total radius of the micelles and the radius of the hydrophobic region.

The bilayer electron density map is then built with the following equation. An example is

shown in Figure B2.1c

$$\rho_r = \rho_w + \frac{\rho_h - \rho_t}{2}\left(1 + erf\left(\frac{r}{\sqrt{2}\cdot\sigma}\right)\right) + \frac{\rho_t - \rho_h}{2}\left(1 + erf\left(\frac{r - d_h}{\sqrt{2}\cdot\sigma}\right)\right) + \frac{\rho_h - \rho_t}{2}\left(1 + erf\left(\frac{r - d_h - 2d_t}{\sqrt{2}\cdot\sigma}\right)\right) + \frac{\rho_w - \rho_h}{2}\left(1 + erf\left(\frac{r - 2d_h - 2d_t}{\sqrt{2}\cdot\sigma}\right)\right), \quad \text{(A.2)}$$

where ρ_r is the electron density at a distance r normal to the membrane surface and *erf* is the error function

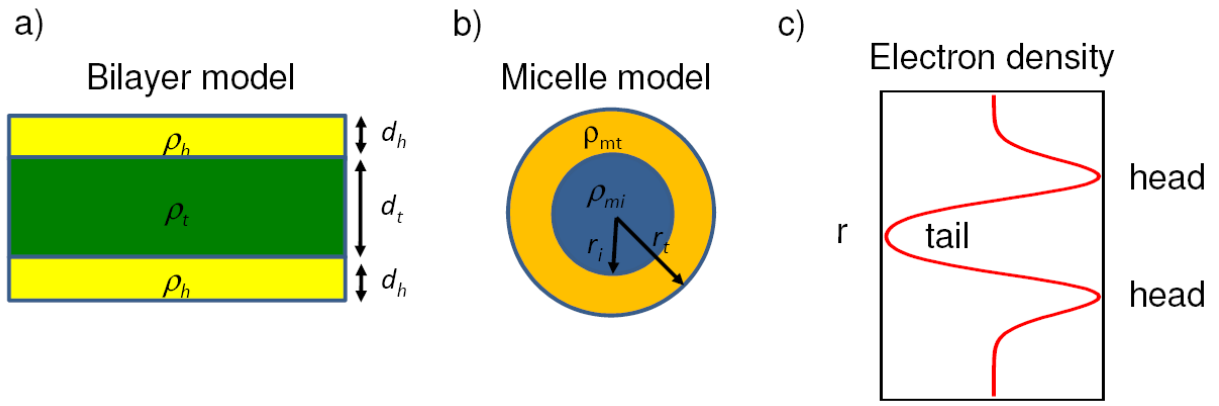

Figure B2.1. (a) Bilayer model and (b) micelle model used to fit the SAXS data of catanionic mixture. (c) Bilayer electron density map of catanionic bilayers

The WAXS diffraction peaks are fitted with Lorentzian functions.

$$I = h\frac{\frac{1}{2}\Gamma}{(q - q_0)^2 + (\frac{1}{2}\Gamma)^2} + background, \quad \text{(A.3)}$$

Where h is the peak height, Γ is the full width at half maximum and q_0 is the peak maximum position.

B.3. SAXS and WAXS Raw Data Averaging

When conducting solution SAXS or WAXS experiments, we often average 5 to 10 images of each sample rather than taking very long exposures. The reasons are as follows: i) to get rid of the random background radiation collected by some CCD pixels, ii) to avoid bubbles in the solution that could ruin the only image, iii) to ensure that the solution is isotropic, and iii) to calculate the error of the scattered data because Fit2D often overestimates the error. Since CCD detectors do not output the exact photon counts, we cannot use the square root of the output signal as our uncertainties. The following MATLAB routine uses the Chauvenet rejection algorithm to calculate the averaged $I(q)$ values from the datasets and also determines the uncertainties $\Delta I(q)$ based on the standard deviation of the original raw data points.

```
% load all data files
clear;
frame = '126';
str1 = strcat('pal_saxs_', frame, '_000');
str3 = '_m2.txt';
scale = 1;
n = 5;
row_size = 633;

total = zeros(row_size,1);
err_tot = zeros(row_size,1);
tempvari = 0;
t = 1.7;
for j =1:n
        ji = int2str(j-1);
        name = strcat(str1, ji, str3);
        fid = fopen(name);
        C = textscan(fid,'%f %f %f %f %f %f %f %f %f %f %f %f %f %f %f %f %f %f %f %f %f %f %f %f',
```

```
'HeaderLines',82);
        fclose(fid);
        q(:,j)= C{1,2};
        intensity(:,j)= C{1,3};
        err(:,j)= C{1,4};
        total = total + intensity (:, j);
                % plot
        set(gca, 'YScale', 'log');
        set(gca, 'XScale', 'log');
        hold on;
        cc=hsv(20);
        loglog(q(:,j), intensity(:,j),'color',cc(j,:));
        xlabel ('q [A^{-1}]');
        ylabel ('Intensity');
  end;
  hold off;
  %start rejection here
  %calculate SD and average here
  % need to do a transpose since the MATLAB fns do ave and std vertically
  intensity_tran = intensity';
  ave_tran = mean(intensity_tran);
  ave = ave_tran';
  SDN_tran = std(intensity_tran);
  SDN = SDN_tran';

  ub = ave + 1.5 * SDN;
  lb = ave - 1.5 * SDN;

  len = length(ave);
  for j =1:len
      count = n;
      for i =1:n
              if (intensity(j,i) > ub(j)) || (intensity(j,i) < lb(j))
              total(j) = total(j) - intensity(j,i);
```

```
            count = count -1;
            end;
    end;
    ave(j) = total(j) / count;
end;
  % here i use SD as the error
err_ave = SDN_tran;

figure(2);
loglog(q(:,1), ave(:));
legend('averaged data','frame 1', 'frame 2');
xlabel ('q [A^{-1}]');
ylabel ('Intensity');

newave(:,1)= q(:,1);
newave(:,2)= ave * scale;
newave(:,3)= err_ave*scale;
outname = strcat('ave_SAXS_', frame, '.txt');

dlmwrite(outname, newave, 'delimiter', ' ', 'precision', 8)
```

B.4 Radial Distribution Function (RDF) Calculation

In chapter 6, the radial distribution of the nanofibers was computed from the x-ray scattering data to determine whether they form a crystallized network with the following equation stated in Chapter 6. (119)

$$g(r) = \frac{1}{2\pi\rho}\int [S(q)-1]J_0(qr)qdq \quad (6.2)$$

,

where $J_0(qr)$ is the Bessel function of the first kind and $S(q)$ is the structural factor

The Matlab code for this calculation is shown below:

```
function temp
    load form.txt;

    q = form (:, 1);
    Sq = form (:, 2);

    Mr = 5000;
    pts = 5000;
    r = linspace(0,Mr,pts);
    g = linspace(0,Mr,pts);
    for j = 1:length(r)
        Y = (Sq(:)-1).*besselj(0,q(:)*r(j)).*q(:);
        g(j) = trapz(q,Y);
    end
    g = g/2/pi/2.55e-6;
    figure(100);
    plot(r,g);
end
```